

**CZECH TECHNICAL  
UNIVERSITY IN PRAGUE**

**FACULTY OF MECHANICAL  
ENGINEERING**



**MASTER'S THESIS**

**CONTROL STRATEGIES FOR  
BLDC MOTORS**

**2019**

**SHAWN MOSES  
CARDOZO**



# MASTER'S THESIS ASSIGNMENT

## I. Personal and study details

Student's name: **Cardozo Shawn Moses** Personal ID number: **472474**  
Faculty / Institute: **Faculty of Mechanical Engineering**  
Department / Institute: **Department of Instrumentation and Control Engineering**  
Study program: **Mechanical Engineering**  
Branch of study: **Instrumentation and Control Engineering**

## II. Master's thesis details

Master's thesis title in English:

**Control strategies for Brushless DC motors**

Master's thesis title in Czech:

**Strategie řízení bezkartáčových DC motorů**

Guidelines:

- 1) Carry out a research on a topic 'control strategies for BLDC motors'. Describe the BLDC motor function, explain the basic principles of BLDC motor control using power electronics and investigate possibilities of its sensorless control.
- 2) Model the BLDC motor control in Matlab Simulink. From the previous point, choose a suitable feedback control strategy for a BLDC motor and create a model of the situation, including a simplified power electronics model.
- 3) Program and test the actual motor control. Choose the appropriate feedback control strategy for a BLDC motor and program the strategy using a suitable control electronics. Permanent magnet synchronous motor (PMSM) can be used instead if the BLDC motor is not available.
- 4) Evaluate the quality of the control algorithm and suggest possible improvements and future developments.

Bibliography / sources:

- [1] KRISHNAN, R. Permanent magnet synchronous and brushless DC motor drives. Boca Raton, 2010. ISBN 978-0-8247-5384-9.
- [2] BUSO, Simone a Paolo MATTAVELLI. Digital Control in Power Electronics. Morgan & Claypool, 2006. ISBN 9781598291131.
- [3] KAŻMIERKOWSKI, Marian P., R. KRISHNAN a Frede BLAABJERG. Control in power electronics: selected problems. New York: Academic Press, 2002. ISBN 01-240-2772-5.

Name and workplace of master's thesis supervisor:

**Ing. Zdeněk Novák, U12110.1**

Name and workplace of second master's thesis supervisor or consultant:


Date of master's thesis assignment: **26.04.2019**

Deadline for master's thesis submission: **12.06.2019**

Assignment valid until: \_\_\_\_\_

  
Ing. Zdeněk Novák  
Supervisor's signature

  
Head of department's signature

  
prof. Ing. Michael Valášek, DrSc.  
Dean's signature

## III. Assignment receipt

The student acknowledges that the master's thesis is an individual work. The student must produce his thesis without the assistance of others, with the exception of provided consultations. Within the master's thesis, the author must state the names of consultants and include a list of references.

23-4-2019  
Date of assignment receipt

  
Student's signature

# Abstract

Shawn Moses Cardozo: Control Strategies for Brushless DC motors

Master's Thesis (Supervisor: Ing. Zdeněk Novák)

Department of Instrumentation and Control Engineering, Faculty of Mechanical Engineering – Czech Technical University in Prague, Prague 2019. 94 pages

Master's Thesis researching the various control strategies available for BLDC motor control that can then be employed in the speed control of electric vehicle drive systems. The task involved studying the various control algorithms, finding ways to optimize their performance and simulate them as a proof of concept. The final stage of the thesis involved the preparation of an implementable control algorithm that was then run on a test bench with an active PID feedback-based control system and HMI for easy interaction in runtime.

Keywords: Brushless DC Motor, Space vector modulation, Feedback Control, LabView FPGA, Third Harmonic, Start-Up control

# Abstrakt

Shawn Moses Cardozo: Strategie řízení bezkartáčových DC motorů

Diplomová práce (Vedoucí práce: Ing. Zdeněk Novák)

Ústav přístrojové a řídicí techniky, Fakulta strojní – ČVUT v Praze, Praha 2019. 94 stran


Tato diplomová práce se zabývá strategiemi řízení, které jsou dostupné pro bezkartáčové DC motory, a které mohou být použity pro řízení rychlosti pohonů elektrických vozidel. Úkolem práce je studium rozličných řídicích algoritmů, nalezení způsobů, jak optimalizovat jejich výkon, a zároveň simulovat jejich chování pro ověření jejich vlastností. Závěrečná etapa práce spočívá v přípravě implementovatelného řídicího algoritmu, který je poté spuštěn na laboratorním stanovišti s aktivním řídicím systémem založeným na zpětné vazbě PID regulátoru a uživatelského rozhraní (HMI) pro snadnou interakci v průběhu testu.

Klíčová slova: Střídavý DC motor, Prostorová vektorová modulace, LabView FPGA, Řízení zpětné vazby, Třetí harmonický, Ovládání spouštění

## Statement

I declare that this thesis and the work presented in it has been composed solely by me and that it has not been submitted, in whole or in part, in any previous application for a degree. I agree that its results can be further used at the discretion of the thesis supervisor as its co-author. Except where stated otherwise by reference or acknowledgment, the work presented is entirely my own. I also agree with the potential publication of the results of the thesis or of its substantial part, provided I will be listed as the co-author.

Prague, 10<sup>th</sup> June, 2019.

  
.....  
Cardozo Shawn Moses

# Acknowledgements

I would like to thank my supervisor for his help and guidance in developing this research. I am also grateful to the Mechanical Faculty at ČVUT, Prague for lending me the components and access to a laboratory for developing my test bench for this research.

I would like to thank my colleagues at Ricardo s.r.o. for advising me throughout this research and Ricardo plc. for providing me with this opportunity to participate in this research program.

I would also like to thank my parents for their ever enduring support and my friends that that have stood by my side.

Thank You.

# Table of Contents

<b>1. Introduction.....</b>	<b>6</b>
1.1. Overview of Chapters.....	7
<b>2. State of the art .....</b>	<b>8</b>
2.1. Basic functionality of BLDC Motor .....	8
2.2. BLDC Motor model.....	10
2.2.1. State Equations .....	12
2.2.2. Hall Effect Sensors.....	14
2.2.3. Mechanical model.....	14
2.3. Principle of the Hall Effect sensor control.....	16
2.4. Principle of Sensor-less control.....	18
2.5. Start-up control.....	20
2.5.1. Prepositioning Phase.....	20
2.5.2. Starting Ramp.....	21
2.5.3. Switching To Auto-Commutated Mode .....	22
2.6. Space Vector Pulse Width Modulation .....	24
2.6.1. Vector Notation for SV-PWM.....	24
2.6.2. Synthesizing the required output voltage.....	27
2.7. Third Harmonic Injection.....	31
2.7.1. Purpose.....	31
2.7.2. Strategy for optimization .....	32
2.7.3. Modulation index.....	33
2.7.4. Over-Modulation and its purpose.....	33
<b>3. Proposed Control Strategies.....</b>	<b>34</b>
3.1. Using reference active and reactive current.....	34
3.1.1. Control Process .....	34
3.1.2. Advantage .....	35
3.2. Using reference speed (Direct voltage modulation).....	36
3.2.1. Advantage .....	36
3.2.2. Disadvantage .....	36

<b>4. Simulation of control strategies.....</b>	<b>37</b>
4.1. Simulink model for control with Hall Effect sensor.....	37
4.1.1. Result.....	41
4.2. Simulink model for Sensor-less control.....	42
4.3. Simulink model for Startup control.....	46
4.3.1. Transition from Startup control to the standard control.....	46
4.3.2. Transition between stages of the start-up control.....	47
4.4. Simulink model for Sine wave PWM with third harmonic injection control.....	50
4.5. Simulink model for Space vector modulation with PWM control.....	53
4.6. Future Prospects.....	56
4.6.1. Optimization of Power supply.....	56
<b>5. Practical Realization .....</b>	<b>60</b>
5.1. Hardware Setup .....	61
5.1.1. PMSM Motor.....	62
5.1.2. DC Power Source.....	62
5.1.3. Six step Inverter.....	63
5.1.4. MyRIO Student Embedded Device.....	65
5.1.5. Angular position Resolver .....	66
5.2. Labview algorithm.....	67
5.2.1. LabView FPGA VI Component .....	67
5.2.2. Labview VI .....	72
5.2.3. Results from Practical implementation.....	73
<b>6. Conclusion.....</b>	<b>75</b>
6.1. Proposed research for Future .....	76
<b>7. Appendix A - Hardware specifications.....</b>	<b>77</b>
<b>8. Appendix B – LabView Block Diagram.....</b>	<b>83</b>
<b>References .....</b>	<b>84</b>

## Table of Figures

Figure 2.1 – Cross-Sectional representation of a BLDC Motor <sup>[3]</sup> .....	8
Figure 2.2 - BLDC Motor Functional Diagram with 6 – Step Inverter <sup>[1]</sup> .....	9
Figure 2.3 – Internal magnetic force <sup>[3]</sup> .....	9
Figure 2.4 - Permanent magnet synchronous machine .....	10
Figure 2.5 - PMSM Parameter setup .....	10
Figure 2.6 - Phase BEMF <sup>[4]</sup> .....	10
Figure 2.7 - Simulink PMSM motor model <sup>[4]</sup> .....	11
Figure 2.8 - Simulink model for Electrical Aspects <sup>[4]</sup> .....	12
Figure 2.9 - Simplified Electrical Circuit.....	12
Figure 2.10 - State Model <sup>[4]</sup> .....	13
Figure 2.11 - Phase Current Calculator <sup>[4]</sup> .....	13
Figure 2.12 - Hall Effect Signal Generator <sup>[4]</sup> .....	14
Figure 2.13 - Simulink model for Mechanical Aspects <sup>[4]</sup> .....	15
Figure 2.14 - Hall sensor <sup>[1]</sup> .....	16
Figure 2.15 - Six-step control and PWM wave <sup>[1]</sup> .....	17
Figure 2.16 - Hall-effect sensor waveforms with back-EMF trapezoidal waveforms <sup>[11]</sup> .....	18
Figure 2.17 – Zero-crossing detection <sup>[11]</sup> .....	19
Figure 2.18 - Prepositioning rotor alignment <sup>[11]</sup> .....	20
Figure 2.19 - Prepositioning current ramp <sup>[11]</sup> .....	20
Figure 2.20 – Starting ramp <sup>[11]</sup> .....	21
Figure 2.21 - Stator BEMF during starting ramp <sup>[11]</sup> .....	22
Figure 2.22 – Switching to Auto-commutated mode <sup>[11]</sup> .....	23
Figure 2.23 - Two Level Inverter Schematic.....	24
Figure 2.24 - Vector Representation .....	25
Figure 2.25 - Gate configurations for Vector Combinations .....	26
Figure 2.26 – Input Reference and Trigonometric Wave.....	27
Figure 2.27 - Switching State Vectors .....	28
Figure 2.28 – Switching State Pattern .....	28
Figure 2.29 - Relative time on for switching state .....	29
Figure 2.30 - Space Vector Hexagon.....	31
Figure 2.31 - Control without Third harmonic injection.....	32
Figure 2.32 - Control without Third harmonic injection.....	32
Figure 2.33 - Superposition of three phases .....	32
Figure 3.1 - Using reference active and reactive current .....	34
Figure 3.2 - Transformation process .....	35
Figure 4.1 - Encoder.....	37
Figure 4.2 - De-coder.....	38
Figure 4.3 - Brushless DC Motor fed by Six Step inverter and Hall Effect sensor base control .....	39



Figure 4.4 - Output Rotor Angle .....	40
Figure 4.5 - Hall Effect Signal .....	40
Figure 4.6 - Output Rotor Speed.....	41
Figure 4.7 - Back EMF cross over pulse detection Signal .....	42
Figure 4.8 - Edge Detection .....	42
Figure 4.9 - Top edge detection.....	43
Figure 4.10 - Pulse generator .....	43
Figure 4.11 - Rising edge detector.....	43
Figure 4.12 - Edge signals .....	43
Figure 4.13 - Back EMF gate signal generator.....	44
Figure 4.14 - Brushless DC Motor fed by 6 - step inverter and Senso-rless control algorithm.....	45
Figure 4.15 - Gate Signals.....	46
Figure 4.16 - Transition from Startup control to the standard control.....	46
Figure 4.17 - Phase transition.....	47
Figure 4.18 - Phase 1 gate signal generator .....	47
Figure 4.19 – Phase transition.....	48
Figure 4.20 – Phase 2 Signal Generator .....	48
Figure 4.21 - Brushless DC Motor fed by 6 - step inverter and Start-up control algorithm .....	49
Figure 4.22 – Third harmoninc Modulation in phases.....	50
Figure 4.23 - Sine wave PWM with third harmonic injection control.....	51
Figure 4.24 - Sine wave PWM with third harmonic injection .....	51
Figure 4.25 - BLDC Motor with SW-PWM and Third harmonic control.....	52
Figure 4.26 -Triangle wave generator    Figure 4.27 - Sector Generator .....	53
Figure 4.28 - Time ratio generator.....	53
Figure 4.29 - PID controller.....	53
Figure 4.30 - Vector Generator .....	54
Figure 4.31 - Final Stage .....	54
Figure 4.32 - Gate signal Generator .....	54
Figure 4.33 - BLDC Motor with SV-PWM controller .....	55
Figure 4.34 – Schematic of power management system.....	57
Figure 4.35 - Final model of proposed power management system .....	57
Figure 4.36 - Difference in current load at start-up.....	58
Figure 4.37 - Difference in current load at 6- step control.....	58
Figure 5.1 –Test bench.....	61
Figure 5.2 – Block Diagram of components.....	61
Figure 5.3 – DC source and PMSM Motor.....	62
Figure 5.4 – Six-pack Driver .....	63
Figure 5.5 – IGBT Module .....	63
Figure 5.6 – AC/DC transformers .....	64
Figure 5.7 – Current Sensors .....	64
Figure 5.8 – Cooling Fin for Heat dissipation .....	64

Figure 5.9 - MyRio Student Embedded Device .....	65
Figure 5.10 - Block Diagram.....	65
Figure 5.11 – A, B, Z Signal lines.....	66
Figure 5.12 – Resolver Schematic <sup>[26]</sup> .....	66
Figure 5.13 - FPGA VI front Panel.....	67
Figure 5.14 - PID Controller loop.....	68
Figure 5.15 - Angle and time generator loop.....	69
Figure 5.16 - Sector and vector generator loop .....	70
Figure 5.17 - Phase signal generator loops.....	71
Figure 5.18 - FIFO Generator loop.....	71
Figure 5.19 - LabView VI Front panel .....	72
Figure 5.20 – Real measured value from oscilloscope.....	73
Figure 5.21 – Real vs. Simulated result.....	73
Figure 7.1 - 2AML406B-S PMSM Motor <sup>[35]</sup> .....	77
Figure 7.2 - Technical data for 2AML406B <sup>[38]</sup> .....	78
Figure 7.3 - Manson NP-9625.....	78
Figure 7.4 - Semikron SKHI 61 <sup>[41]</sup> .....	79
Figure 7.5 - Chip Back-view <sup>[41]</sup> .....	79
Figure 7.6 - Schematic of SKHI 61 <sup>[41]</sup> .....	79
Figure 7.7- Characteristics of SKHI 61 .....	80
Figure 7.8 - SKM 75 GD 124 D <sup>[3]</sup> .....	81
Figure 7.9 - Schematic of SKM <sup>[3]</sup> .....	81
Figure 7.10 - Characteristics of SKM 75 <sup>[3]</sup> .....	81
Figure 7.11 - BV EI 481 1184 transformer <sup>[45]</sup> .....	82
Figure 7.12 - LEM LA-55-P Current sensor <sup>[46]</sup> .....	82
Figure 8.1 –Block diagram for LabView Section.....	83
Figure 8.2 – Block Diagram for FPGA Section.....	83

# List of Tables

Table 1 – List of variables .....11  
*Table 2 - Commutation Table* .....17  
Table 3 – Look-up table data.....70  
*Table 4 - Pin description* .....80

## List of Abbreviations

BLDC	Brushless Direct Current motor
PID	Proportional-Integral-Derivative
HMI	Human Machine Interface
PMSM	Permanent Magnet Synchronous Motor
AC/DC	Alternating Current / Direct Current
BEMF	Back Electromotive Force
SV-PWM	Space Vector- Pulse Width Modulation
IGBT	Insulated-Gate Bipolar Transistor
FPGA	Field Programmable Gate Array
VI	Virtual Instrument
FIFO	First In First Out
MCU	Motor Control Unit
DSC	Digital Speed Controller
SPDT	Single Pole Double Throw
RMS	Root Mean Square
MOSFET	Metal Oxide Semiconductor Field Effect Transistor
SR	Set Reset
LED	Light Emitting Diode
IC	Integrated Circuit
PROM	Programmable Read Only Memory
LCD	Liquid Crystal Display
CMOS	Complementary Metal–Oxide–Semiconductor

# 1. Introduction

The central objective of this research is to understand, simulate and optimize the control strategies for the control of BLDC motors and compare their results. The end goal of this project undertaken by Ricardo plc. is to develop a complete motor and control system for installation in electric vehicles for their partner firms.

The focus in terms of control strategies shall include the below control algorithms and respective control circuits -

- Hall Effect sensor control
- Sensor-less control
- SVM based control

The brushless DC motor (BLDC) is also referred to as an electronically commutated motor. BLDC Motors have no brushes on the rotor and the commutation is performed electronically at certain rotor positions by a Controller/Driver circuitry.

The replacement of a DC motor by a BLDC motor places a higher requirement for a control algorithm and a control circuit.

1. The general BLDC motors are normally in three-phase system configurations. They must therefore be supplied with a three-phase power supply.
2. The rotor position must be known exactly to align the applied voltage. <sup>[1]</sup>

For the purpose of developing an understanding of BLDC motor performance and also generating computer algorithms for predicting calibratable parameters, the proposed simulations form a core of the research.

The simulation of the various control algorithms to be used in with BLDC motor models have been implemented using the MATLAB tool Simulink in conjunction with the features offered by SimScape. This allows for a further clarity in verifying the differences in the control strategies. In addition to this, the models generated shall also give a reference platform for generating a Calibration system and control program Library for further future usage.

As shall be further shown in the research, the various control strategies shall be studied, and the overall output efficiencies shall be mapped.

Another major focus of this work shall include the generation of a control system across an inverter power supply pack for reducing load fluctuations generated across the supply.

The final stage for this research will also include a complete workbench with a testable control algorithm to verify if the predicted model results match those obtained in the real world system.

# 1.1. Overview of Chapters

- **Chapter 2 – State of the art**

This chapter includes a study of the functionality and modeling of BLDC motors and the principles of their control algorithms. The main control strategies addressed include -

- Hall Effect sensor control
- Sensor-less control
- SVM based control
- Start-up control

- **Chapter 3 – Proposed control strategy**

This chapter deals with a proposal for improving the feedback control of the motor by reducing of the computational requirements on the controller. This is especially beneficial when the motor runs at high speeds.

- **Chapter 4 – Simulation of control strategies**

In this chapter, the previously discussed control algorithms are simulated in MATLAB Simulink to provide predictions of their behavior. The simulations have then been analyzed respectively and their results assessed.

- **Chapter 5 – Practical realization**

The practical realization of a BLDC motor on a constructed test bench and all the related Hardware and Software components have been discussed in this chapter. The results have also been elaborated and compared to the simulated predictions.

- **Chapter 6 - Conclusion**

In this chapter, all the work performed in this thesis has been compiled and analyzed to provide a holistic understanding of the work and the way forward to progress in the research of a BLDC control system for the electric vehicle market.

## 2. State of the art

### 2.1. Basic functionality of BLDC Motor

Brushless DC motors or synchronous DC motors are synchronous motors that are powered by DC power through an inverter or a switched mode power supply that generates an AC drive for each phase of the motor via a closed controller. The controller supplies current pulses to the motor windings which control the speed and torque of the motor.<sup>[2]</sup>

The design of a brushless motor system is a permanent magnet synchronous motor with trapezoidal BEMF (PMSM).

The advantages of a brushless motor over brush motors include

- high power-to-weight ratio
- high speed
- Processor based control

Brushless motors find applications in areas such as computer peripherals (disk drives, printers), hand-held power tools and vehicles ranging from model aircraft to automobiles.<sup>[3]</sup>

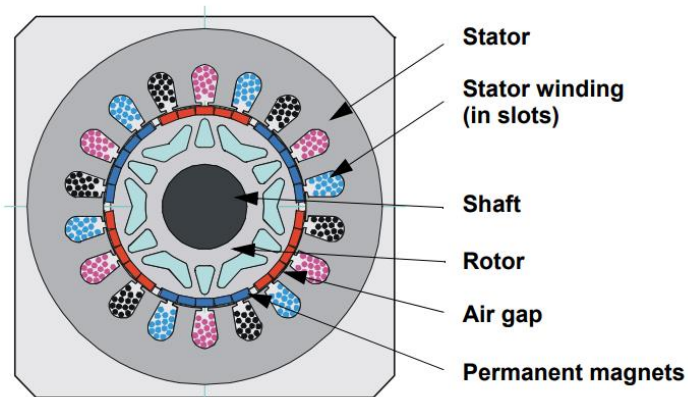


*Figure 2.1 – Cross-Sectional representation of a BLDC Motor<sup>[4]</sup>*

Figure 2.1 and Figure 2.2 show the internal structure and functional diagram of a three-phase BLDC motor. The rotor (generally external, some rotors are internal) has two pole pairs and consists of permanent magnets. The stator consists of three-phase windings (A, B and C).

In most cases, the stator magnetic circuit is constructed using magnetic steel sheets. Stator phase windings are inserted in the grooves (distributed winding) or wound as a single coil around the magnetic pole. The arrangement of the permanent magnet's magnetization and their respective displacement on the rotor are chosen in such a way that the back-EMF shape is trapezoidal. Back-EMF here refers to the induced voltage in

the stator winding due to the relative movement of the rotor. This allows a rectangular-shaped 3-phase voltage system to create a rotational field with low torque ripples. [4]

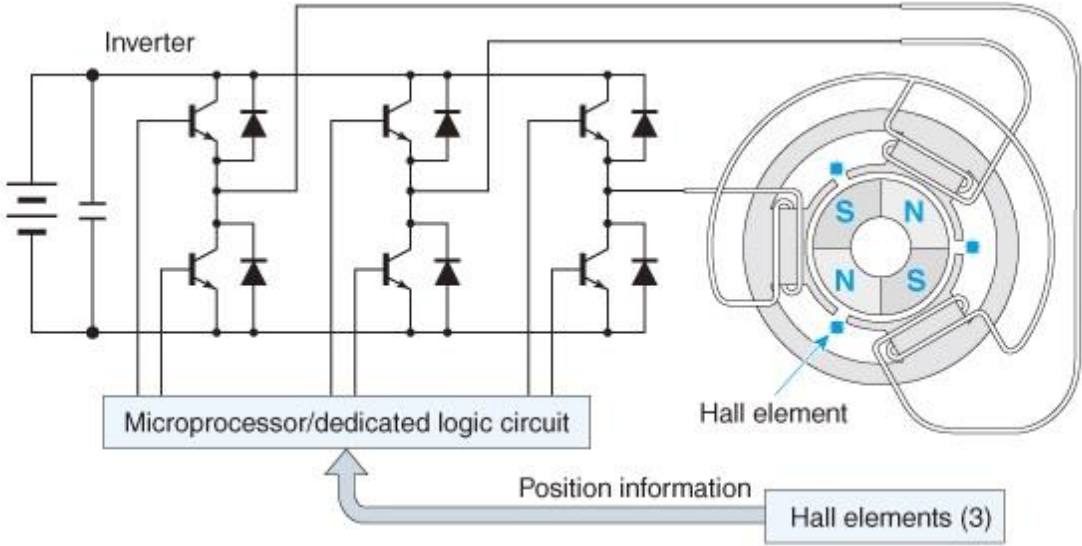


Figure 2.2 - BLDC Motor Functional Diagram with 6 – Step Inverter<sup>[1]</sup>

Upon being powered, the stator windings begin to generate a magnetic field, which attracts or repels the permanent magnet (rotor), as a result of this action a rotor spin is brought about. See the Figure 2.3.

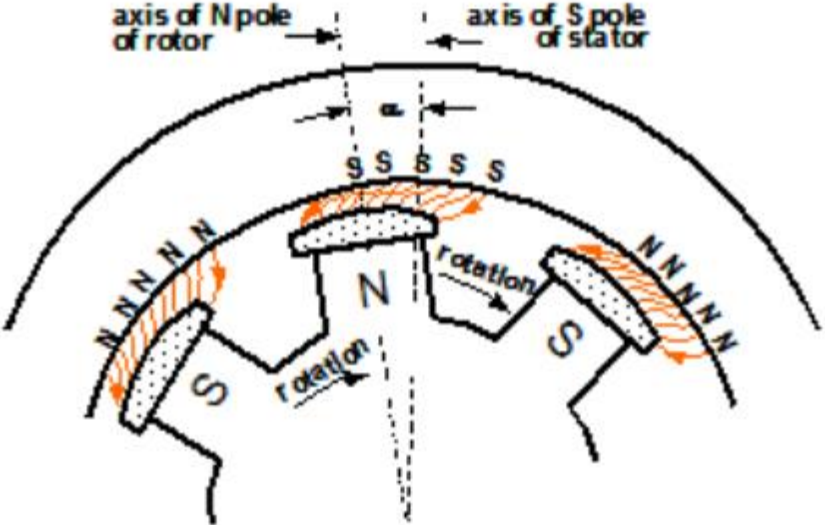


Figure 2.3 – Internal magnetic force<sup>[4]</sup>

The BLDC motor shares its working principle with the DC motor. In the situation that the MCU and control circuit in a BLDC motor fail to change the direction of the generated magnetic field, the stator windings lose synchronization with the rotor. Thus the rotor will not rotate. This makes it essential to develop an arrangement to adjust the position of the electronic commutation and change the direction in order that the BLDC motor may generate the appropriate rotating magnetic field around the rotor. [1]



## 2.2. BLDC Motor model

The model used for the BLDC Motor in this research can be seen as the direct application of the PMSM Motor model (see *Figure 2.4*) available in Simulink/SimScape.

The purpose for using the Permanent Magnet Synchronous Motor (PMSM) model in the case of this research is because this is the default application offered by MATLAB for

modelling BLDC motors.

In absence of an existing pre-selected motor, it was thought best to use an existing tried and tested model to prove the principle of the control algorithms.

Both the BLDC motor and the PMSM are similar in construction i.e. they have permanent magnets in the rotor that interact with the magnetic field produced by the stator coils. The difference lies in the fact that in a PMSM the Back Electro Magnetic Force (BEMF) is generated in a sinusoidal manner while in a BLDC Motor the BMEF is generated in a trapezoidal manner.(see *Figure 2.6*)

Simulink/SimScape offers this configurability in the settings window (see *Figure 2.5*) and hence the final motor model offered is a complete BLDC Motor and can be fairly employed for this research.

The following section will try and describe the mathematical functionality of the components of the BLDC Motor being modeled under the above mentioned Simulink/SimScape mask.<sup>[5]</sup>

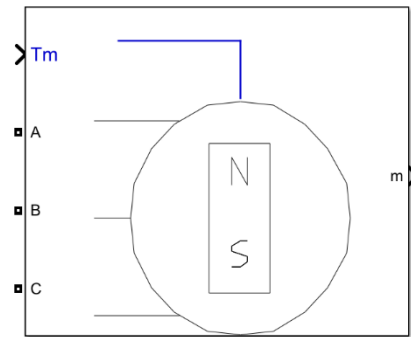


*Figure 2.4 - Permanent magnet synchronous machine*

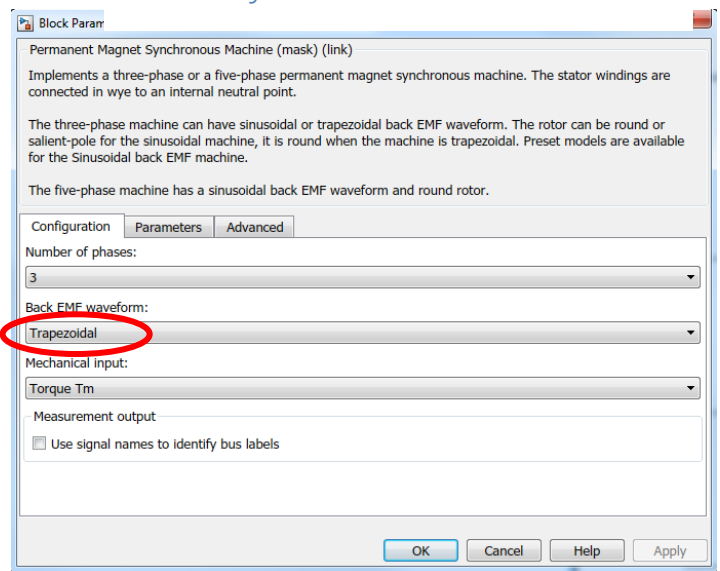


*Figure 2.5 - PMSM Parameter setup*

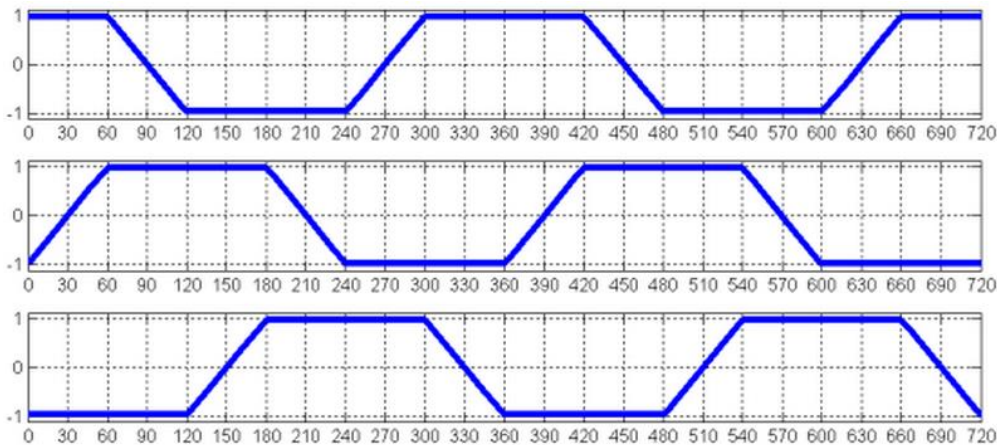
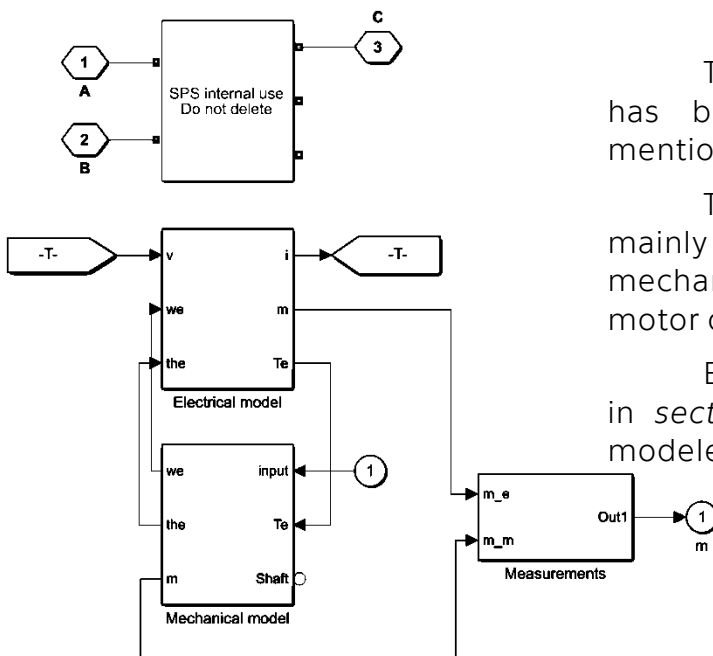


*Figure 2.6 - Phase BEMF<sup>[5]</sup>*

Lets consider the below notation for description of the mathematical model –

Table 1 – List of variables

<b>For model capturing Electrical aspects</b>	
$L$	Inductance of the stator windings
$R_S$	Resistance of the stator windings
$i_a, i_b, i_c$	a, b and c phase currents
$e_a, e_b, e_c$	Induced voltage
$\phi_a, \phi_b, \phi_c$	a, b and c phase electromotive forces, in per-unit value to the amplitude of the flux $\lambda$ .
$V_{ab}, V_{bc}$	ab and bc phase to phase voltages
$\omega_m$	Angular velocity of the rotor
$\gamma$	Amplitude of the flux induced by the permanent magnets of the rotor in the stator phases
$p$	Number of pole pairs
$T_{elec}$	Electromagnetic torque
<b>For model capturing Mechanical aspects</b>	
$J$	Combined inertia of rotor and load
$F$	Combined viscous friction of rotor and load
$\theta$	Rotor angular position
$T_{mech}$	Shaft mechanical torque
$T_{frict}$	Shaft static friction torque



The mathematical model for this work has been understood using references mentioned in the Simulink help. [6, 7, 8, 9, 10, 11]

The Model for the BLDC motor is mainly divided into the electrical and the mechanical model to define the aspects of motor dynamics as seen in Figure 2.7.

Each model is described by equations in section 2.2.1 2.2.1 that are then further modeled in the Simulink blocks.

Figure 2.7 - Simulink PMSM motor model<sup>[5]</sup>

The electric model in *Figure 2.8* is further divided into the parts which model the motor's functionality i.e. the motor's interaction between the rotor and stator during rotor rotation and the feedback generated by the various variables like the Hall effect sensor and BEMF values.

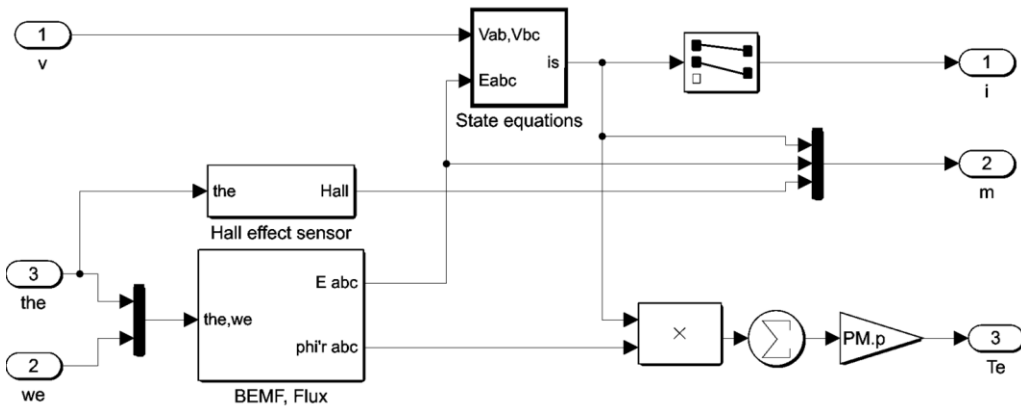


*Figure 2.8 - Simulink model for Electrical Aspects<sup>[5]</sup>*

### 2.2.1. State Equations

Consider the basic circuit scheme for the BLDC motor as seen in the *Figure 2.9*. The equations for the individual voltages can be stated as <sup>[12]</sup>

$$u_a = Ri_a + L \frac{di_a}{dt} + e_a \quad \text{---- (1)}$$

$$u_b = Ri_b + L \frac{di_b}{dt} + e_b \quad \text{---- (2)}$$

$$u_c = Ri_c + L \frac{di_c}{dt} + e_c \quad \text{---- (3)}$$

Thus, the line to line voltages can be found as

$$u_{ab} = R(i_a - i_b) + L \frac{d(i_a - i_b)}{dt} + e_a - e_b \quad \text{---- (4)}$$

$$u_{bc} = R(i_b - i_c) + L \frac{d(i_b - i_c)}{dt} + e_b - e_c \quad \text{---- (5)}$$

$$u_{ca} = R(i_c - i_a) + L \frac{d(i_c - i_a)}{dt} + e_c - e_a \quad \text{---- (6)}$$

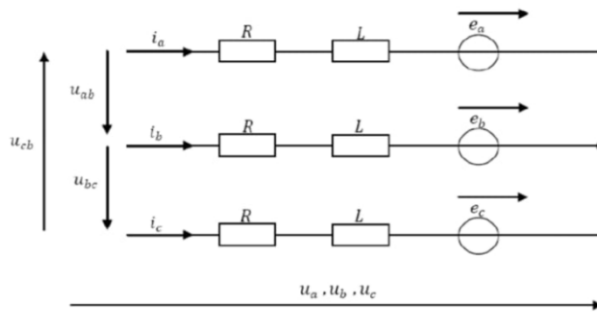


*Figure 2.9 - Simplified Electrical Circuit*

The below equations then implement the dynamics encountered in a 3-phase BLDC motor with trapezoidal Back EMF. The motor may function in both Generator and motor mode depending on the torque value (positive or negative).

The trapezoidal model assumes that three trapezoidal back EMF waveforms shall be produced due to the winding distribution and subsequent flux established by the permanent magnets.

$$\frac{d}{dt} i_a = \frac{1}{3L} (2v_{ab} + v_{bc} - 3R_S i_a + \gamma p \omega_m (-2\phi_a + \phi_b + \phi_c)) \quad \text{---- (7)}$$

$$\frac{d}{dt} i_b = \frac{1}{3L} (-v_{ab} + v_{bc} - 3R_S i_b + \gamma p \omega_m (\phi_a - 2\phi_b + \phi_c)) \quad \text{---- (8)}$$

$$\frac{d}{dt} i_c = - \left( \frac{d}{dt} i_a + \frac{d}{dt} i_b \right) \quad \text{---- (9)}$$

$$T_{elec} = p \gamma (\phi_a i_a + \phi_b i_b + \phi_c i_c) \quad \text{---- (10)}$$

The below *Figure 2.10* of the model shows the two blocks that capture equation 7, equation 8 and equation 9. These are then modeled in the below *Figure 2.11*.

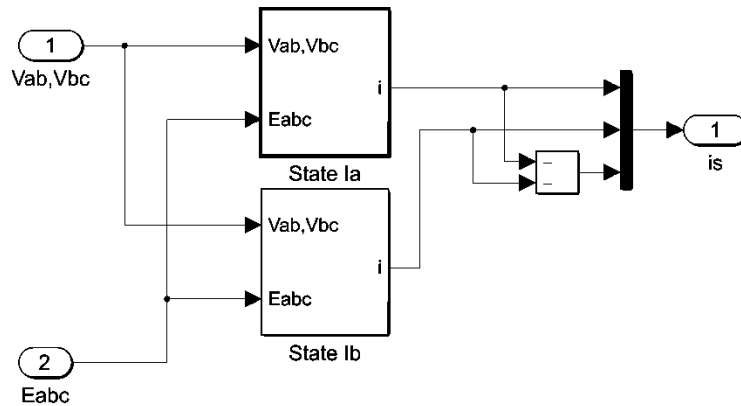


Figure 2.10 - State Model<sup>[5]</sup>

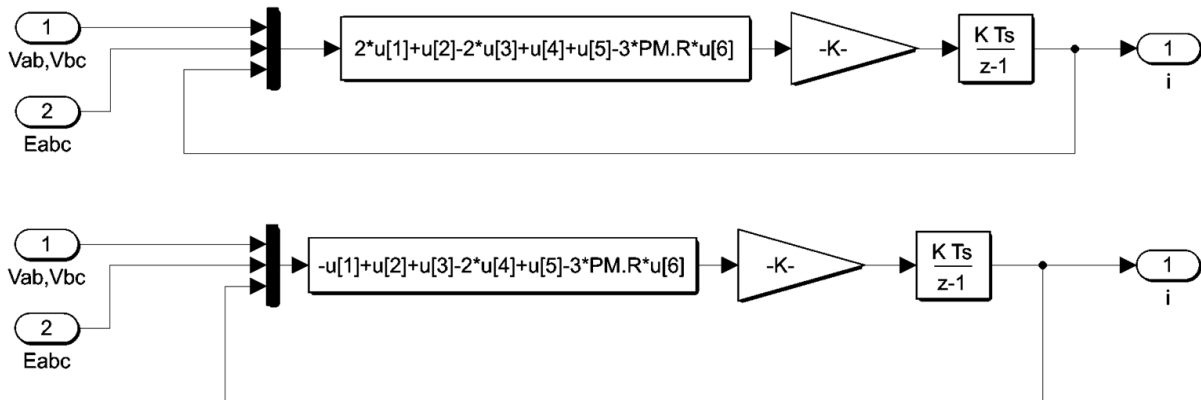


Figure 2.11 - Phase Current Calculator<sup>[5]</sup>

## 2.2.2. Hall Effect Sensors

The below subsystem in *Figure 2.12* is for calculation of the rotor angle in order to be used further in the generation of sensor signals of Hall Effect. The Hall Effect sensor values are generated by mapping the previously calculated rotor angle to the sector it lies in and then producing the respective signal for the phase.

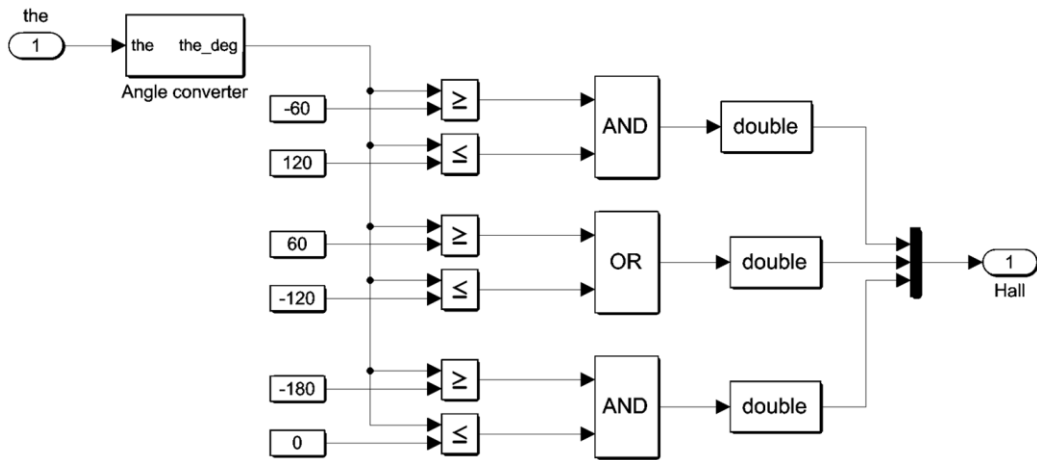
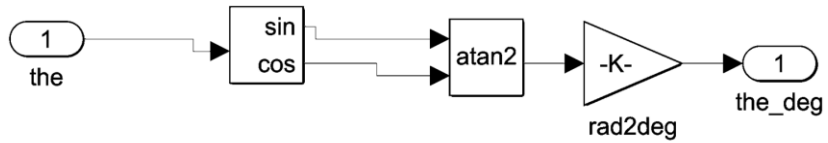


Figure 2.12 - Hall Effect Signal Generator<sup>[5]</sup>

## 2.2.3. Mechanical model

The Mechanical dynamics of the motor are then modeled by application of the below equations in *Figure 2.13*.

$$\frac{d}{dt} \omega_m = \frac{1}{J} (T_{elec} - T_{frict} - F\omega_m - T_{mech}) \quad \text{---- (11)}$$

$$\frac{d}{dt} \theta = \omega_m \quad \text{---- (12)}$$

This completes the entire description of the BLDC Motor model and the aspects of its variable feedback that shall be used in the upcoming chapters for the generation of motor control algorithms.

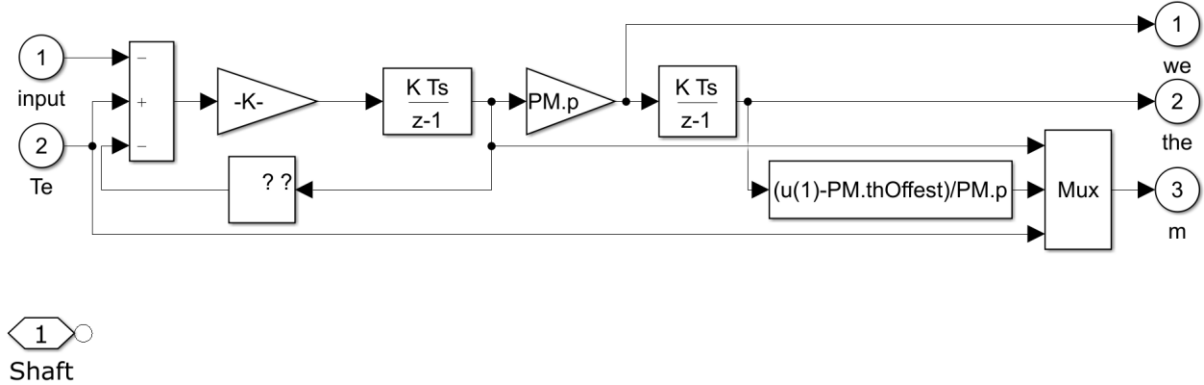
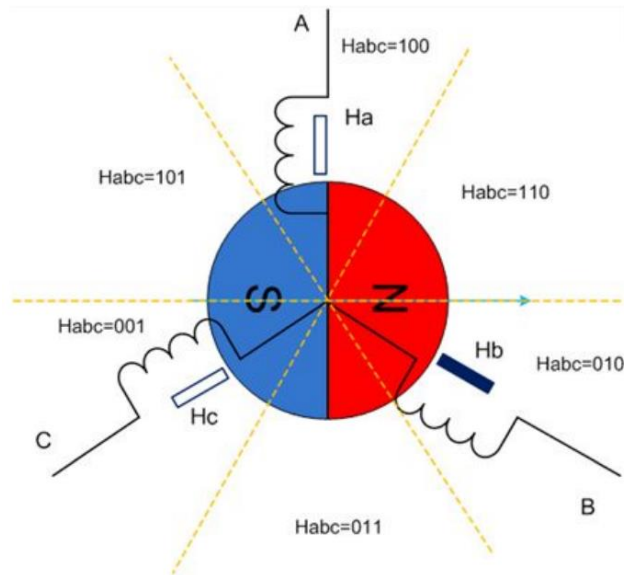


Figure 2.13 - Simulink model for Mechanical Aspects<sup>[5]</sup>

## 2.3. Principle of the Hall Effect sensor control

The Hall Effect sensors are detection switches that output a logic level based on the detection of magnetic fields. A set of 3 Hall Effect sensors ( $H_a$ ,  $H_b$  and  $H_c$ ) are inserted into the stator of the BLDC motor.

For example, in the below *Figure 2.14*, if the  $H_a$  sensor is below the N pole of the permanent magnet, it will output signal 1, otherwise 0. <sup>[1]</sup>



*Figure 2.14 - Hall sensor<sup>[1]</sup>*

Theoretically, given 3 outputs from the 3 Hall Effect sensors, 8 combinations can be derived i.e from 000 to 111. In most cases, due to the hardware's limitation, the signals 000 and 111 do not exist. So, the other 6 states can share one electric cycle of position in six areas, and the exact point at which the status changes from one to another is the position where the commutator changes the direction of the magnetic field of the stator.

Here is the summary of the commutation process as can be seen in *Figure 2.15*

- The excitation of the stator windings will be transitioned six times over the course of the rotor completing one complete rotation of 360 electrical degrees. Each transition is called a commutation.
- The angle between S-N pole (rotor) and magnet field (stator windings) is 60-120°, commutation happens at 60°.
- The commutation position aligns with the status of the Hall sensor changes.
- At any given moment, only two phases are driven by current, while the third one is powered off. <sup>[1]</sup>

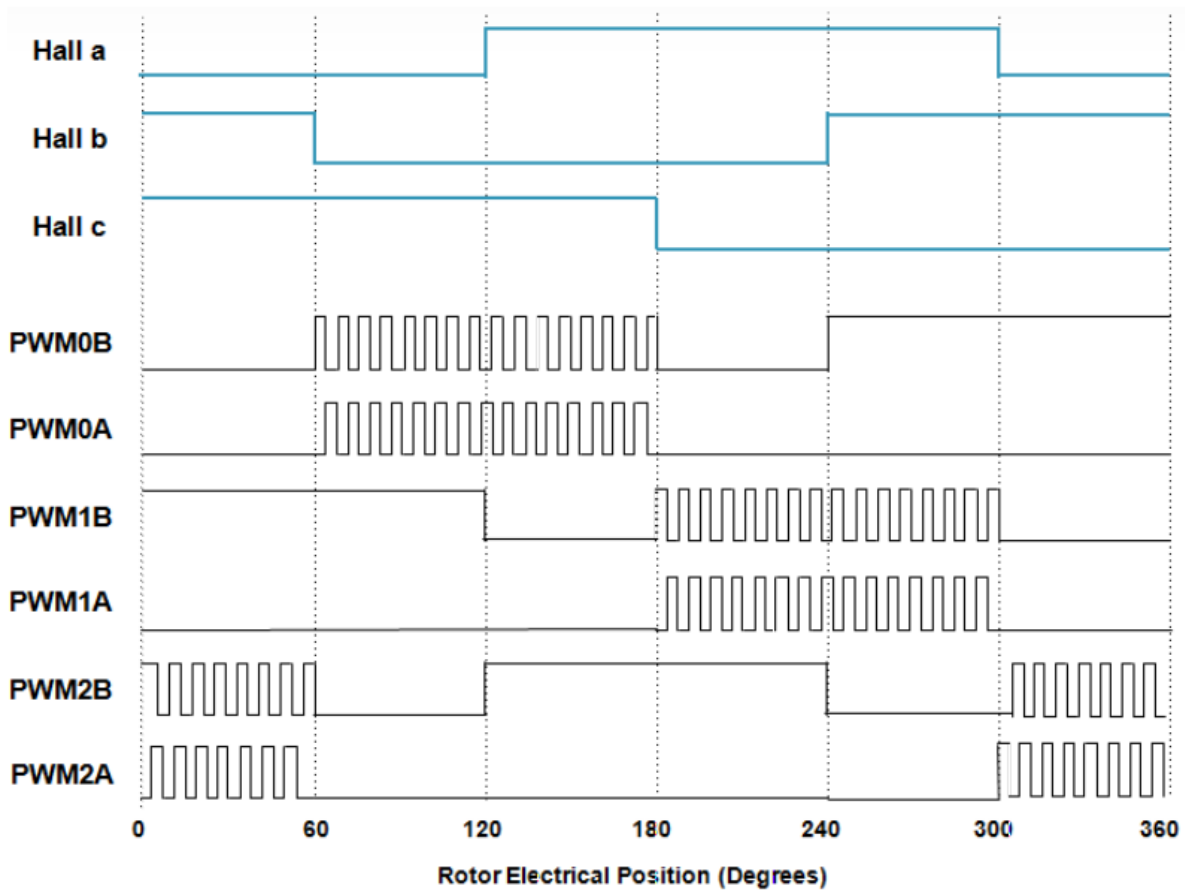


Figure 2.15 - Six-step control and PWM wave<sup>[1]</sup>

As discussed previously in the Six-step commutation, the six commutation positions are fixed in 360 electrical degrees. The below *Table 2 - Commutation Table*, can be built to describe the relationship between the sensor status and stator winding excitation, which is called a commutation table. Using the commutation table, the Motor control unit (MCU) can easily control the commutation. <sup>[1]</sup>

Table 2 - Commutation Table

Hall sensors			Phase		
a	b	c	A	B	C
0	1	1	NC	+	-
0	0	1	-	+	NC
1	0	1	-	NC	+
1	0	0	NC	-	+
1	1	0	+	-	NC
0	1	0	+	NC	-



## 2.4. Principle of Sensor-less control

The concept of this application is that of a speed-control for a closed loop drive using Back-EMF Zero Crossing technique for position detection. It serves as an example of a sensor-less BLDC motor control system using a Digital Signal Controller (DSC).

As explained in the previous section, the rotor position must be known to control a brushless DC motor. If sensors are used to detect the rotor position, the acquired information must be transmitted to a control unit. Therefore, additional connections to the motor are necessary. This may not be acceptable for some applications. There are at least two reasons to remove the position sensors:

- It is not possible to make additional connections between the position sensors and the control unit
- Cost of position sensors and wiring

The sensor-less BLDC motor control - sometimes referred to as sensor-less trapezoidal control of BLDC motors - uses a back-EMF (BEMF) to determine the absolute position of the rotor of the motor (the rotating part of the motor with respect to the stator).

A voltage applied across the motor winding forces the rotor to rotate. However, the movement of the rotor through the magnetic field of the stator is analogous to the behavior of a generator. As a result, the motor not only receives an applied voltage but also generates its own voltage. This voltage is referred to as counter electromotive force or back EMF and is proportional to the motor speed. [13]

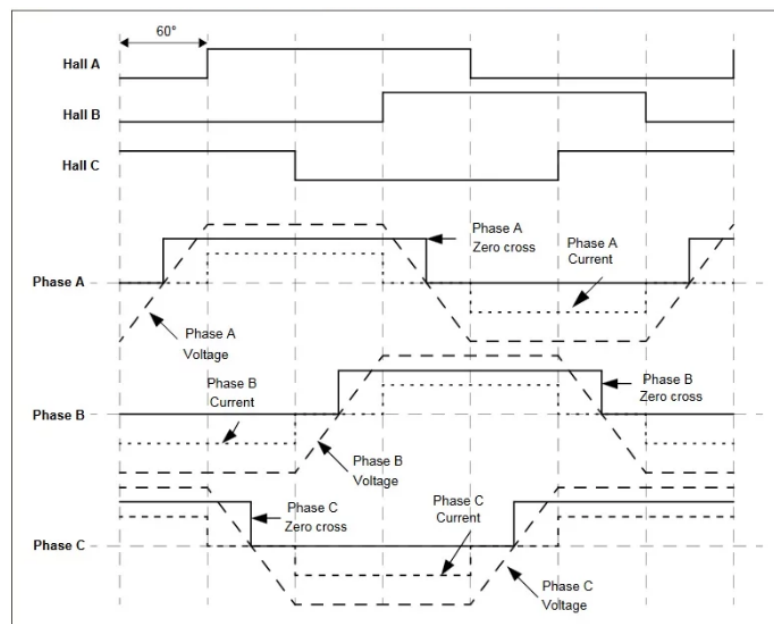
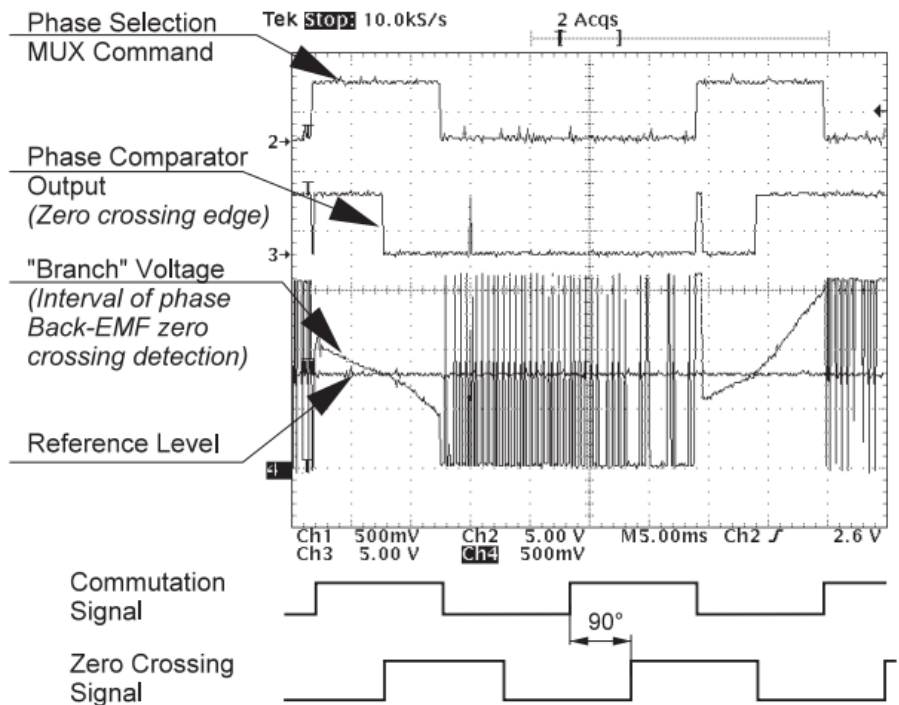


Figure 2.16 - Hall-effect sensor waveforms with back-EMF trapezoidal waveforms [13]

Back EMF can be used to determine the rotor speed and position of a motor. There are no sensors required. Controlling a motor using EMF is not an easy task. Most sensor-less BLDC motors are controlled by a microcontroller, a digital signal processor, or a dedicated driver IC.

The concept in *Figure 2.16* was chosen. The developed sensor-less rotor positioning technique detects the zero-crossing points of back EMF induced in the motor windings. The phase transition point zero-crossing points are detected while one of the three phase windings is not energized. The information obtained is processed to commutate the energized phase pair and to control the phase voltage using pulse width modulation.



*Figure 2.17 – Zero-crossing detection<sup>[12]</sup>*

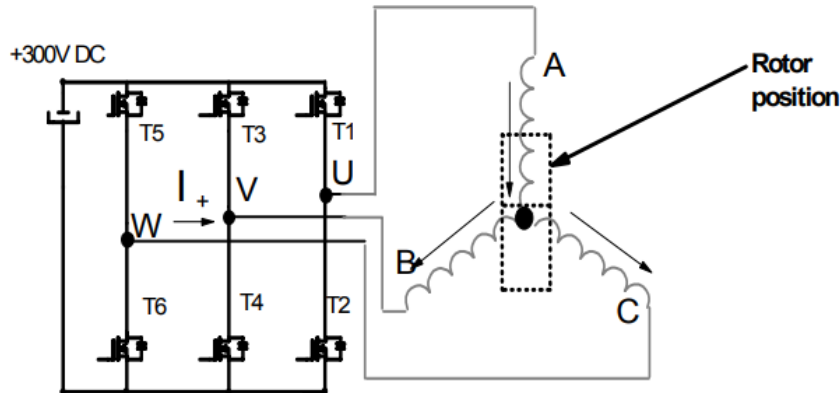
As explained earlier in this chapter, note that the phase zero crossing event can be detected at the moment when the branch voltage (of a free phase) crosses the half DC-bus voltage level. The comparators sense the zero-voltage difference of the input signal. The encoder selects the phase comparator output, which corresponds to the current commutation stage. This Zero Crossing Detection signal is transferred to the Decoder as an input. The comparator control and zero crossing signals plus the voltage waveforms are shown in *Figure 2.17*.

## 2.5. Start-up control

### 2.5.1. Prepositioning Phase

In sensor-less mode, the position of the rotor before starting the motor is not known. A prepositioning phase is needed in this case either to determine the position of the rotor or to place it in a known position.

In the pre-positioning phase, the goal is to bring the rotor into a specific, known position. During this entire phase, a constant current direction is maintained in the windings that moves the rotor to the desired position. See *Figure 2.18*.



- *Figure 2.18 - Prepositioning rotor alignment*<sup>[12]</sup>

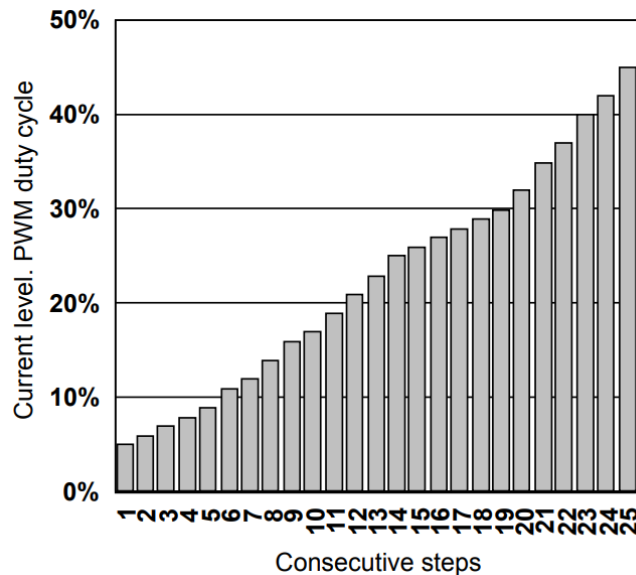


*Figure 2.19 - Prepositioning current ramp*<sup>[12]</sup>

To reduce the oscillations of the rotor when approaching its starting position, the applied voltage to all windings is increased in steps (see *Figure 2.19*). This means that all windings are energized during the pre-positioning phase. This is an intermediate position between two of the six step positions. <sup>[13]</sup>

During the pre-positioning phase, the switches T1, T4 and T6 are turned on. It means that upon creating a current in this configuration, it will be positive in phase A and negative Phases B and C at half the value of phase A. This will bring the rotor into the intermediate position.

## 2.5.2. Starting Ramp

As soon as the rotor is in the starting position, a starting ramp table is applied to the motor as per *Figure 2.20*. The intent of this ramp table is to accelerate the motor to detect the backward EMF zero-crossing information as fast as possible in order to switch to the automatically commutated mode. (see *Figure 2.21*). This ramp table consists of continuously decreasing step times which are applied to the motor. Some user-specified conditions required by the microcontroller must be met to allow the motor to switch to the automatically commutated mode. (eg. Number of zero-crossing detections)

The six-step drive consists of a succession of six different step configurations.

step 1: switches T1 and T4

step 2: switches T1 and T6

step 3: switches T3 and T6

step 4: switches T3 and T2

step 5: switches T5 and T2

step 6: switches T5 and T4

Then the process goes back to step 1 etc....

This step configuration sequence will make the rotor turn in the counter-clockwise direction after the prepositioning phase. <sup>[13]</sup>

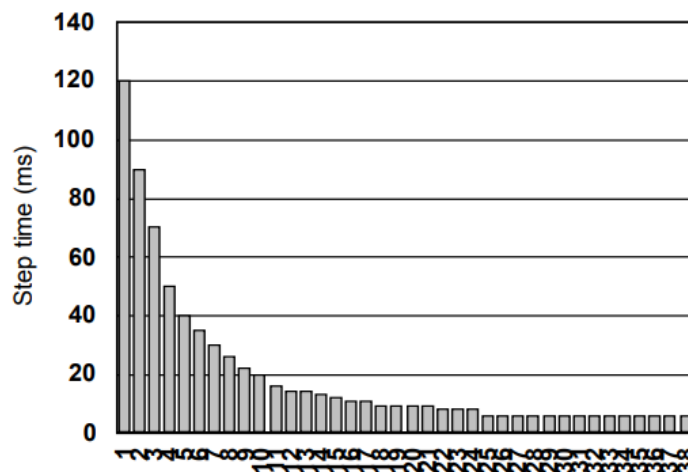


*Figure 2.20 – Starting ramp*<sup>[12]</sup>

The difficulty in defining the correct starting ramp table for a motor lies in the fact that the sequence of decreasing step times must speed up the motor enough to detect a signal for zero-crossing event. This must occur even after the forced synchronous mode and continue to receive the target number of consecutive events to switch to the automatically commutated mode. In the same manner as for the pre-positioning ramp, the waveform of the starting ramp table depends on the rotor inertia & motor load. [13]

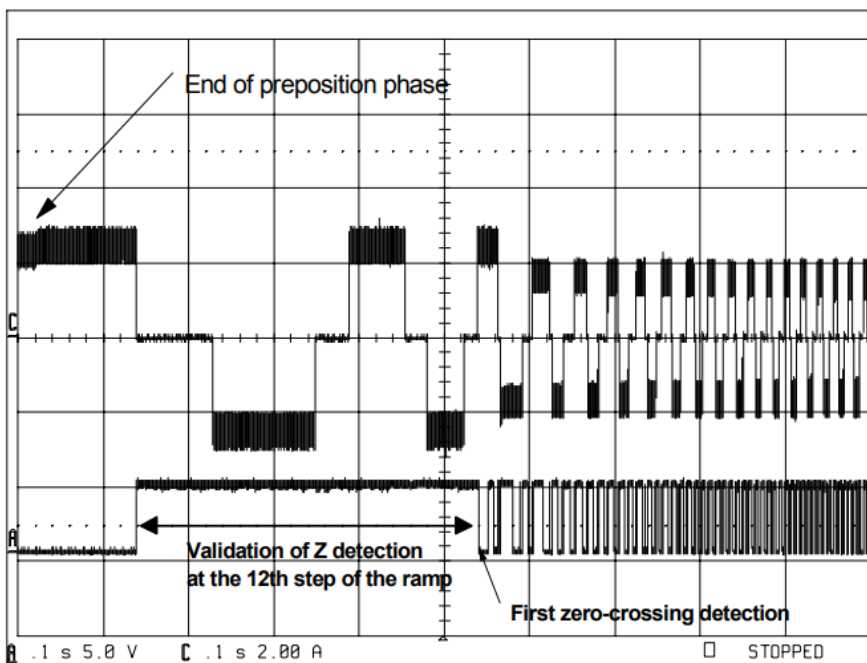
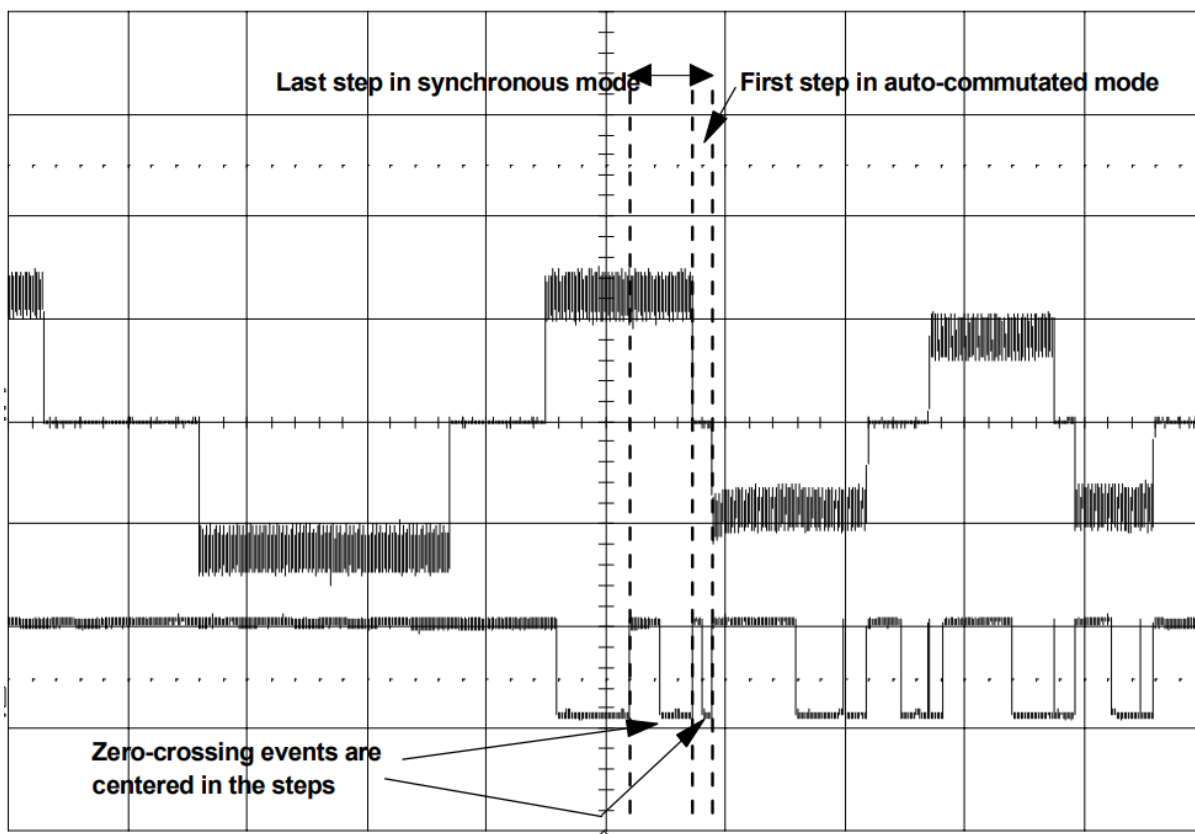


Figure 2.21 - Stator BEMF during starting ramp<sup>[12]</sup>

### 2.5.3. Switching To Auto-Commutated Mode

At the end of the start sequence, once the microcontroller has detected the target number of zero-crossing events, it switches to auto-commutated mode. This switchover is very important for the motor behavior.

For example, as can be observed in *Figure 2.22*, upon having set a target of two consecutive zero-crossing events before switching to auto-commutated mode, when the microcontroller detects the second one, it will memorize that the motor is in its last step in synchronous mode. <sup>[13]</sup>



*Figure 2.22 – Switching to Auto-commutated mode<sup>[12]</sup>*

## 2.6. Space Vector Pulse Width Modulation

Space Vector Pulse Width Modulation (SV-PWM) is a modulation scheme used to apply a specific voltage vector to a three-phase electric motor (permanent magnet or induction machine).<sup>[14, 15, 16, 17, 18]</sup>

The goal is to use a steady-state DC voltage and to emulate a three-phase sine wave waveform with six switches (eg, transistors), with adjustable frequency and amplitude.

There are two challenges here:

- The only voltage level available is the DC-link voltage which can be assumed constant (at least for the sake of simplicity).
- There are only six different voltage angles available. Without middle ground. Turning a motor requires a smoothly rotating voltage vector - not a step that skips 60 degrees per step. <sup>[19]</sup>

### 2.6.1. Vector Notation for SV-PWM

In order to develop a representative Schematic for the system in *Figure 2.23*, the below simplifications can be considered–

- The DC-link voltage can be simplified so that it is constant. Normally it varies with load, but not that much during the time frames addressed herein. The supply and diode rectifier will thus not be shown.
- Now, the scenario of both transistors in one leg being open is not interesting and will not be necessary. Further, the scenario of both transistors being closed implies that the DC-link is short circuited and hence unacceptable.
- Thus, each leg of the inverter bridge can be simplified by replacing the two leg-transistors throughout the bridge by one single SPDT-switch each. This shall indicate that either the top or the bottom transistor is closed. <sup>[19]</sup>

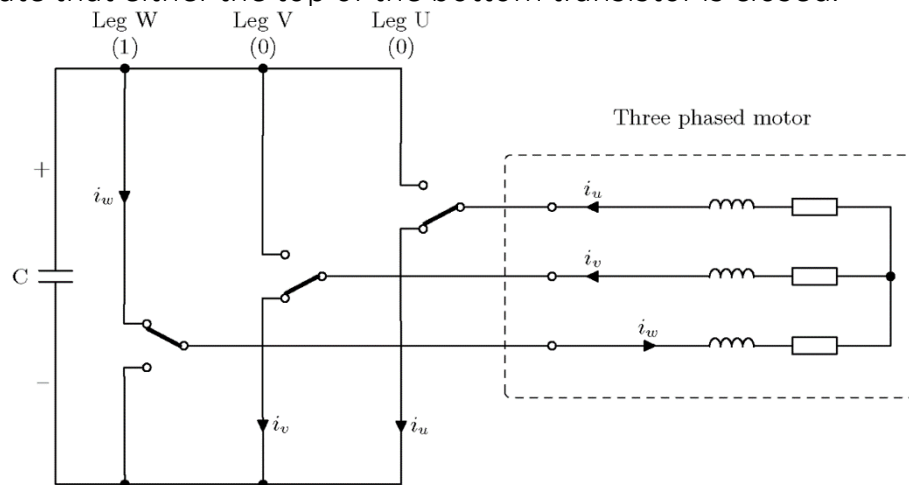


Figure 2.23 - Two Level Inverter Schematic<sup>[19]</sup>

It can now be seen from the simplified scheme that there are three switches, each of which can be in two different positions. The total number of possible switch configurations is thus  $2^3 = 8$

Six of these configurations correspond to different voltages applied to the connected motor and are called basic vectors from now on. The last two are referred to as zero vectors as they represent zero volts on the terminals. [19]

The origin of the angles for the phases can be traced to the windings physical location inside the stator. The windings are installed around the circumference at  $120^\circ$  apart. The U-phase normally forms the basis for the basic vector's angle at  $0^\circ$ . Because each winding can have positive and negative voltage, it occupies two angles at  $180^\circ$  separation, e.g.  $240^\circ$  and  $60^\circ$  is W-phase in positive and negative state respectively.

In binary, these vector combinations can be represented as eight different binary values, here named from v0 to v7:

0 0 0	-	v0	Zero Vector
0 0 1	-	v1	Phase +U
0 1 0	-	v2	Phase +V
0 1 1	-	v3	Phase -W
1 0 0	-	v4	Phase +W
1 0 1	-	v5	Phase -V
1 1 0	-	v6	Phase -U
1 1 1	-	v7	Zero Vector

Each of the three binary digits refers to one bridge leg where the value 1 indicates that the top transistor is closed whereas the value 0 indicates that the bottom transistor is closed. [19]

All eight combinations and the resulting motor voltage and current directions are shown in the *Figure 2.24*.

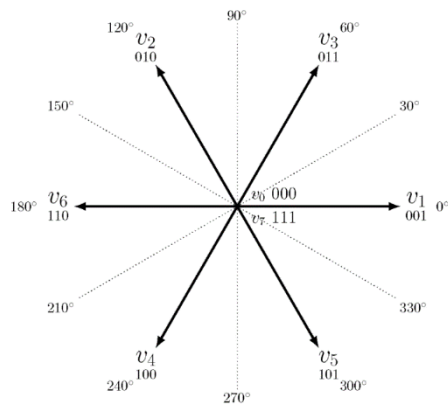


Figure 2.24 - Vector Representation [19]



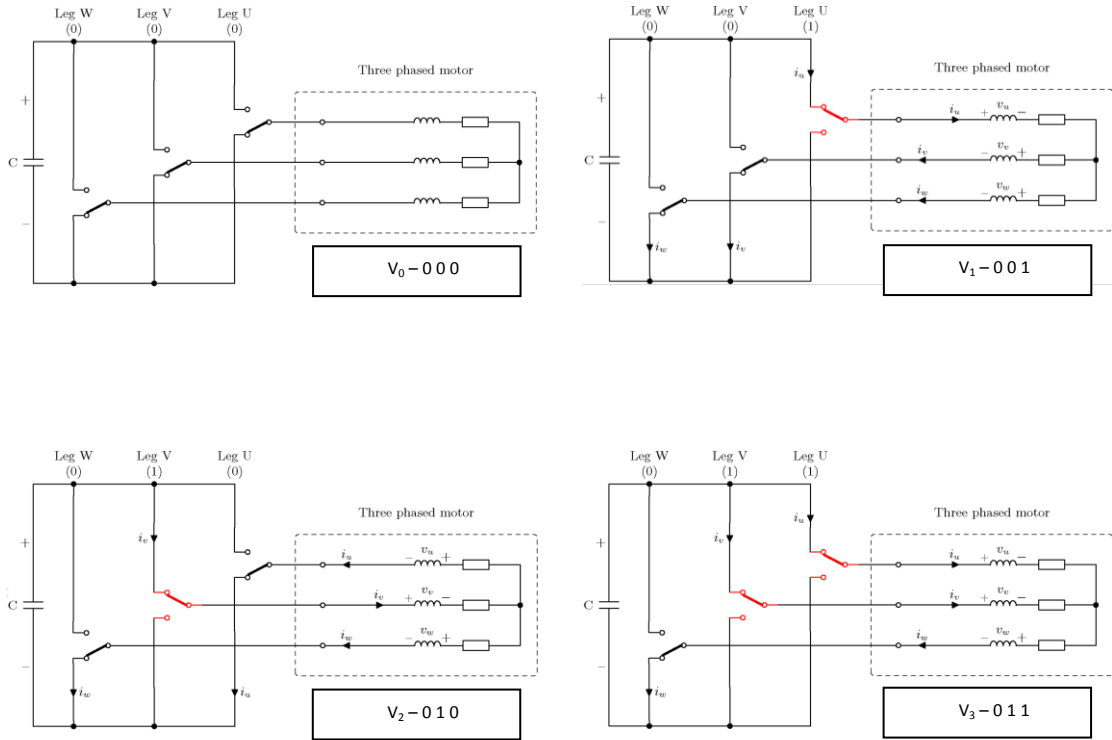
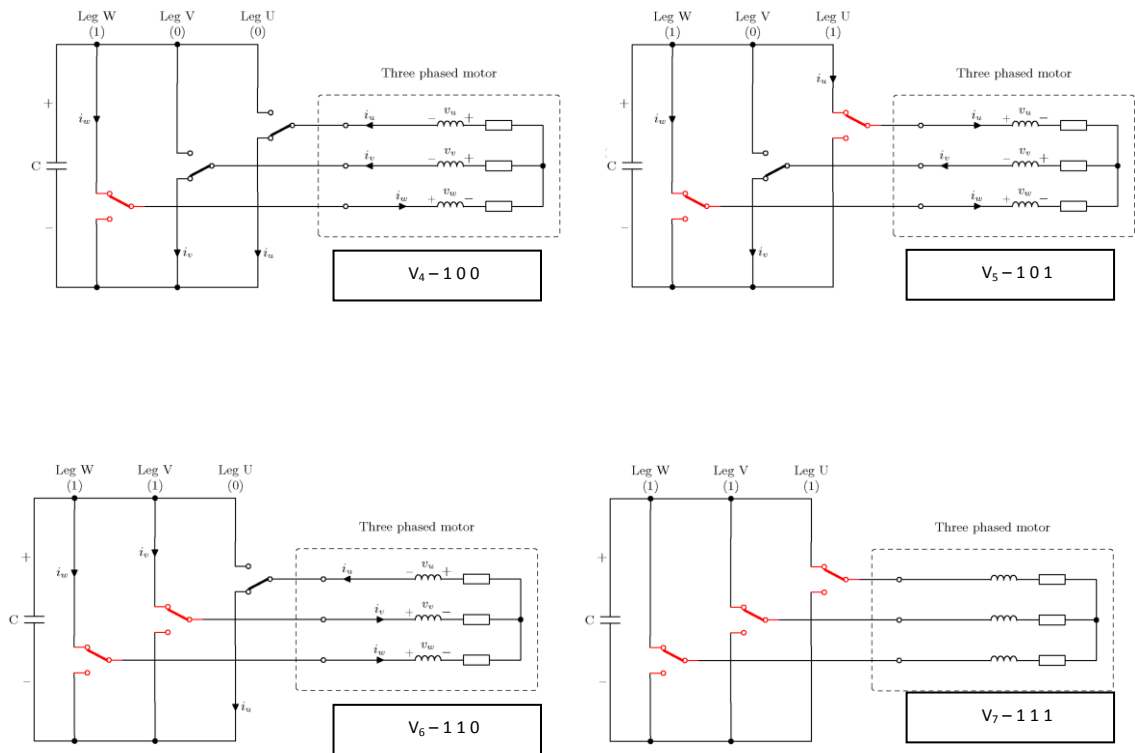


Figure 2.25 - Gate configurations for Vector Combinations<sup>[19]</sup>



## 2.6.2. Synthesizing the required output voltage

Up until this point, the discussion has addressed the possibility of how a converter can output DC-link voltage to the terminals and how each of the six usable vectors affects current- and voltage directions in the motor.

In the following section, the emphasis will be placed on how to synthesize any voltage vector by quickly alternating between adjacent voltage vectors and timing of the on- and off times.

The two zero vectors  $v_0$  and  $v_7$  are also used to add dead time to the switching pattern. This dead time reduces the voltage magnitude and is necessary when the voltage reference magnitude is less than 100%.<sup>[19]</sup>

- **Projection of a reference to the Trigonometric Wave**

In the *Figure 2.26*, the left circle is the "input" or "reference". It is what is needed to be achieved; three different voltages at different angles - together forming a space vector with one magnitude and one angle.

As seen, the U-phase (red) is close to its maximum positive value. This level is also shown on the graph to the right of the circle together with a triangle wave where it is referred to as a control voltage. The frequency of this waveform is many times higher than the frequency of the space vector. (Typically, between 1 and 20 kHz)

Similarly, the V-phase (green) is close to its maximum negative value and the W-phase (blue) just stretching out from zero in positive direction.

It is based upon how these three values are intersected with the triangular wave, that will directly translate to which switches shall be closed and how long they will remain closed.<sup>[19]</sup>

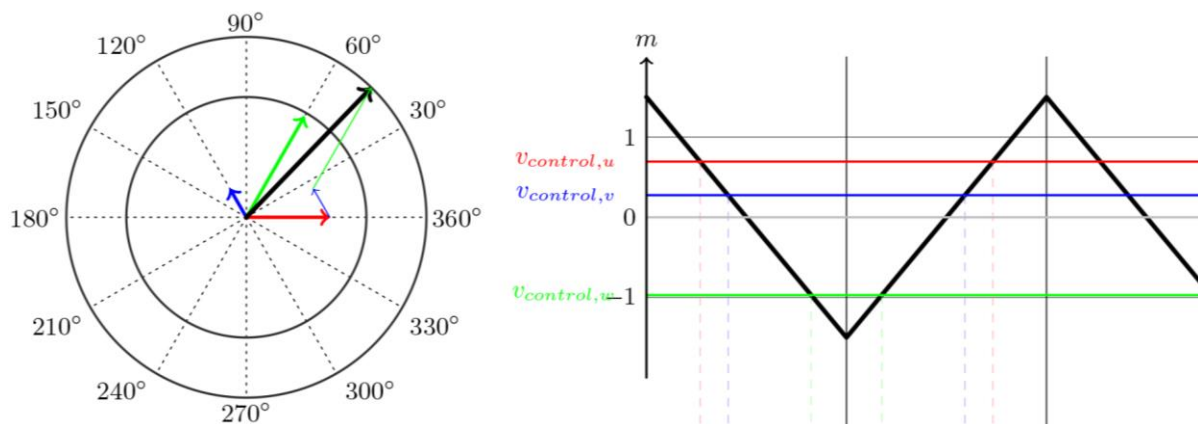


Figure 2.26 – Input Reference and Trigonometric Wave<sup>[19]</sup>

## • Translation of the reference to Switching States

The primary focuses in this section are the dashed lines protruding downwards from the triangular wave displayed in *Figure 2.26*. The dotted line representation will be used to define the proportion of the time period in the state switching frequency that shall be occupied but individual states.

These dotted lines originate from where the control voltages intersect the trigonometric wave. At all times, four different sections are visible below the W-axis right above the  $0.5xT$  arrow. For other space vector angles and magnitudes, the width of these four sections change, but the total width will always be the same.

At the angle in *Figure 2.27*, the first dashed line is the red one. There are no active voltage vectors between the start of the three axes and the red line. All three control voltages in this region are below the trig wave. This means that all switches are off. (000, Zero vector  $v_0$ )<sup>[19]</sup>

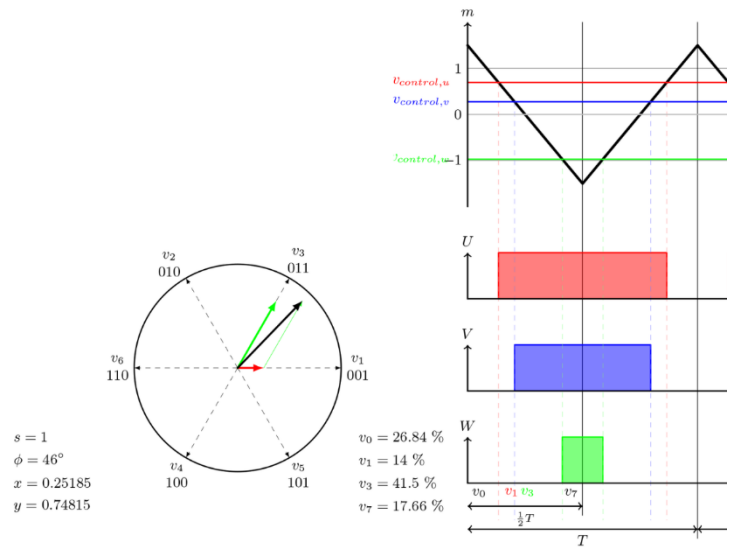


*Figure 2.27 - Switching State Vectors*<sup>[19]</sup>

In a similar manner, the vectors  $v_1$ ,  $v_3$  and  $v_7$  can be realized that as 001, 011 and 111 respectively by associating the dotted lines generated with the active switching states.

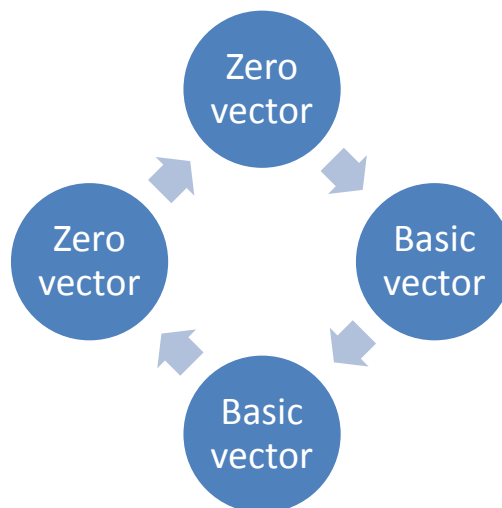


*Figure 2.28 – Switching State Pattern*

At every angle and magnitude, the same pattern as *Figure 2.28* will be seen; Zero vector - basic vector - basic vector - zero vector. Repeat. The only thing that changes is the width (i.e. the on-time) of these sectors and which of the six basic vectors are used.

## • Emulation of Space Vectors

The two vectors between which an alternation must be achieved are now known between is v1 and v3.

By getting the on-times correctly, this will emulate a voltage vector at the same angle as the input voltage space vector.<sup>[20]</sup>

$$T_1 = \frac{\sqrt{3} \cdot T_z \cdot |\overline{V_{ref}}|}{V_{dc}} \left( \sin \left( \frac{\pi}{3} - \alpha + \frac{\pi \cdot (n-1)}{3} \right) \right) \quad \text{---- (7)}$$

$$T_2 = \frac{\sqrt{3} \cdot T_z \cdot |\overline{V_{ref}}|}{V_{dc}} \left( \sin \left( \alpha - \frac{\pi \cdot (n-1)}{3} \right) \right) \quad \text{---- (8)}$$

$$T_0 = T_z - T_1 - T_2 \quad \text{---- (9)}$$

Here,

T1	----	On time for basic vector 1
T2	----	On time for basic vector 2
T0	----	On time for zero vector
Tz	----	Time period for the switching frequency
$V_{ref}$	----	R.M.S. Reference voltage
$\alpha$	----	Rotor Angle
n	----	Sector number ranging from 1 – 6 in increments of 60°

## • Emulation of switching states

The two different switching combinations (basic vectors) which the drive will alternate between are shown in *Figure 2.29*. Above each configuration, the comparative total on-time for both basic vectors is indicated in the progress bar i.e, how long they are on relative to each other.

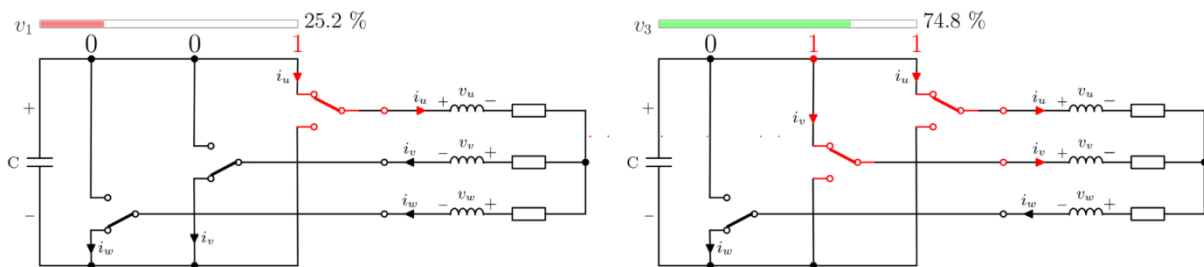


*Figure 2.29 - Relative time on for switching state<sup>[19]</sup>*

Additionally, the zero-vectors come in and increase for lower voltage levels. This allows for a modulation of the overall output.

For example, if the angle is midway between two basic vectors (i.e.  $30^\circ$ ), both basic vectors would be turned on for 50% of time each. This however does not indicate their total on time with respect to the period  $T$  of switching states. If the voltage magnitude is less than the maximum, zero-vectors are added to average down the voltage. So, at 70% voltage and  $30^\circ$  orientation, the ON-time of each basic vector is still 50% with respect to each other, however in total there would be 30% zero vectoring within this period. The actual on-time for each transistor thus becomes 35%. <sup>[19]</sup>

$$T = T_{v1} + T_{v3} + T_{v0} + T_{v7} = 35\% + 35\% + 15\% + 15\% = 100\%$$

---- (10)

## 2.7. Third Harmonic Injection

### 2.7.1. Purpose

Consider the available voltage at inverter terminals. These are not readily apparent but however play a major role in the optimization of the system. They depend on many factors including the averaging of the different vectors and the modulation index.

Suppose the grid voltage that the inverter is connected to is

$$V_{\text{grid,RMS}} = 690 V_{\text{RMS}} \quad \text{---- (11)}$$

The resulting DC – DC link voltage would be found as

$$V_{\text{DC}} = V_{\text{grid,RMS}} \times \sqrt{2} = 975.8 V \quad \text{---- (12)}$$

This is the synthesis level that can be achieved as an output.

In a system of SV-PWM, there are a set of 6 basic vectors with their magnitude as

$$V_{|1-6|} = V_{\text{DC}} \quad \text{---- (13)}$$

Knowing this a *Figure 2.30* can be prepared representing the phasor of the 6 basic vectors and connecting the vector tips leads to the famous space vector hexagon.

The circle inside the hexagon represents the maximum size permissible in it and thus the maximum RMS voltage can then be found as

$$V_{\text{max,RMS}} = V_{\text{DC}} \times \cos 30 \times \frac{1}{\sqrt{2}} = 579 V \quad \text{---- (14)}$$

Here, a lacking is found in the output considering that the grid voltage was found to be 690 V. <sup>[19]</sup>

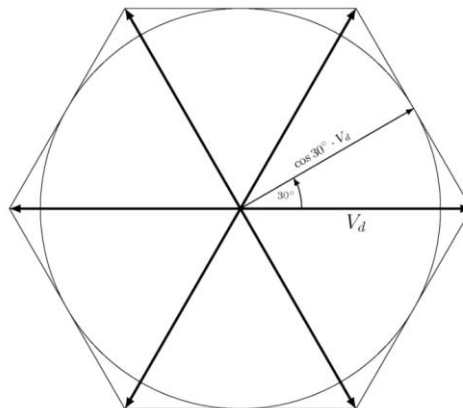


Figure 2.30 - Space Vector Hexagon<sup>[19]</sup>

## 2.7.2. Strategy for optimization

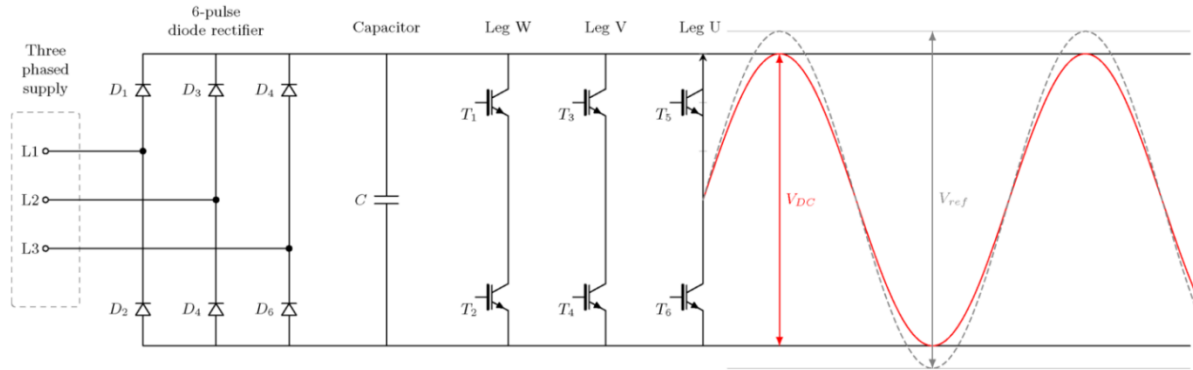


Figure 2.31 - Control without Third harmonic injection<sup>[19]</sup>

In the above Figure 2.31, it is apparent that the maximum voltage of the DC-link has to be the DC-link voltage. In the figure, it has been shown as a red sine wave having a peak-to-peak voltage equal to the V<sub>DC</sub> = 975 V. Similar to the previous section, the RMS phase-to-phase can then be found as

$$V_{\max,RMS} = \frac{V_{DC}}{2} \times \sqrt{3} \times \frac{1}{\sqrt{2}} = 579 \text{ V} \quad \text{---- (15)}$$

The purpose of this strategy is to try re-gaining the lost 15% that was lost and reach the 690 V of the DC-Link ceiling. The methodology adopted in order to achieve this is attributed to an engineer from GE by injecting a Third Harmonic wave.<sup>[19]</sup>

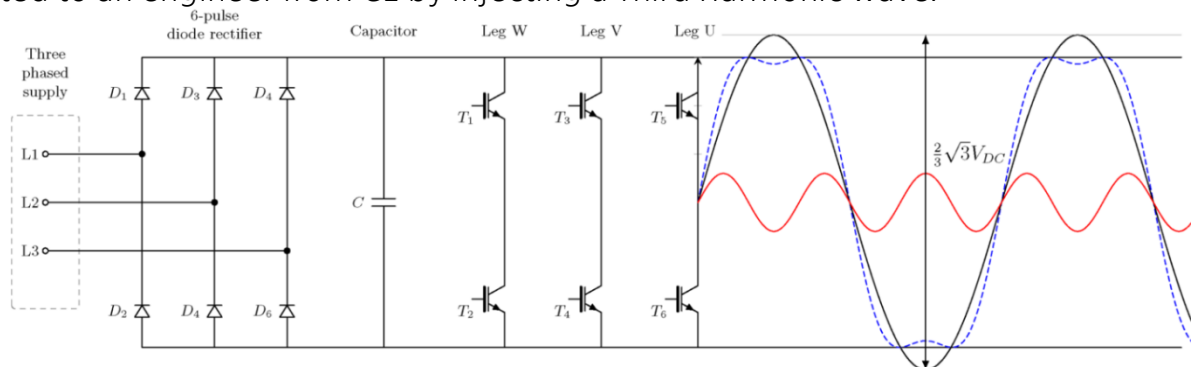


Figure 2.32 - Control without Third harmonic injection<sup>[19]</sup>

Consider an individual phase as shown in the above Figure 2.32. The addition of the third harmonic wave leads to a loss of the smooth sine wave. The Fourier expansion of the above dotted blue wave leads to the formation of the black and red wave.

Superimposing all of the three phase voltages together, it can be found that the result is that all the waves have a common mode which is the common black third harmonic wave seen in the Figure 2.33.

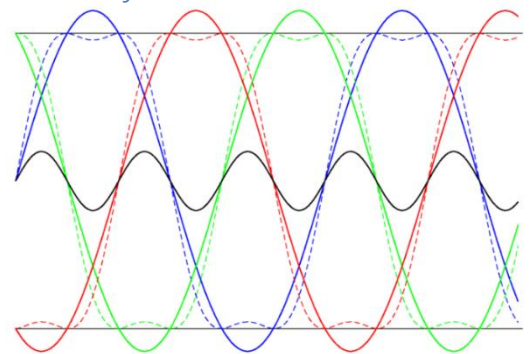


Figure 2.33 - Superposition of three phases<sup>[19]</sup>

The Phase-to-neutral voltage can now be found to have the exact opposite effect as the phase voltage. It can be observed that all parts of the motor including the neutral point are found to be oscillating at the frequency and amplitude of the Third harmonic wave. The Logic of how this leads to the complete inclusion of the third harmonic into the supply goes as below

$$\begin{aligned} &\text{Phase supply wave} - \text{Third Harmonic wave} = \\ &= (\text{Large sine wave} + \text{Third Harmonic wave}) - \text{Third Harmonic wave} = \\ &= \text{Large sine wave only} \end{aligned}$$

### **2.7.3. Modulation index**

The modulation index can be thought of as a scaling factor that can be applied to the amplitude of the voltage. After the inclusion of the third harmonic into the system the range of this modulation now spans from 0 – 115.4 %

$$V_{\text{max,RMS}} = \frac{V_{\text{DC}}}{2} \times \sqrt{3} \times \frac{1}{\sqrt{2}} \times m \quad \text{---- (16)}$$

Where m = Modulation index

### **2.7.4. Over-Modulation and its purpose**

Over-Modulation refers to the state where the modulation index is increased to a value beyond that of 115.4%. At this point, it will effectively get rid of the zero vectors and also increase the presence of the other control voltages for longer periods in each sector.

This leads the inverter to keep cutting the sine wave and distort it until finally a method of control called the Six-step will begin to occur. This is the control strategy that was being avoided in the first place!!

The 60-degree steps and square wave operation leads to a much higher choppy and noisy operation. However, this is occasionally needed as in case of a high current need situation. In such a situation where the motor is at full power and speed, the increase in current demand leads to even the low resistances of the inverter to cause a large voltage drop in accordance to Ohm's Law and thus requires an added modulation to keep the motor flux at rated value.

This leads to heating of the motor windings and acoustic noise. It must also be taken into account that while this will cause substantial wear in Induction motors. For the case of BLDC motors, they are designed substantially to withstand this mode of operation. <sup>[19]</sup>



## 3. Proposed Control Strategies

### 3.1. Using reference active and reactive current

The overall workflow for this strategy can be seen as below *Figure 3.1* and *Figure 3.2*

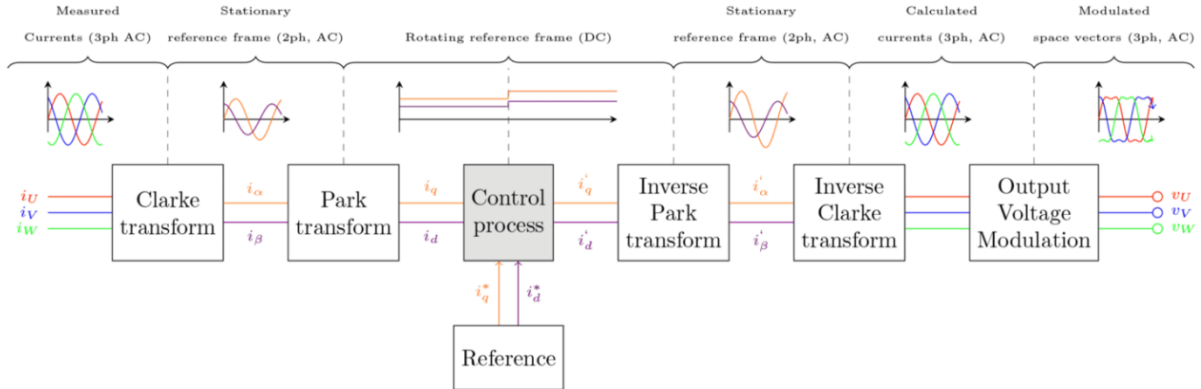


*Figure 3.1 - Using reference active and reactive current*

Here, the control process represents a PID or PI controller that is controlling the Active current and Reactive current. These two basic parameters relate to the torque and magnetic flux respectively and are generated by using the Park-Clarke transformation technique.<sup>19<sup>[19]</sup></sup>

#### 3.1.1. Control Process

- Step 1

Measure the current and voltages

- Step 2

Estimate the rotor position from above measurements

- Step 3

First the three phase current can be transformed to torque producing and flux producing current using the Clarke transformation

$$i_{\alpha} = \frac{3}{2} \cdot i_U \quad \text{---- (17)}$$

$$i_{\beta} = \frac{\sqrt{3}}{2} \cdot i_V - \frac{\sqrt{3}}{2} \cdot i_W \quad \text{---- (18)}$$

where  $i_U, i_V$  and  $i_W$  represents the three phase currents out of the inverter and  $i_{\alpha}$  and  $i_{\beta}$  represents the two "new" currents for torque and flux respectively.

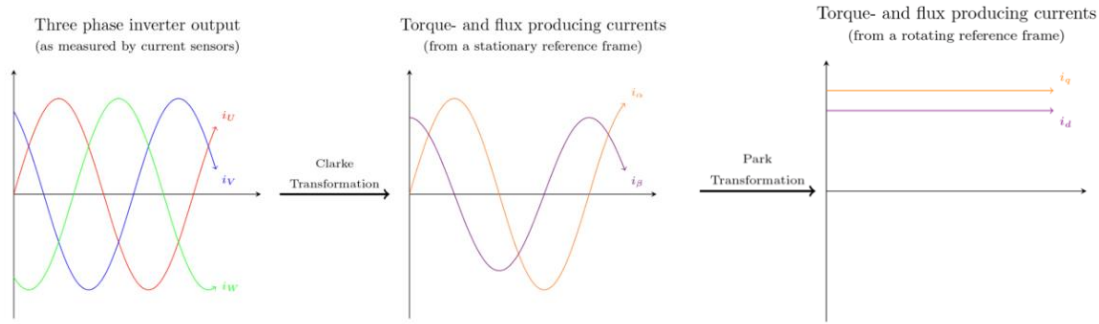


Figure 3.2 - Transformation process

- Step 4

The new torque and flux producing currents are still generated with a stationary reference frame and hence is sinusoidal in nature. This can then be transformed to a steady state current by Park transformation. This can be achieved since the position of the rotor is known and hence the current can be transformed to a rotating reference as below

$$i_q = -i_\alpha \cdot \sin\theta + i_\beta \cdot \cos\theta \quad \text{---- (19)}$$

$$i_d = i_\alpha \cdot \cos\theta + i_\beta \cdot \sin\theta \quad \text{---- (20)}$$

where  $i_q$  and  $i_d$  are the torque producing and flux producing DC currents and  $\theta$  is the rotor angle.

- Step 5

Apply control process to generate new torque and field producing DC currents

- Step 6

Apply reverse Park-Clarke transform to generate modulated space vectors.

- Step 7

Start Over

### 3.1.2. Advantage

The main advantage of using the active and reactive currents in the control of the system is that it leads to a relatively ideal control of the motor. This method allows minimizing the Flux generating current by controlling the advance of the rotating field over the rotor and thus optimizing the utilization of the torque producing current.

## 3.2. Using reference speed (Direct voltage modulation)

In the voltage modulation method as discussed in section 7.3, the voltage undergoes a direct scaling of phase voltages. This method prioritizes all control with respect with the rotor position and speed. It keeps a fixed advance for the magnetic field of the stator from the rotor to a calibrated value. The PID or PI controller then controls the modulation to generate a torque to match the required load and output speed.

The modulation period for basic vectors mentioned in section 6.2.3 can now be recalculated as below for SV-PWM<sup>[19]</sup>

$$T_1 = m \cdot \frac{\sqrt{3} \cdot T_z \cdot |\bar{V}_{ref}|}{V_{dc}} \left( \sin \left( \frac{\pi}{3} - \alpha + \frac{\pi \cdot (n-1)}{3} \right) \right) \quad \text{---- (21)}$$

$$T_2 = m \cdot \frac{\sqrt{3} \cdot T_z \cdot |\bar{V}_{ref}|}{V_{dc}} \left( \sin \left( \alpha - \frac{\pi \cdot (n-1)}{3} \right) \right) \quad \text{---- (22)}$$

$$T_0 = T_z - T_1 - T_2 \quad \text{---- (23)}$$

Where m = Modulation index

### 3.2.1. Advantage

- The main advantage of this method is the much lower requirement it places on the motor driver computation. As the computation is required only for the control process, the speed of iterations is significantly improved.
- Improved computation times are also very significant for BLDC motors as they are generally designed to run at extremely high rpm.
- There are lower hardware requirements as there is no need for measuring the currents present in each phase
- This method is much simpler in combination with the introduction of the Third harmonic wave.

### 3.2.2. Disadvantage

The major disadvantage of the modulation method is that as the optimum angle of advance is calibrated for a particular combination of speed and load on the motor, it will lead to decreasing performance as the motor begins to defer from the set point conditions. This is a sacrifice that needs to be considered taking into account the above-mentioned advantages.

## 4. Simulation of control strategies

The following chapter describes the MATLAB simulations prepared for the control strategies that have been previously discussed in this thesis.

The models mainly deal with the control algorithm and strategy rather than the actual parameterized motor for a specific system. This is mainly due to the fact that this thesis mainly pertains to a general purpose research in the control of BLDC motors with the intention of application in Electric vehicle drive trains. The need here is that of proving adaptability of the algorithm to be calibrated to the final system parameters and still yield the results as predicted by the results.

Taking the above approach in mind, control strategies have been developed as per the researched algorithms. These algorithms however are used in the simulated powering and control of a BLDC motor model of an existing motor that has been developed in the Simulink/SimScape environment.

### 4.1. Simulink model for control with Hall Effect sensor

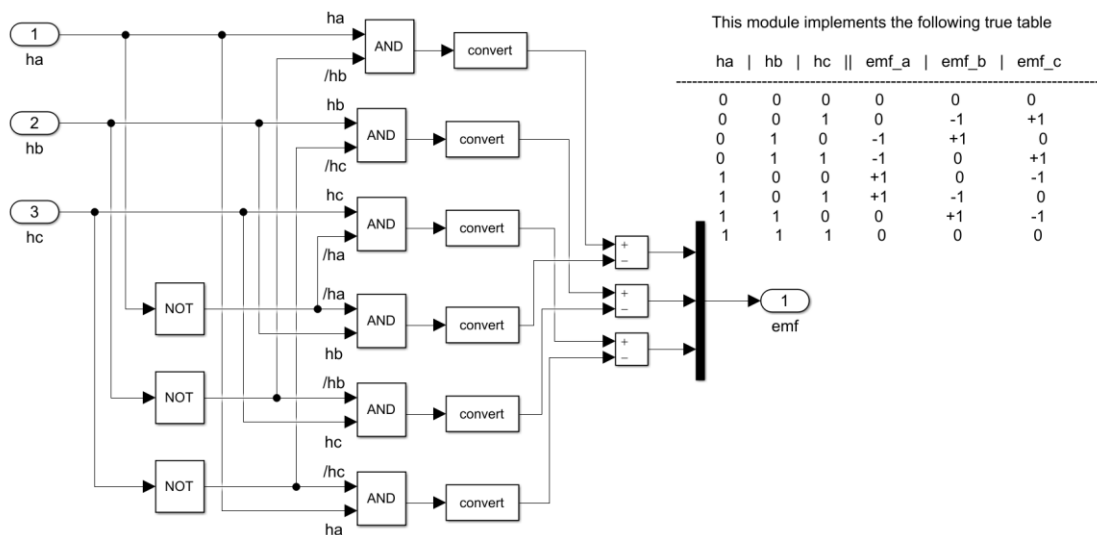
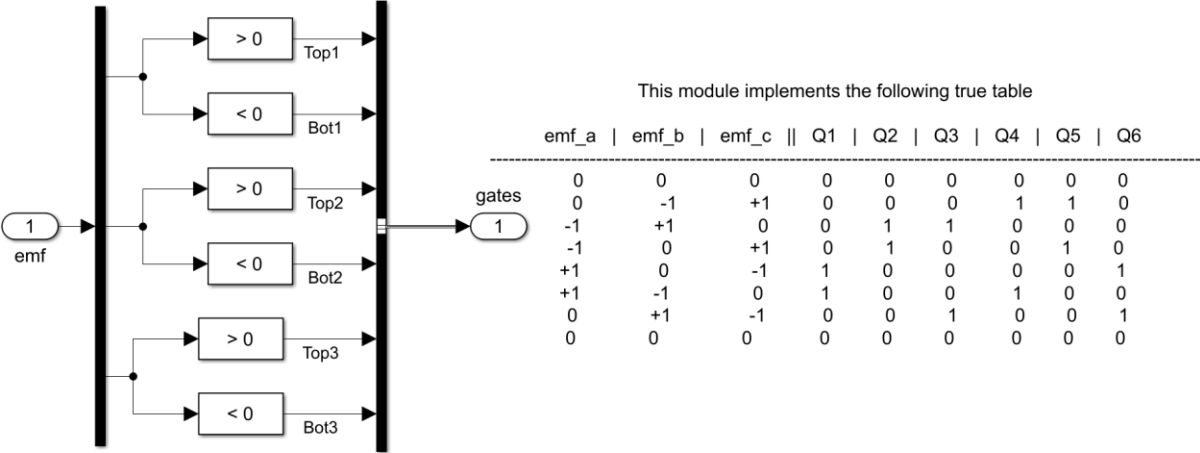


Figure 4.1 - Encoder

The encoder and decoder control logic that is used for the Hall Effect sensor-based switching of 6 -step inverter gates is based on the concept of an encoder and decoder.

The *Figure 4.1* and *Figure 4.2* describe the Simulink implementation of the encoding and decoding process. As the decoder registers the Hall Effect sensors, it generates a E.M.F. signal and this is then converted into a MOSFET gate turn on signal.<sup>[21]</sup>



*Figure 4.2 - De-coder*

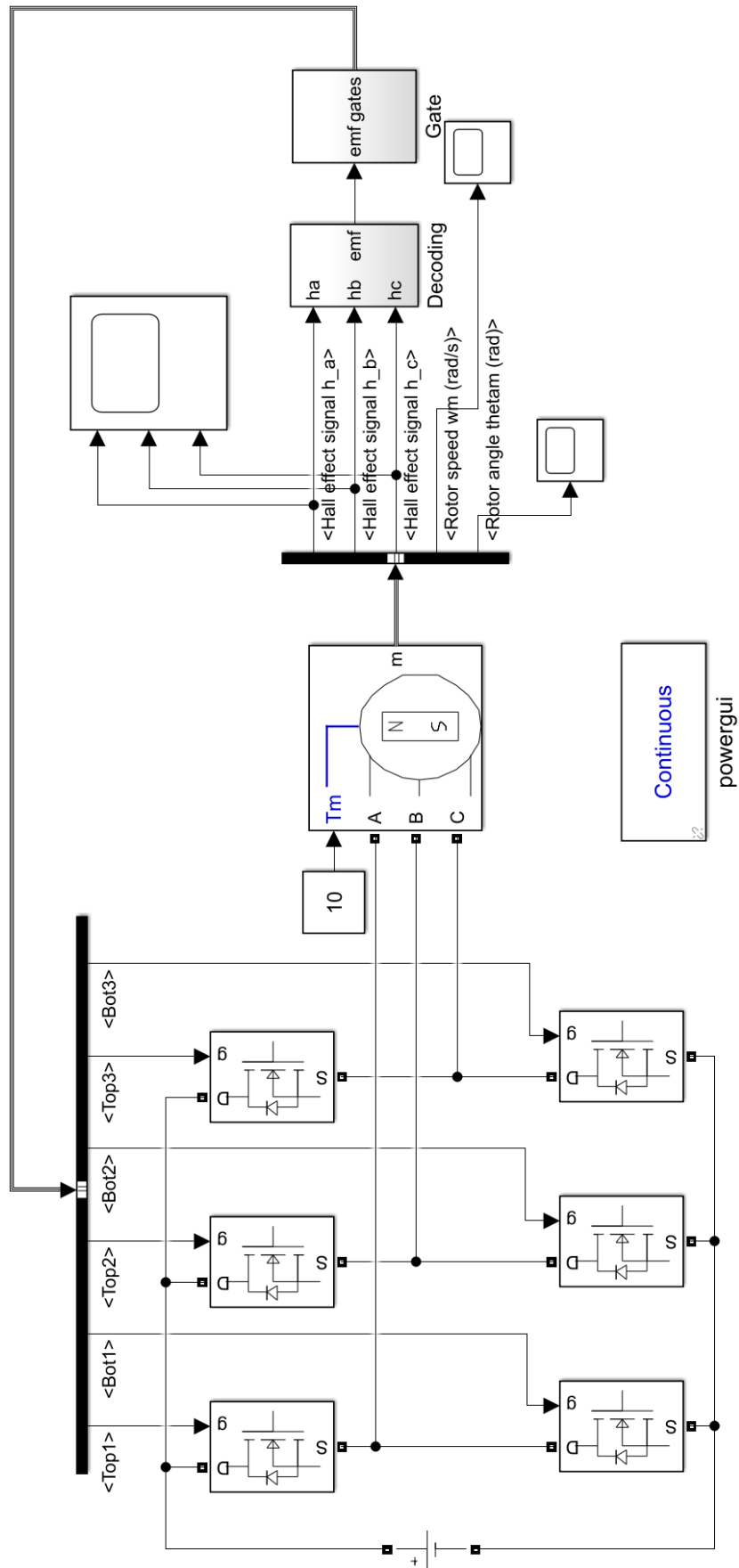


Figure 4.3 - Brushless DC Motor fed by Six Step inverter and Hall Effect sensor base control

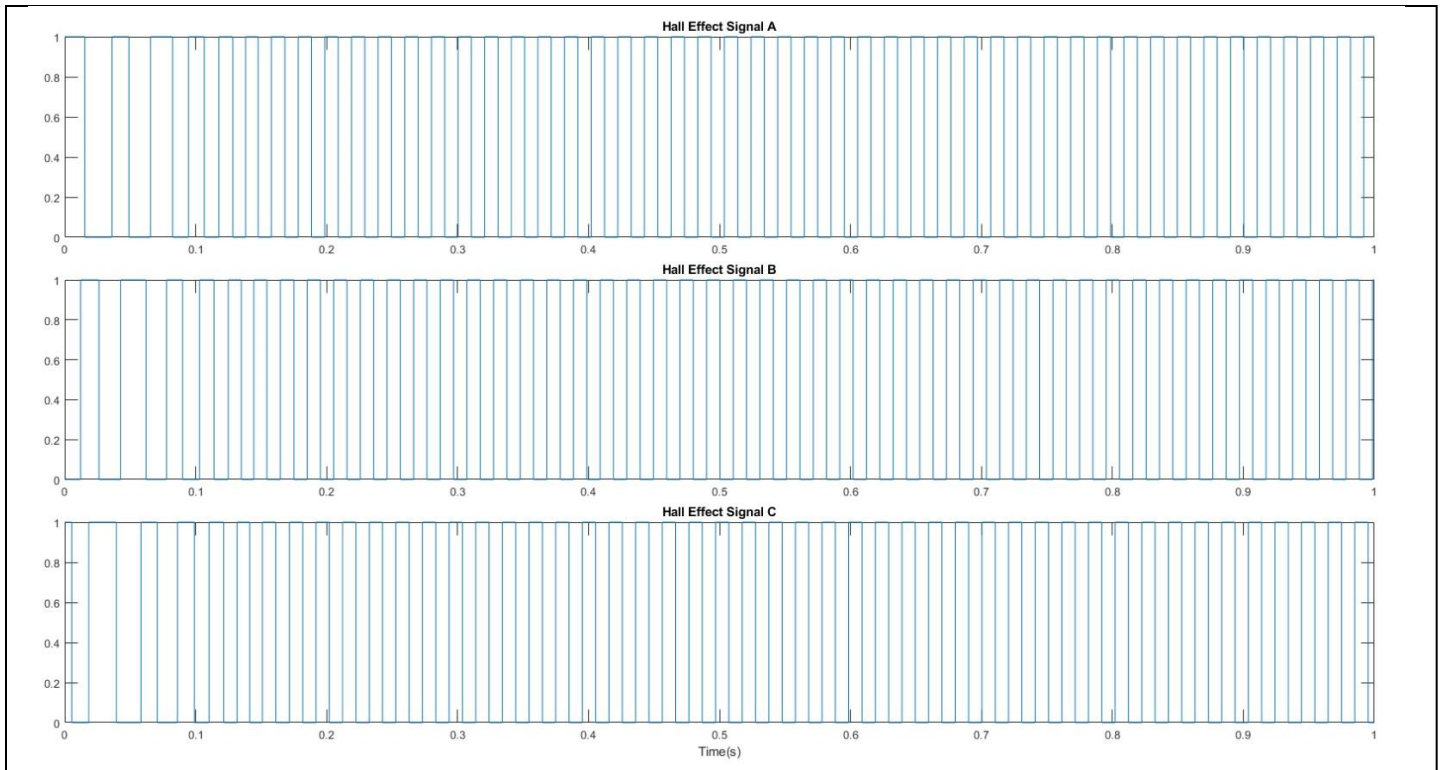


Figure 4.5 - Hall Effect Signal

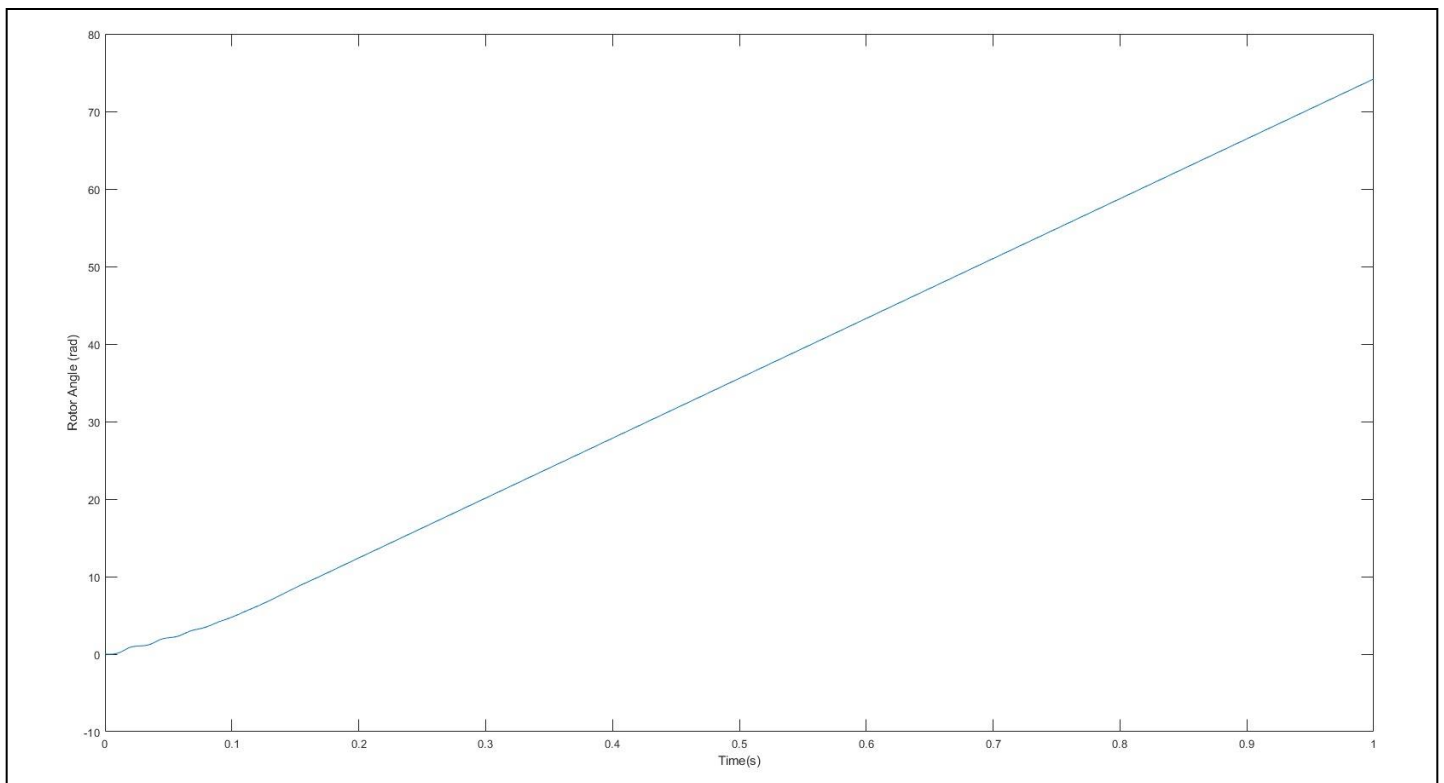
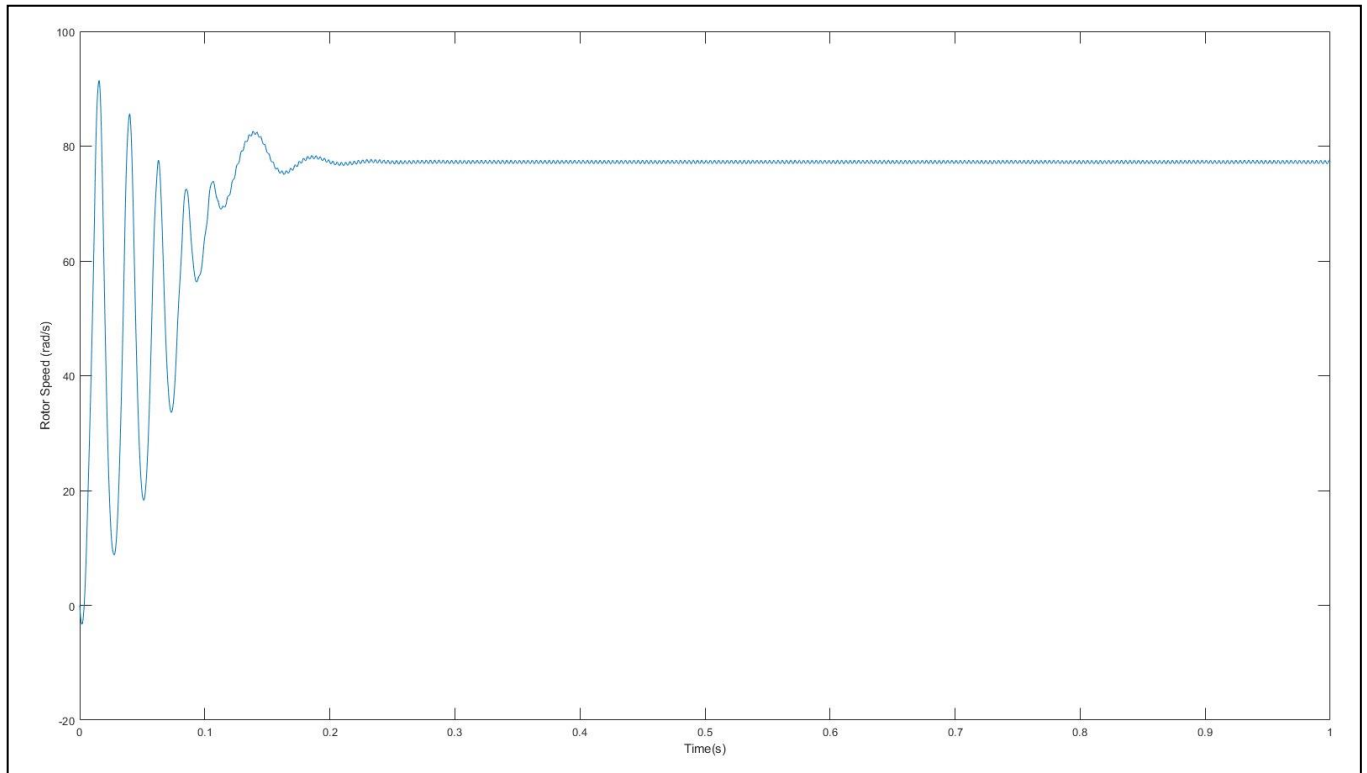


Figure 4.4 - Output Rotor Angle



*Figure 4.6 - Output Rotor Speed*

#### **4.1.1. Result**

- Speed control is achieved with the 6-step control
- The speed control is found to be relatively noisy and choppy
- The choppy nature of the speed leads to a higher level of vibration generated by the motor
- Initial start-up can include a small amount of rotation in reverse direction (limited to a few degrees)



## 4.2. Simulink model for Sensor-less control

In this chapter, the preparation of a model based on the principle of Sensor-less control has been addressed. The back EMF signal generated by the free phase of the motor can be seen in the *Figure 4.7*.

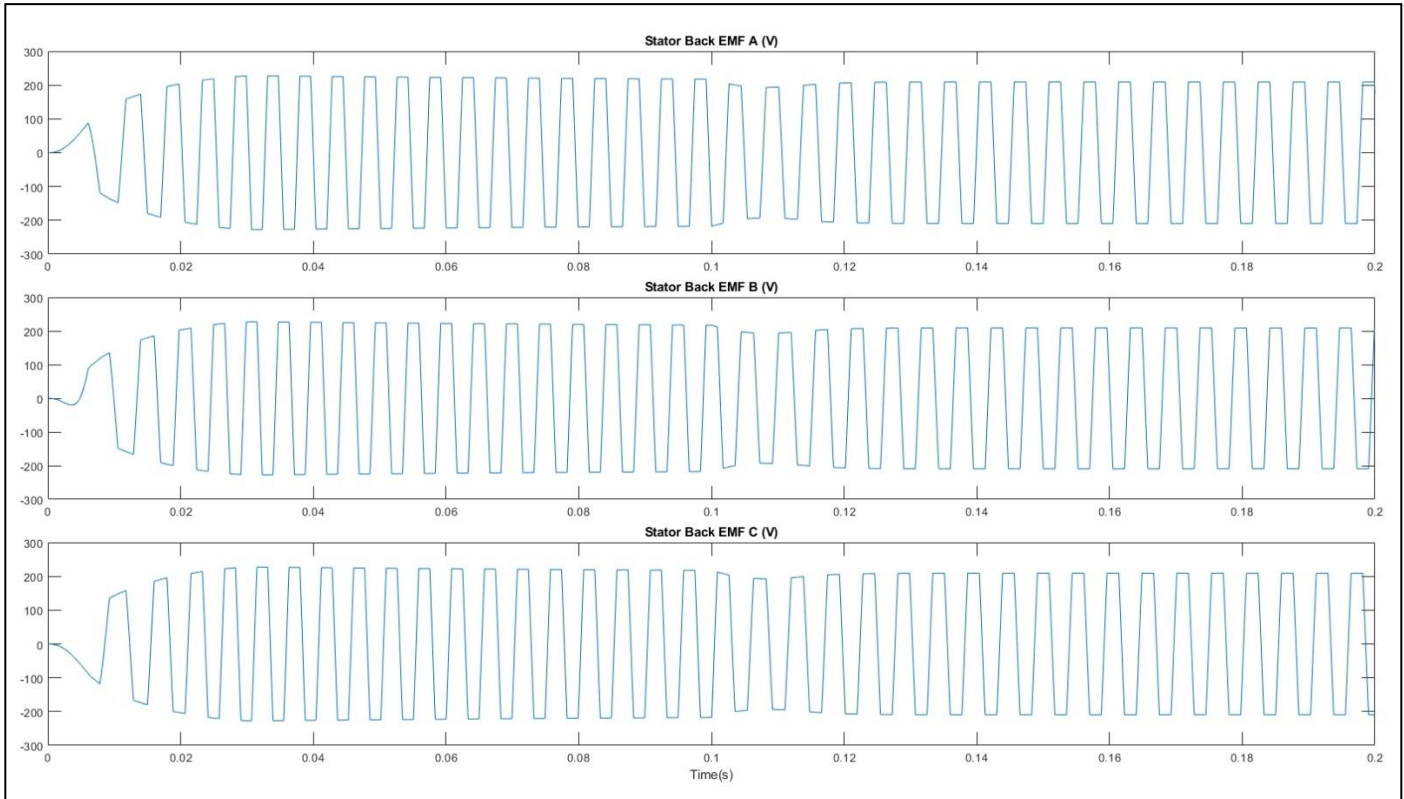


*Figure 4.7 - Back EMF cross over pulse detection Signal*

The first piece of logic approached in *Figure 4.8* is for receiving of the Back EMF reading and converting it into a viable impulse signal that can be latched onto as the transition points for the 6-step controller states. As can be seen in the figure, the goal is to try and isolate the marked point for the transition state post speed stabilization.

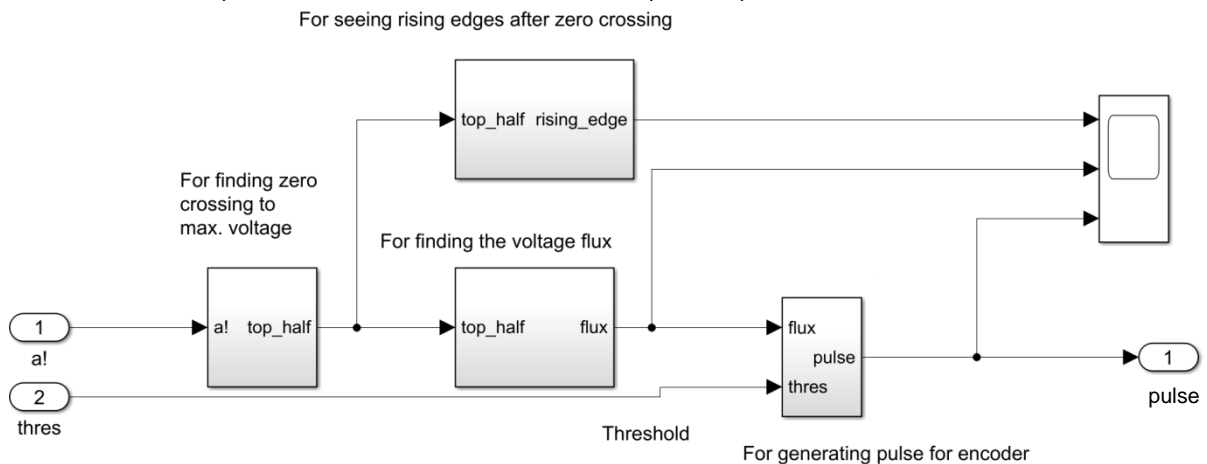


*Figure 4.8 - Edge Detection*

In *Figure 4.9*, parts of the signal that are not the upper half of the EMF signal with rising edges are cut off.

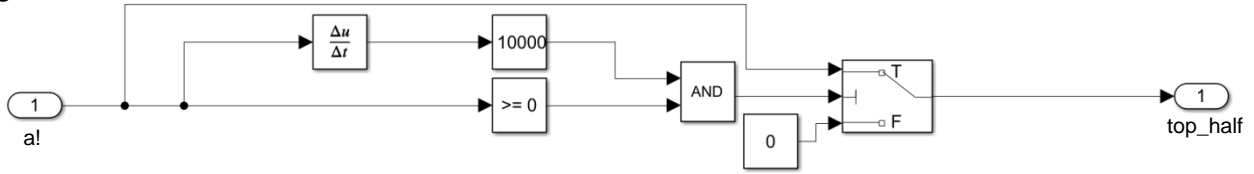


*Figure 4.9 - Top edge detection*

In the next logical step, the previously processed signal is mapped into an arbitrary flux representation value that is sensed by using integration triggered by falling edges in *Figure 4.11*. The purpose of this step is to produce a signal only after a certain set point level of flux is reached.

And finally in *Figure 4.10*, this flux value is then transformed into Impulses for state transitions of the 6-step inverter bridge.

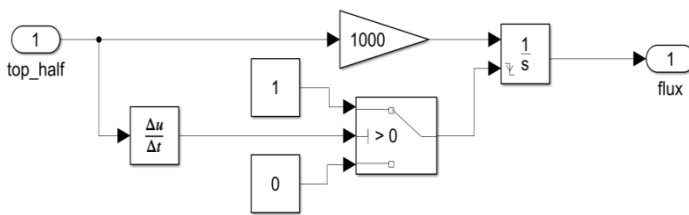


*Figure 4.11 - Rising edge detector*

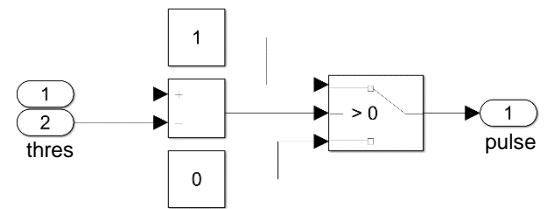


*Figure 4.10 - Pulse generator*

In the *Figure 4.12*, the three steps described above can be captured. In the first stage the top edges are detected. In the second stage arbitrary flux values are generated. In the third stage, Impulses are mapped.

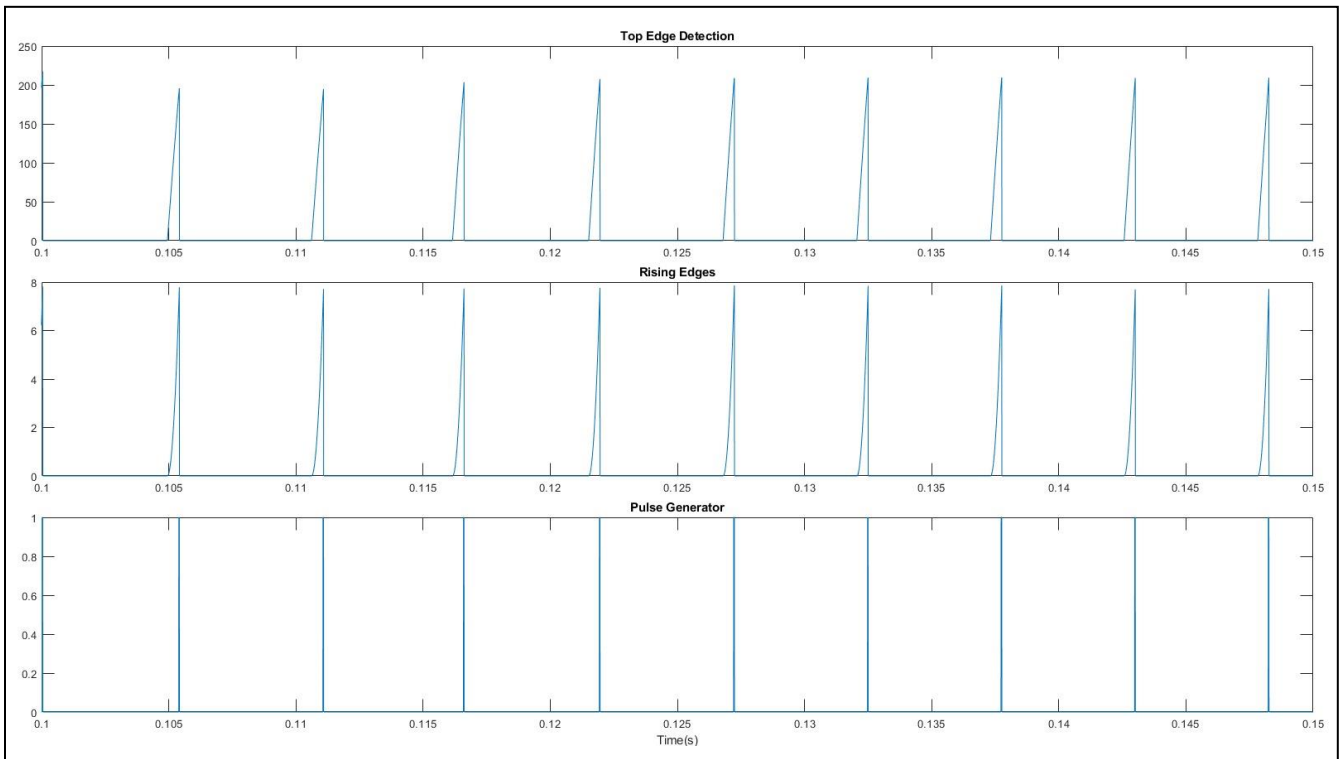


*Figure 4.12 - Edge signals*

The next stage of the logic that is captured in the simulation is to latch onto the impulse signals generated using SR Flip-Flops and the output signal generated is identical to that received from the previous Hall Effect 6-step controller in *Figure 4.13*.

Similar to the previous method, the signal is then passed through the encoder and decoder stages and hence develops the transition between the 6-step inverter stages.

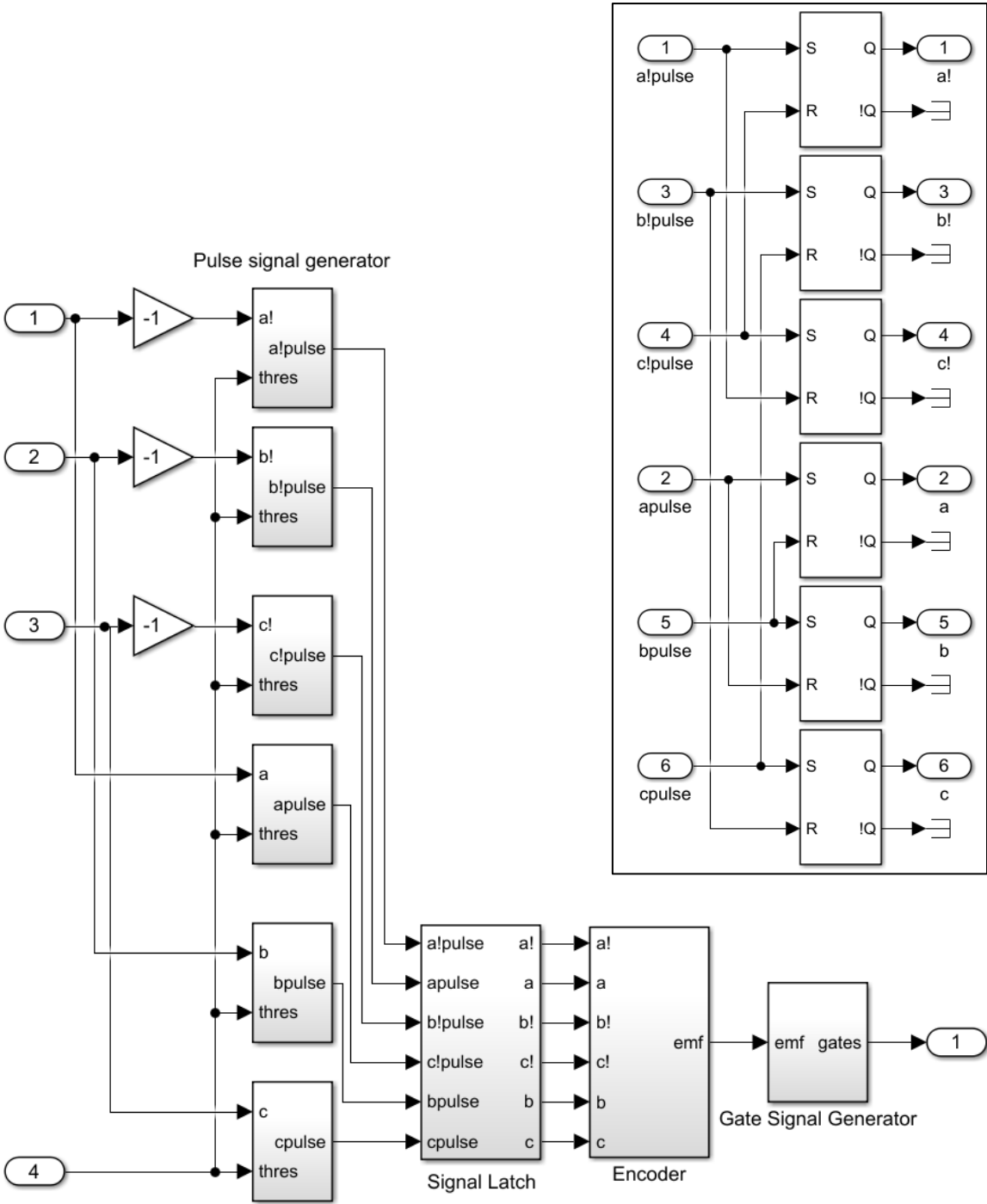


Figure 4.13 - Back EMF gate signal generator

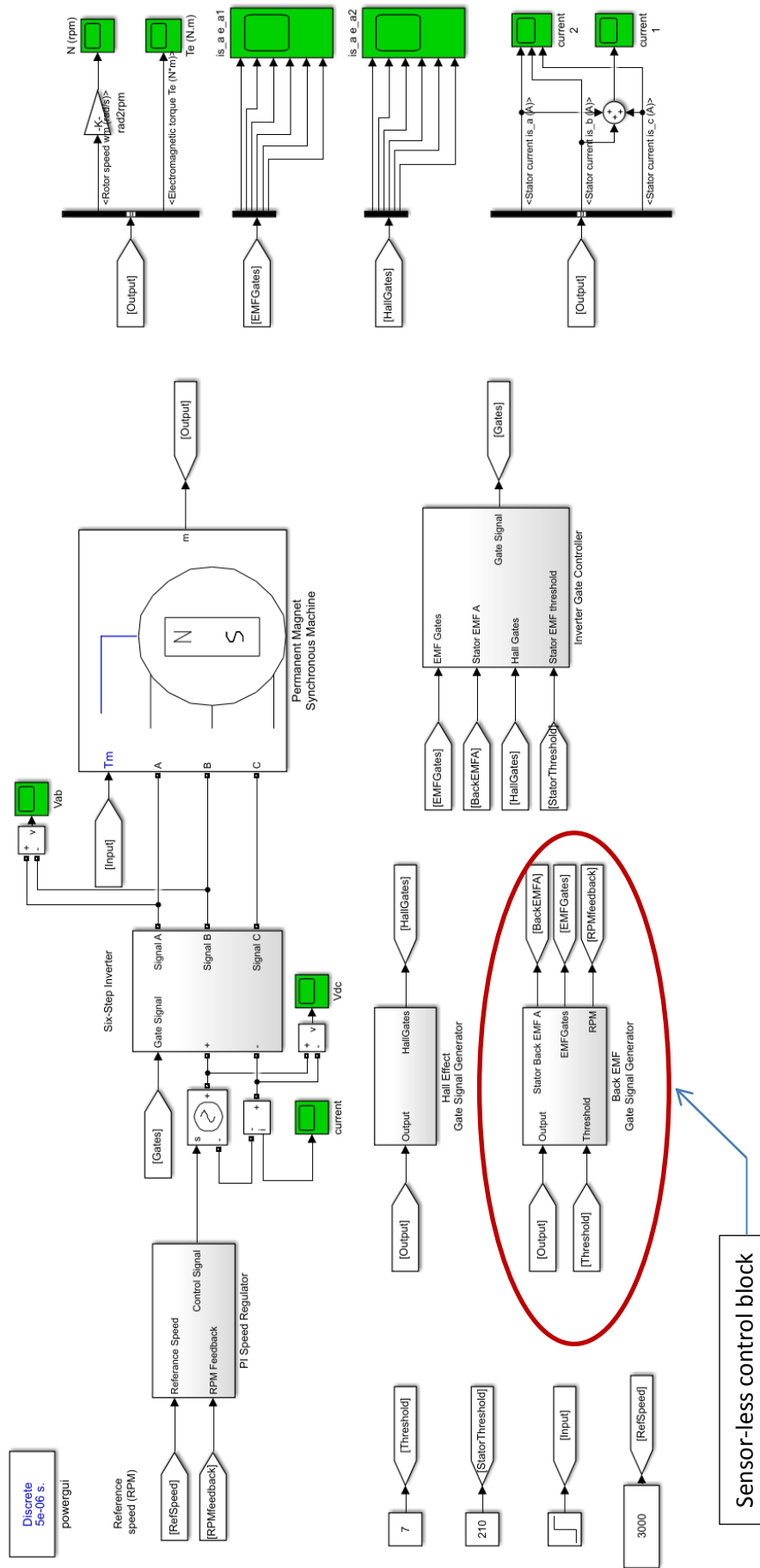


Figure 4.14 - Brushless DC Motor fed by 6 - step inverter and Senso-less control algorithm

### 4.3. Simulink model for Startup control

The Startup control is not strictly a speed control algorithm however is an extremely essential procedure that may need to be coupled with a fair number of other control strategies. As the name suggests this is an algorithm that plays a role for rotor speed increasing from rest condition. It is due to this reason that a general start up algorithm has been prepared which can then be coupled wherever there may be a need for its procedure.

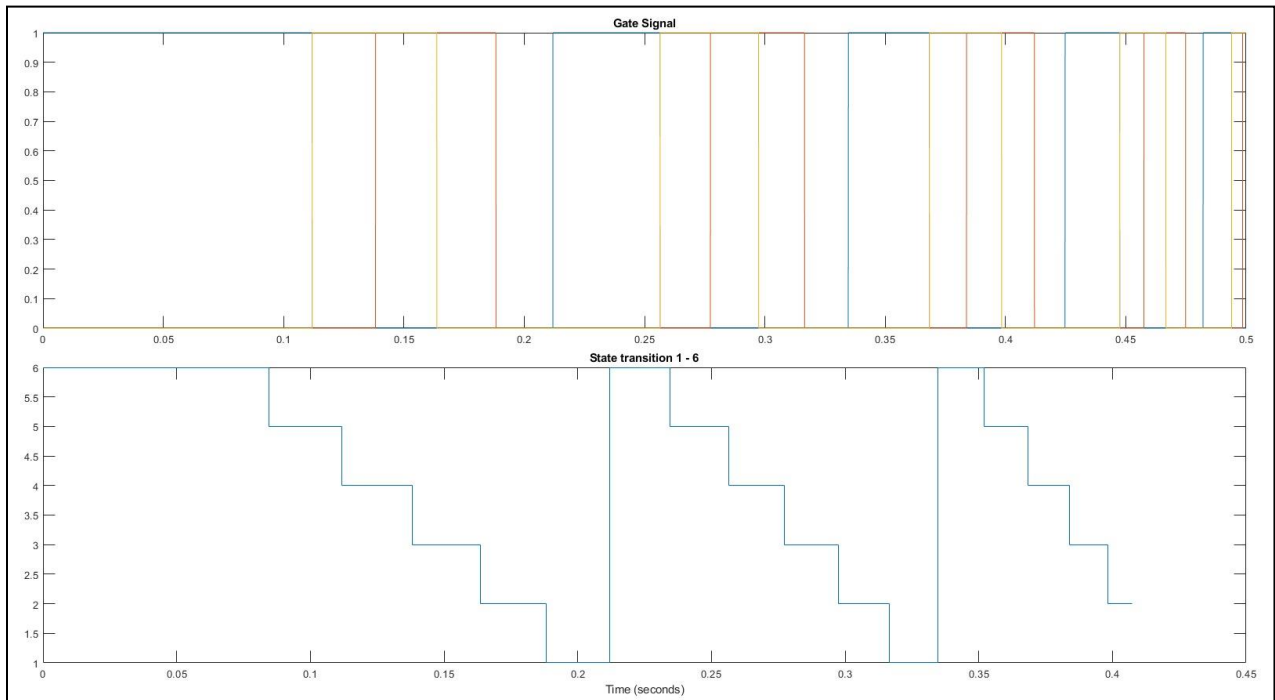


Figure 4.15 - Gate Signals

For the purpose of startup control, the first issue addressed is that of transitioning. There are two types of transitions that need to be addressed.

#### 4.3.1. Transition from Startup control to the standard control

In this case, a transition is needed from Start-up control to sensor-less method. This is due to the fact that Sensor-less control depends on the existence of a back signal. In order to generate such a signal, the motor needs to already be rotating in the EMF fields at a minimum critical speed. In the simulation that has been developed this check is provided in Figure 4.16 by checking the threshold back EMF and then selecting the control method in place.

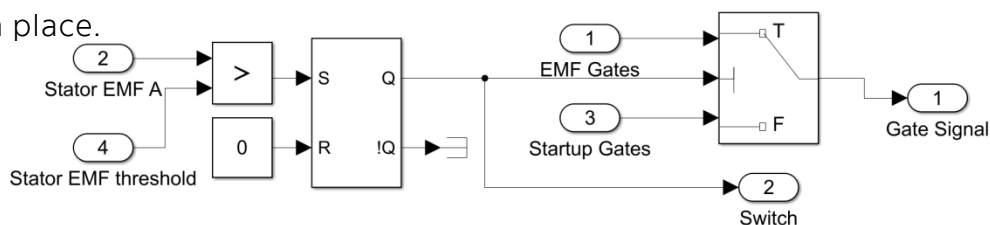
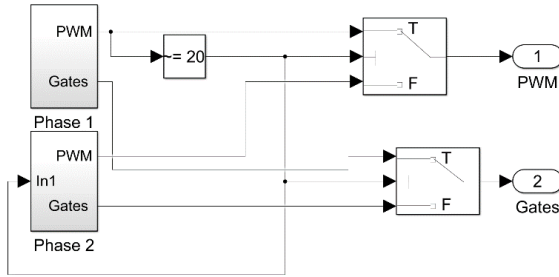


Figure 4.16 - Transition from Startup control to the standard control

### 4.3.2. Transition between stages of the start-up control



The stages of the start-up control are the methods of centering the rotor and then beginning the directional acceleration for beginning its motion. This transition is a pre-set time based transition in *Figure 4.17*.

*Figure 4.17 - Phase transition*

#### • Stage 1

In stage 1, the motor tries to bring the rotor at a fixed position from which it can begin commutation with predictable results. To achieve this, the control system provides a fixed gate signal as seen in *Figure 4.18*. This is achieved by an increment counter counting up to a certain calibrated value that depends upon the motor and counter pulse time. During this period, a fixed value is given to the gate signals with a ramping up PWM voltage allowing for the rotor to slowly align with the magnetic field with little to no oscillations about the steady state position.

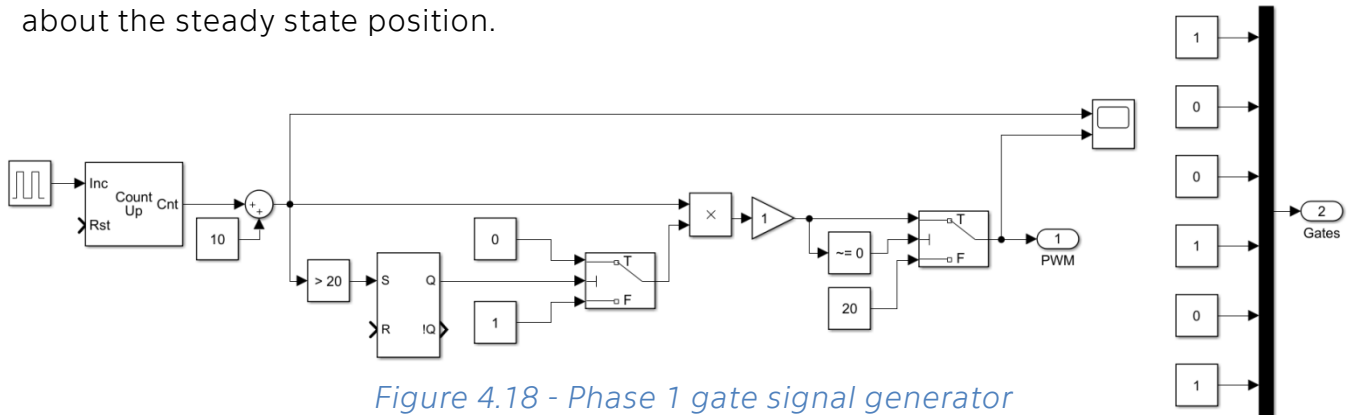


*Figure 4.18 - Phase 1 gate signal generator*

#### • Stage 2

During Stage 2, the motor begins to create the slowly accelerating rotating magnetic field that will cause the rotor to eventually reach critical rpm and back EMF in order to transition to a Sensor-less control. This is evident in *Figure 4.9* where both the transition into Stage 2 and also the reducing duration between the transition impulses can be seen.

This is achieved in *Figure 4.20* by the transition time being generated by a comparison between an arbitrarily calibrated integrator and a countdown timer with reducing threshold value. This then triggers transitions between the 6 commutation states of the 6-step inverter where the number in the state's subsystems represents the active gates.

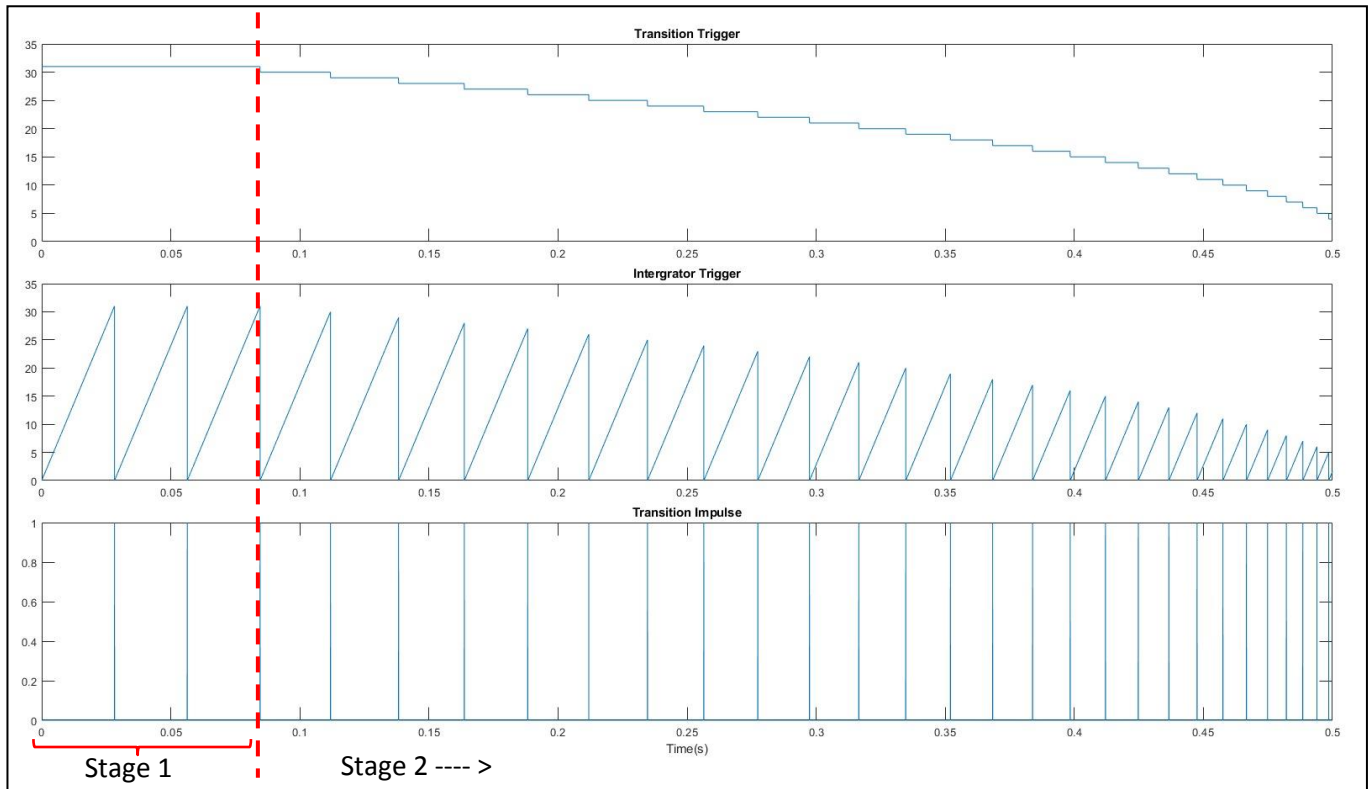


Figure 4.19 – Phase transition

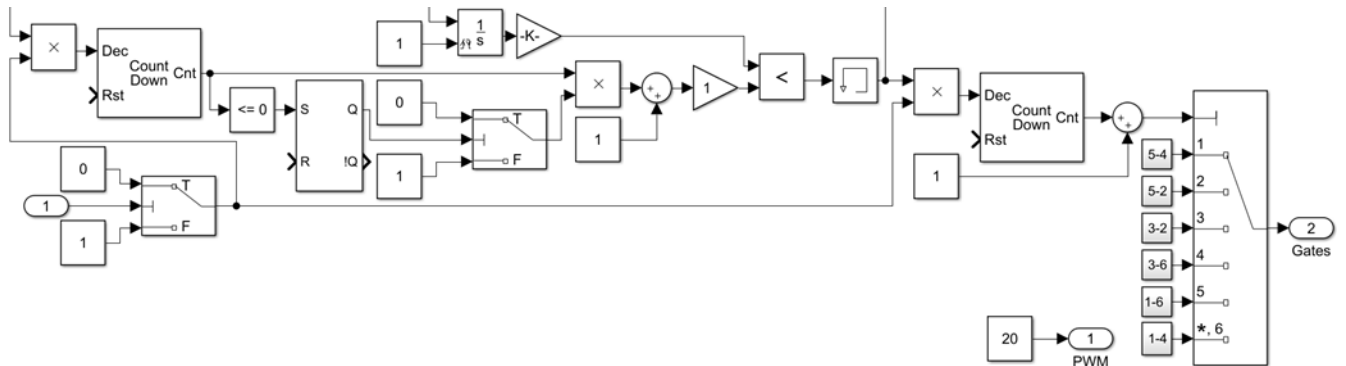


Figure 4.20 – Phase 2 Signal Generator

**Note** – This model also introduces the use of a PWM input for the capture of a PI control system. It allows for a fixed voltage input delivering a varying output voltage to the phases of the motor windings.

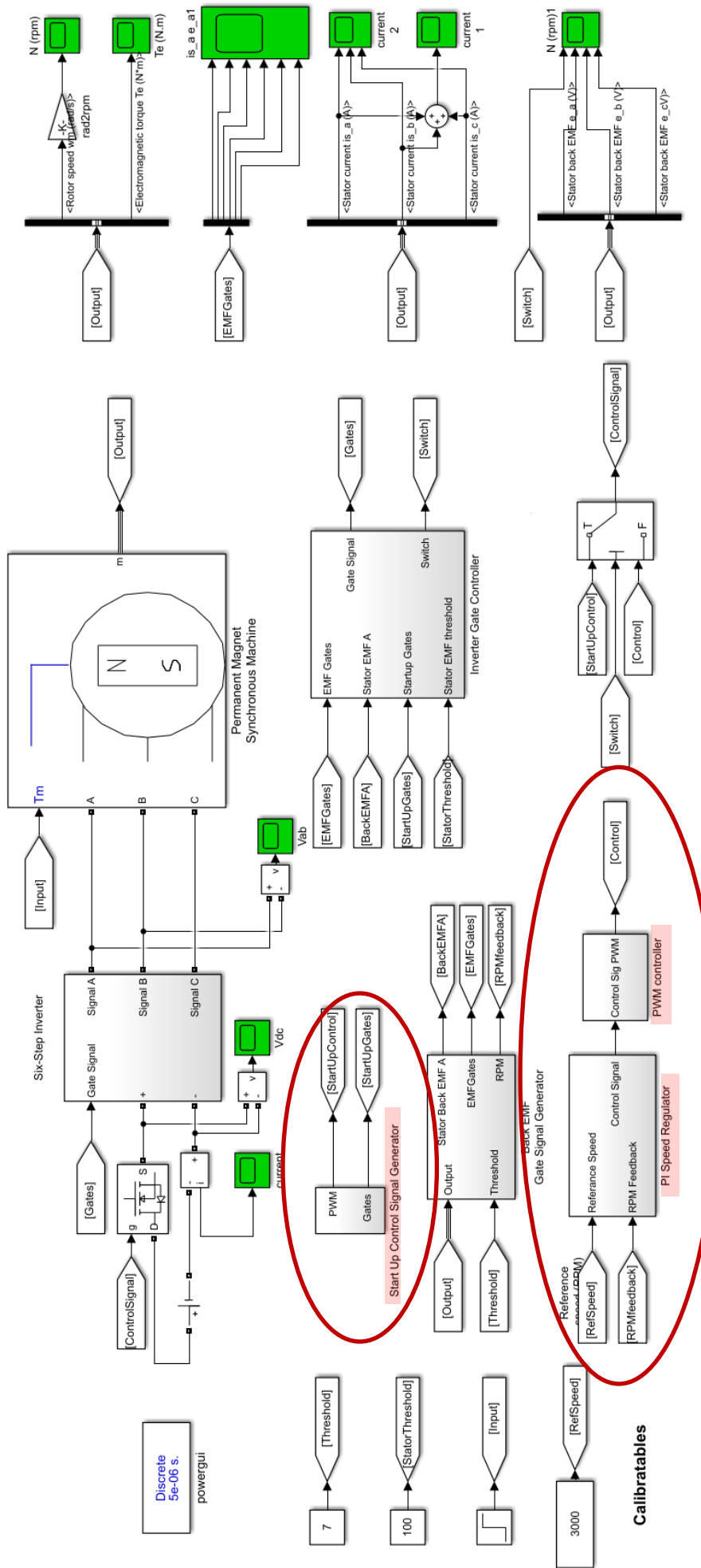


Figure 4.21 - Brushless DC Motor fed by 6 - step inverter and Start-up control algorithm



## 4.4. Simulink model for Sine wave PWM with third harmonic injection control

In this section, a simulation for the concept of Third harmonic injection a basic Sine wave modulation has been implemented. It also simultaneously implements the method of control with PWM to test the predictions of the benefits of Third harmonic injection.

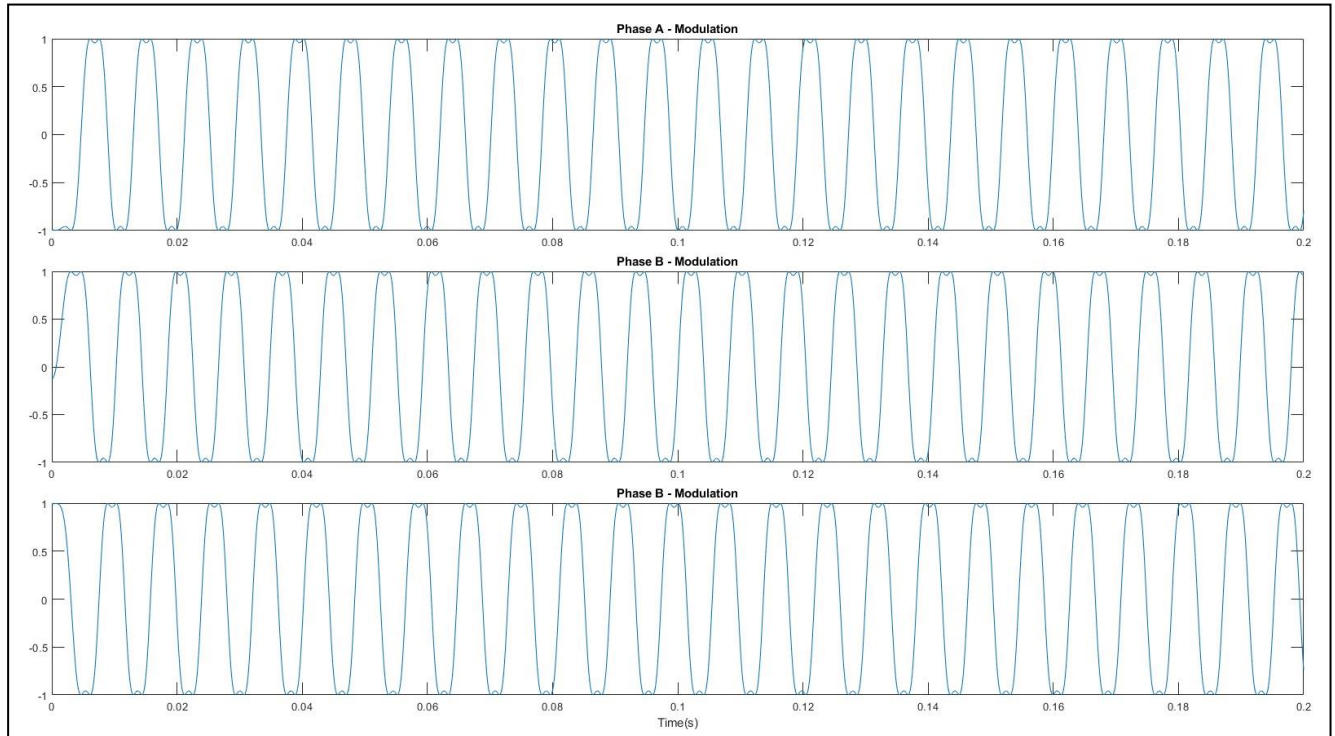


Figure 4.22 – Third harmonic Modulation in phases

As can be seen in *Figure 4.22*, the individual phase modulated signals are no longer a smooth sine wave but instead a combination of two waves. These waves can be identified by Fourier expansion to be the fundamental harmonic signal (phase to neutral voltages) and the third harmonic mode of the motor rotation speed.

The generation of this signal can be seen in *Figure 4.23*, where the generation of one phase signal has been highlighted for simplicity. A pair of sine waves is generated using the detected rotor angle such that the first has a frequency identical to the rotor and moves in synch, while the second has a frequency thrice the rotor. Each of these is then modulated and then combined.

The combined waves are now compared to a high frequency saw tooth signal to generate a Boolean signal which is used to control the gate signal for the inverter. This allows for a PWM- sine wave signal to be obtained at the motor phases.

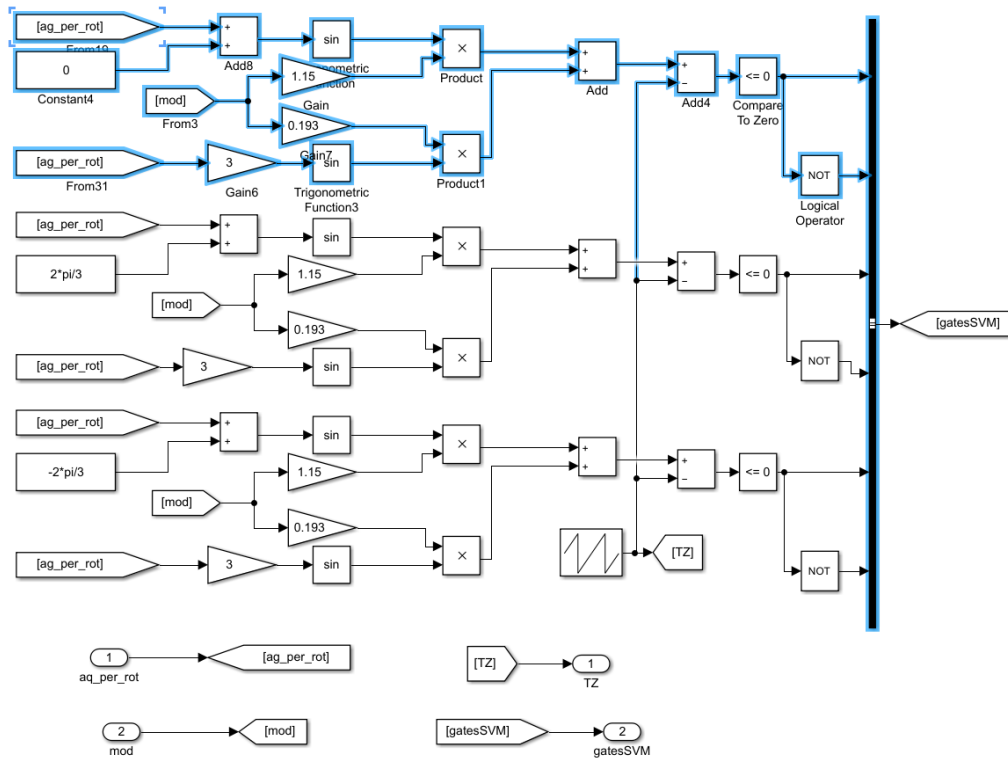


Figure 4.23 - Sine wave PWM with third harmonic injection control

The above Figure 4.24 depicts the measured phase voltages at the motor terminals. The proof of the third harmonic is presently hidden within the fact that the PWM received at the motor terminals is not smoothed out in simulation. This issue could be circumvented by introducing a custom made model for the motor. However, it was not possible to implement this as the exact specifications of the motor were not readily available at time of generation of simulation. Hence, this has been left to further research in case the need were to arise in the future.

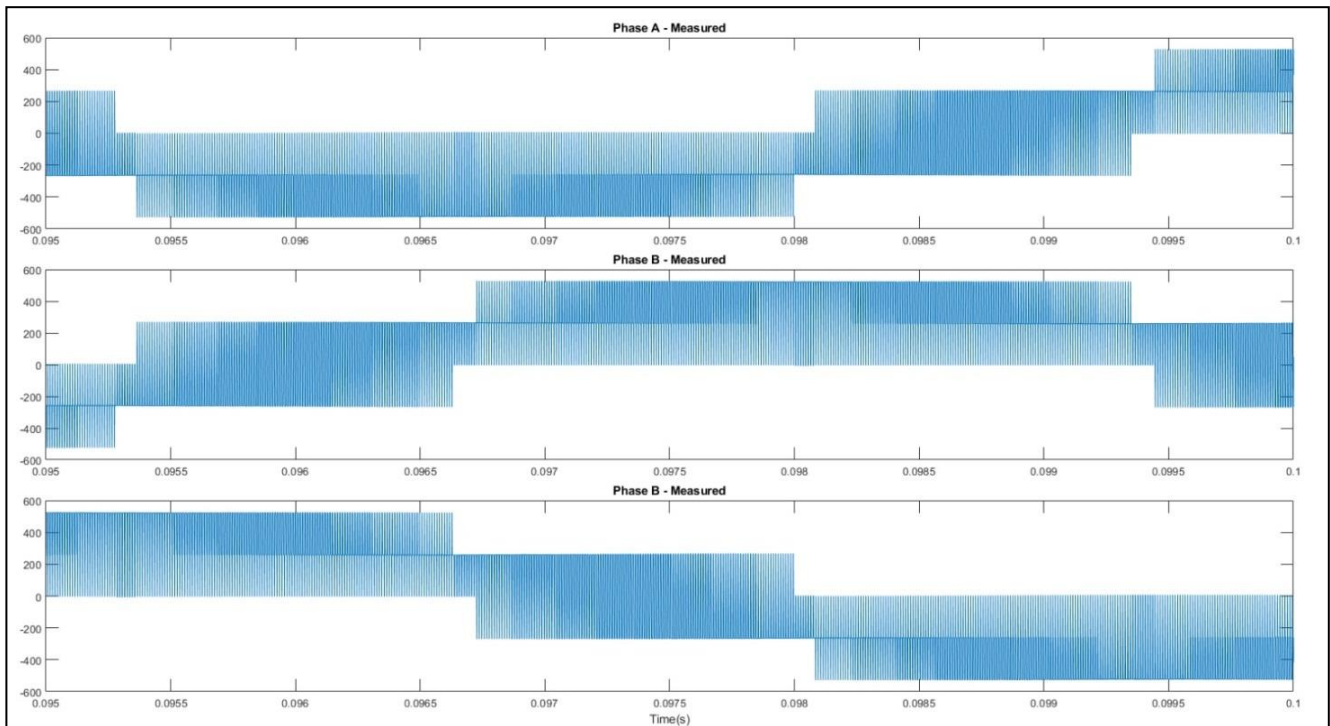


Figure 4.24 - Sine wave PWM with third harmonic injection

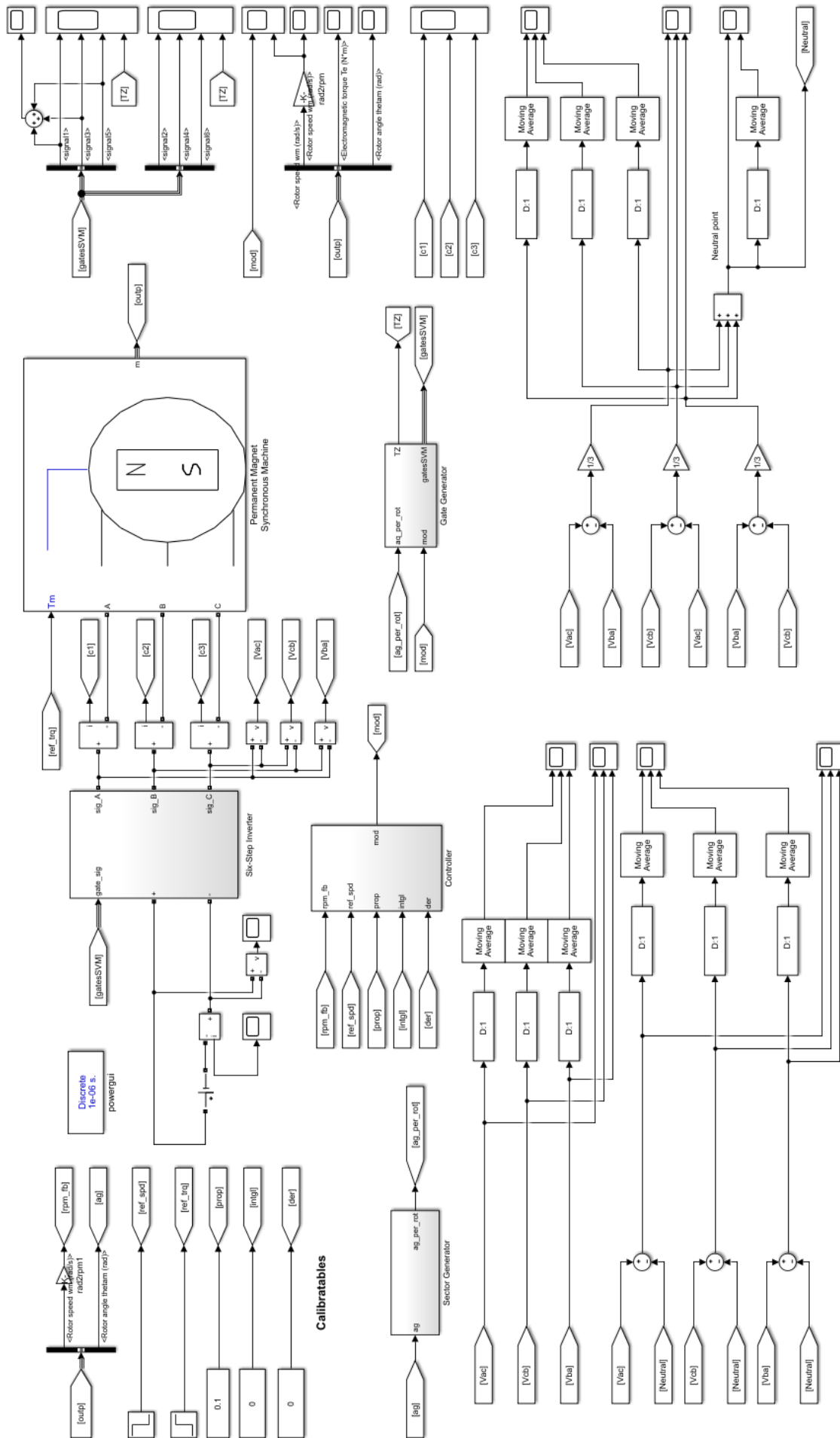


Figure 4.25 - BLDC Motor with SW-PWM and Third harmonic control

## 4.5. Simulink model for Space vector modulation with PWM control

The first step in the SV-PWM was to implement the logic where the two signals are generated. These two signals are the triangle wave for high frequency PWM control and a sector signal as seen in *Figure 4.26*. The sector signal is produced by comparing the rotor angle to a sector value and rounding it up to a ceiling thus defining the upcoming state transition in *Figure 4.26*. [22]

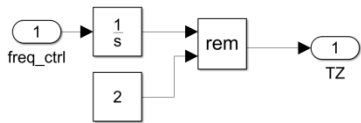


Figure 4.26 - Triangle wave generator

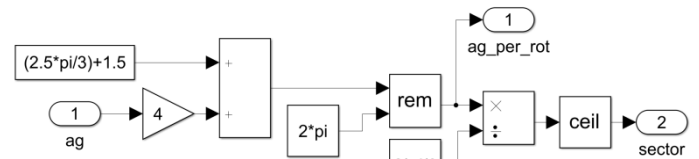


Figure 4.27 - Sector Generator

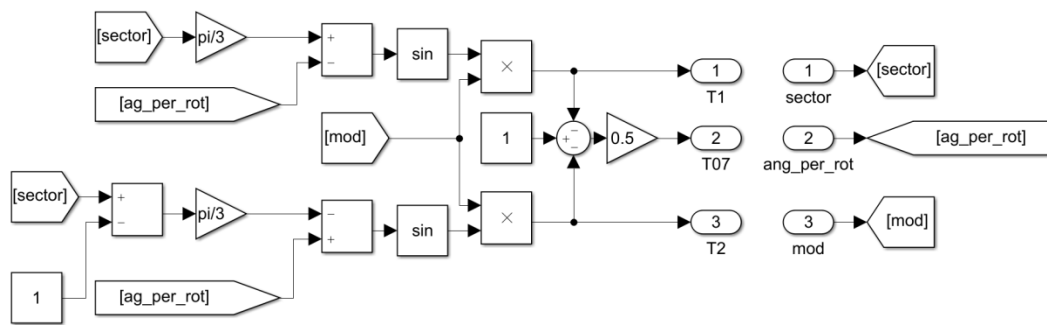


Figure 4.28 - Time ratio generator

The sector value is then combined with the actual rotor angle to define a ratio of the two space vectors in *Figure 4.28*. The pre-controlled modulation value is used to scale the degree of turn-on times for each of the space vectors. Subsequently, the remainder of the time is assigned to the zero vectors in equal half's respectively.

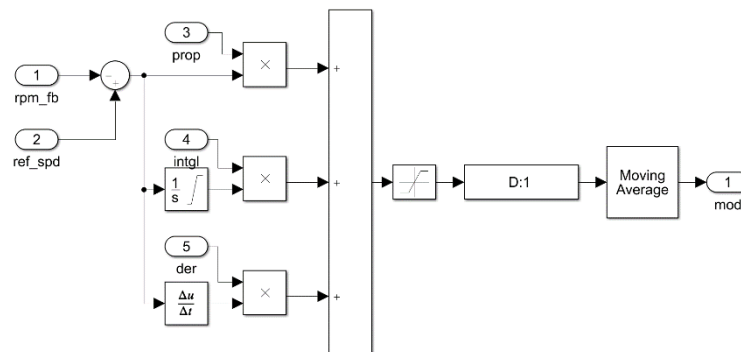


Figure 4.29 - PID controller

The modulation value is generated by passing the error of the actual rotor rpm versus the required rotor rpm and then using a calibrated PID controller in *Figure 4.29*.

At the next stage, the simulation compares the triangle value with the summed-up times of transition in successive stages to generate a vector value that represents a vector that should be turned on at that instant of time. The overall logic can be seen in *Figure 4.30* and also the final stage of comparison can be seen in *Figure 4.31*. In case the time instant lies where the sum adds up to be lesser than complete cycle but higher than the transition time for final zero vector then this section will result as true.

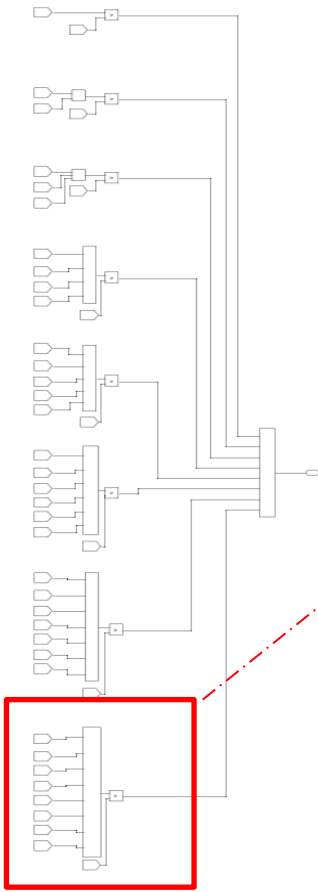


Figure 4.30 - Vector Generator

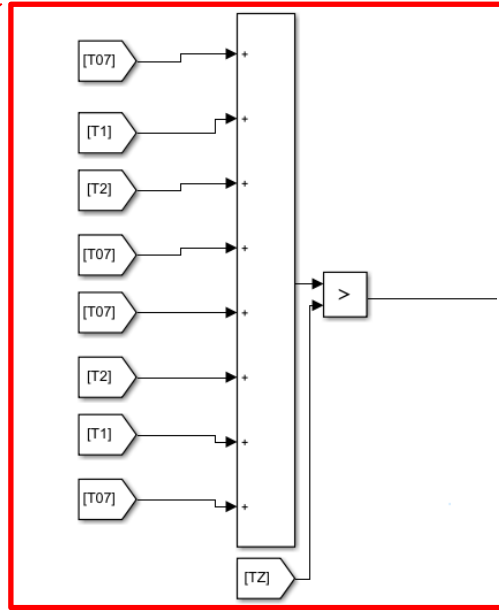


Figure 4.31 - Final Stage

The sector value is used for generating the two vector values in *Figure 4.32*. The generated vector values are then used for cycling through the different vectors valid for the sector in *Figure 4.32* at a speed set by the transitioning previously calculated.

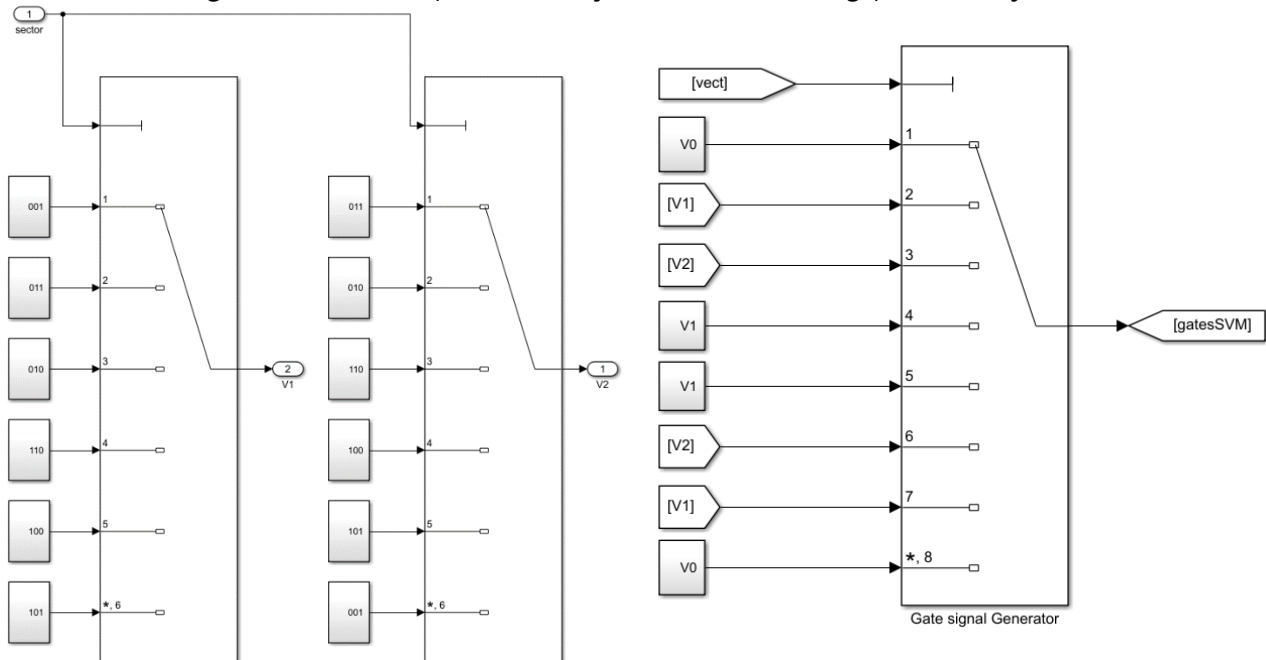
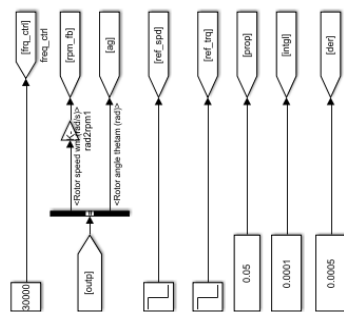
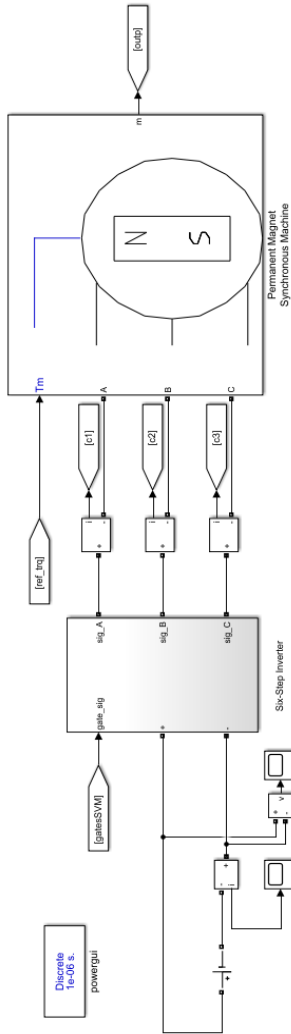
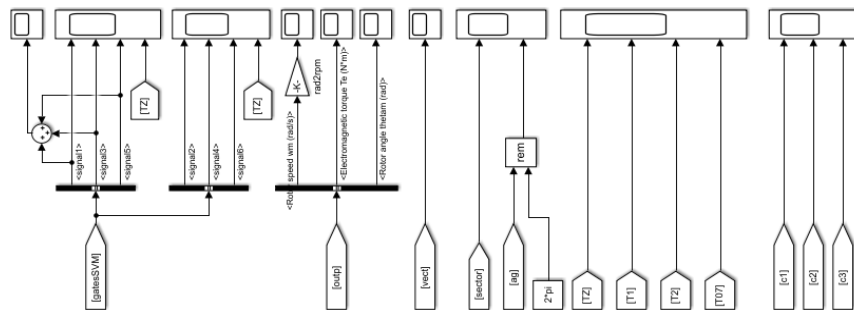


Figure 4.32 - Gate signal Generator



**Calibratables**

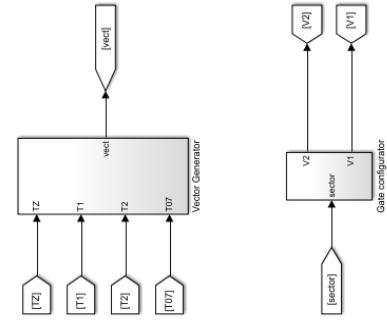
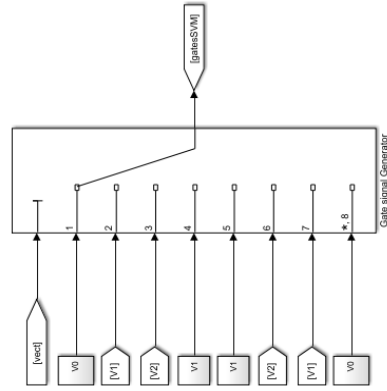
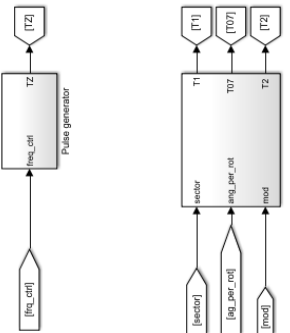


Figure 4.33 - BLDC Motor with SV-PWM controller

## 4.6. Future Prospects

### 4.6.1. Optimization of Power supply

- **Purpose**

In all the previous models generated and the control algorithms approached, one underlying assumption was that the motor has been supplied power by an ideal DC power source. This however is not a viable assumption in practice.

The general assumption made includes -

The source is powerful enough that it shall be able to maintain the required voltage level at its terminals irrespective of the output current provided.

In a real system this is seldom the case. Real batteries and sources have a diminishing value of voltage versus the current. There are other aspects like battery charge and temperature effects which affect the generated voltage.

The effect encountered by various torque ripples and also the harmonics in the system lead to a substantial variation in the required voltage and subsequently a large battery pack considering safety standards.

For the project undertaken, one of the main optimizations proposed is the improvement of the battery power management system. The goal is to most efficiently distribute the battery power to the motor being driven. This includes –

- Reduction in noisy current required at the battery pack terminals  
The various load variation, harmonics and especially the PWM modulation leads to a very noisy current at the battery pack.
- Reduce overall battery current and voltage rating
- Reduce overall weight
- Reduce recharging time

## • Proposed new improvements to power management system

The main idea of the below proposed method has been developed in co-operation with Ricardo plc. for the improvement in power supply with reasons as previously discussed. The idea is to include a filtration system to the battery supply that will be able to reduce the noisy requirements of the system and make the battery functioning relatively stable.

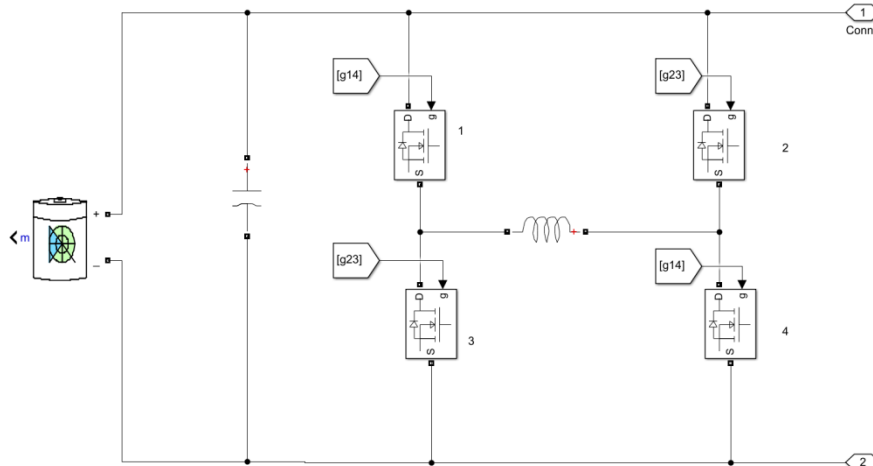


Figure 4.34 – Schematic of power management system

In order to prepare this simulation, the first change that was needed to be implemented was to begin using a realistic battery model offered by MATLAB Simulink/SimScape.

In the Figure 4.35, the capacitor acts as the primary passive filter. This removes major variations in the load experienced by the battery. The secondary active part of the filtration system is an Inductance that is controlled by an inverter. The gates of the inverter are controlled in such a manner that the battery charges the inductance when the required current is less than the average current demand and the inductance then supports the battery in supplying power by coupling itself with the battery supply when the current demand is higher than the average.

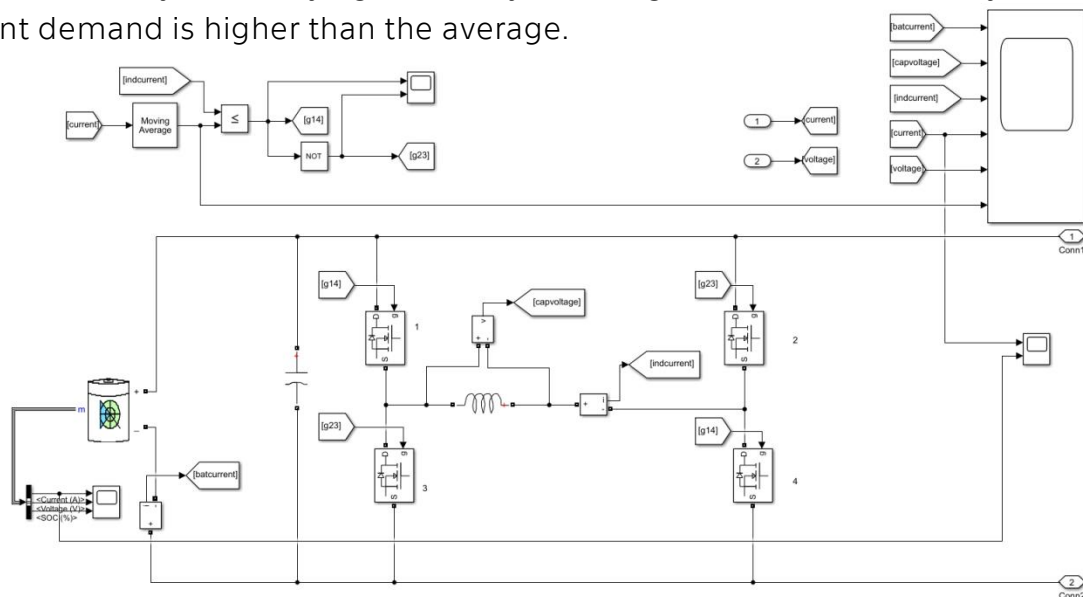
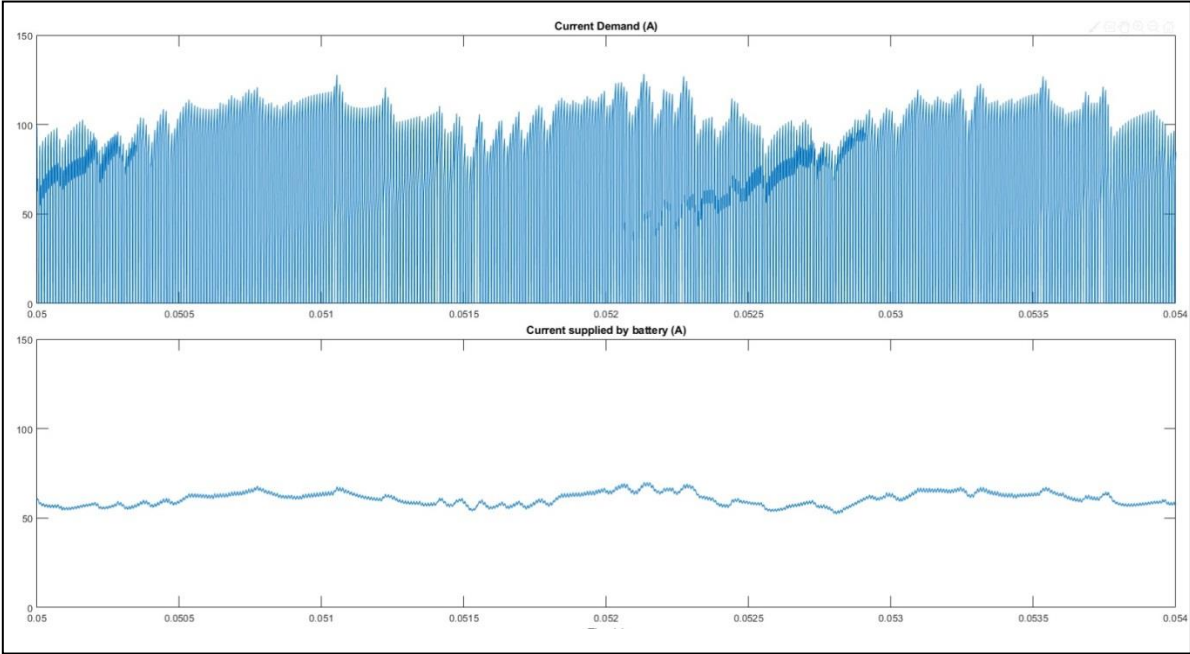


Figure 4.35 - Final model of proposed power management system



The below *Figure 4.36* shows a graph of the resultant current supplied by the new battery pack versus the current demand experienced by the previous battery. There can be seen a substantial smoothing out of noisy PWM induced variations by the filtration system.



*Figure 4.36 - Difference in current load at start-up*

The below *Figure 4.37* now shows the effect of the new battery pack on the currents discussed above when the motor works either directly under 6-step control algorithm or when the SVM-PWM control algorithm has achieved a full overloaded modulation causing it to shift into 6-step control. Even in this extreme case where PWM is relatively at the maximum limit, a substantial smoothing can be observed.

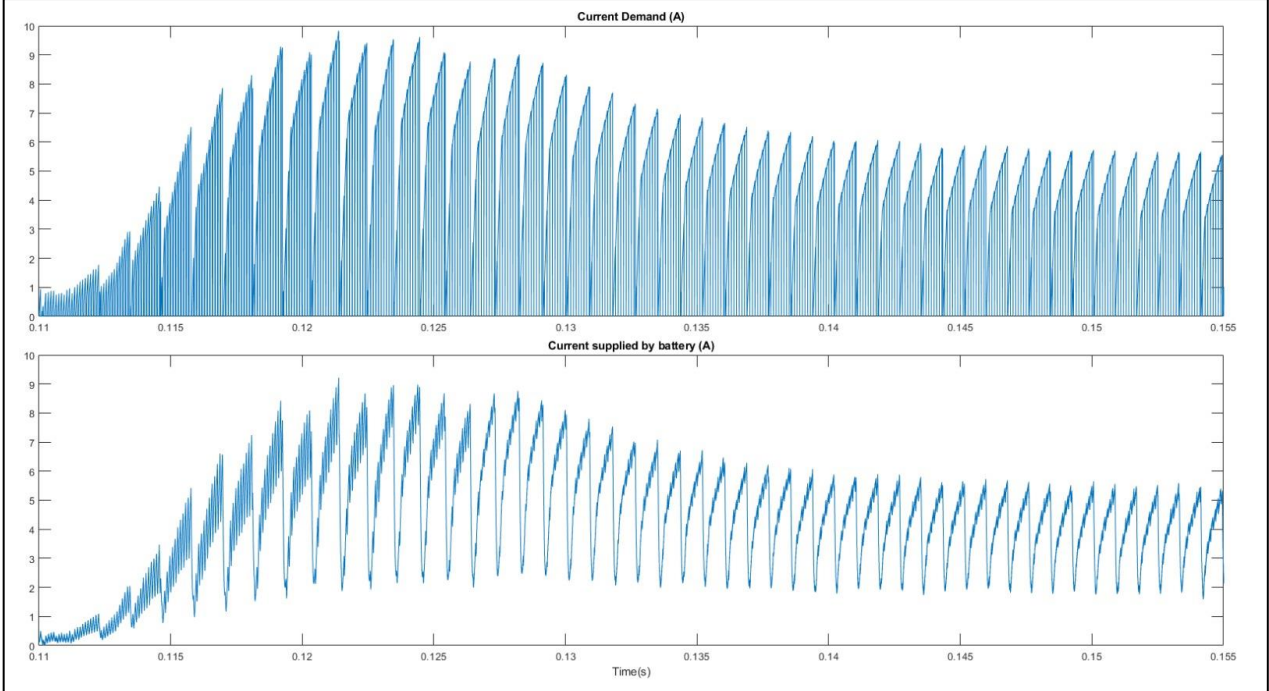


*Figure 4.37 - Difference in current load at 6- step control*

- **Advantage**

The reduction in peak currents places a lesser demand on the battery and hence can lead to downsizing of the battery size itself.

It could also possibly reduce the cost of the system as the new hardware introduced generally is substantially more cost effective than the larger battery.

Also, since the present thesis is in relation to Electric vehicles a lowering of the battery pack weight incurs benefits in overall vehicle efficiency.

Another major benefit of the smoothing of the noisy current is that this leads to much lesser heating up of the battery and hence lesser temperature effects and improved lifespan of the battery pack.

## 5. Practical Realization

The following section is a practical study for the verification of the control strategies previously presented. A working model of the system has been developed by setting up a makeshift test bench using components provide for the purpose of this research by the Faculty of mechanical engineering, ČVUT, Prague.

The strategy chosen to be implemented is that of SV-PWM. The main purposes for this choice as opposed to its counterparts include –

- As this Thesis is a study of control strategies for the implementation in the automobile industry SV-PWM proves to provide many of the needed properties of the motor operation
  - Smooth Start-up characteristics
  - Lower induced noise
  - Improvement over the present popular strategies like 6-step control
  - Max torque extracted from the motor (possibility to over modulate)
- SV-PWM is computationally and logically the most complex of the discussed control strategies
- The SV-PWM method at over-modulation condition (greater than 1.25) begins to exhibit regular 6-step inverter control
- Other strategies have been substantially tried tested and implemented in a variety of studies of BLDC motors

# 5.1. Hardware Setup

Below is the basic description of the hardware components used in this research. For further details please refer to the Appendix A.

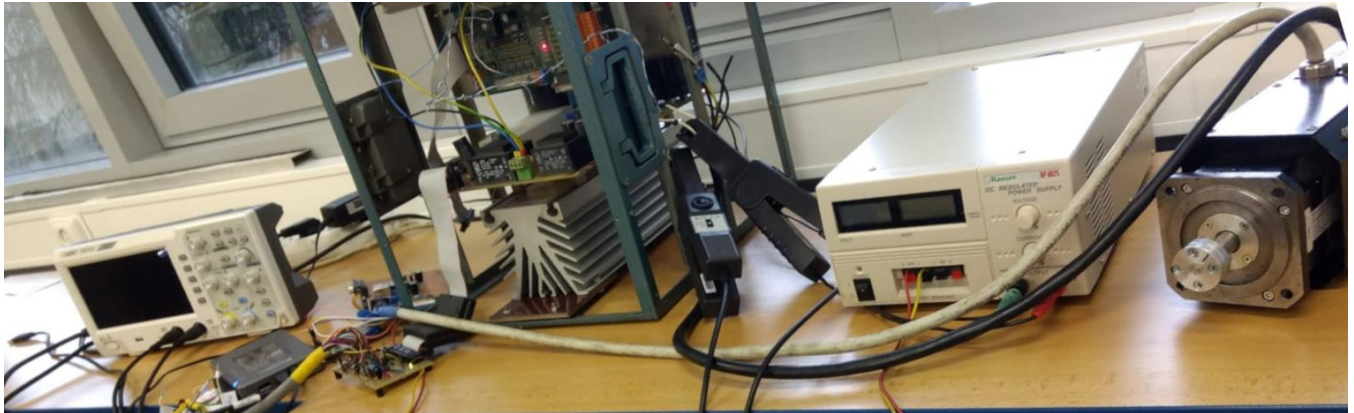


Figure 5.1 – Test bench

In the below block diagram (see Figure 5.2), the various connections that exist between the hardware components can be seen to form an approximate understanding of how power and digital logic flows in the setup.

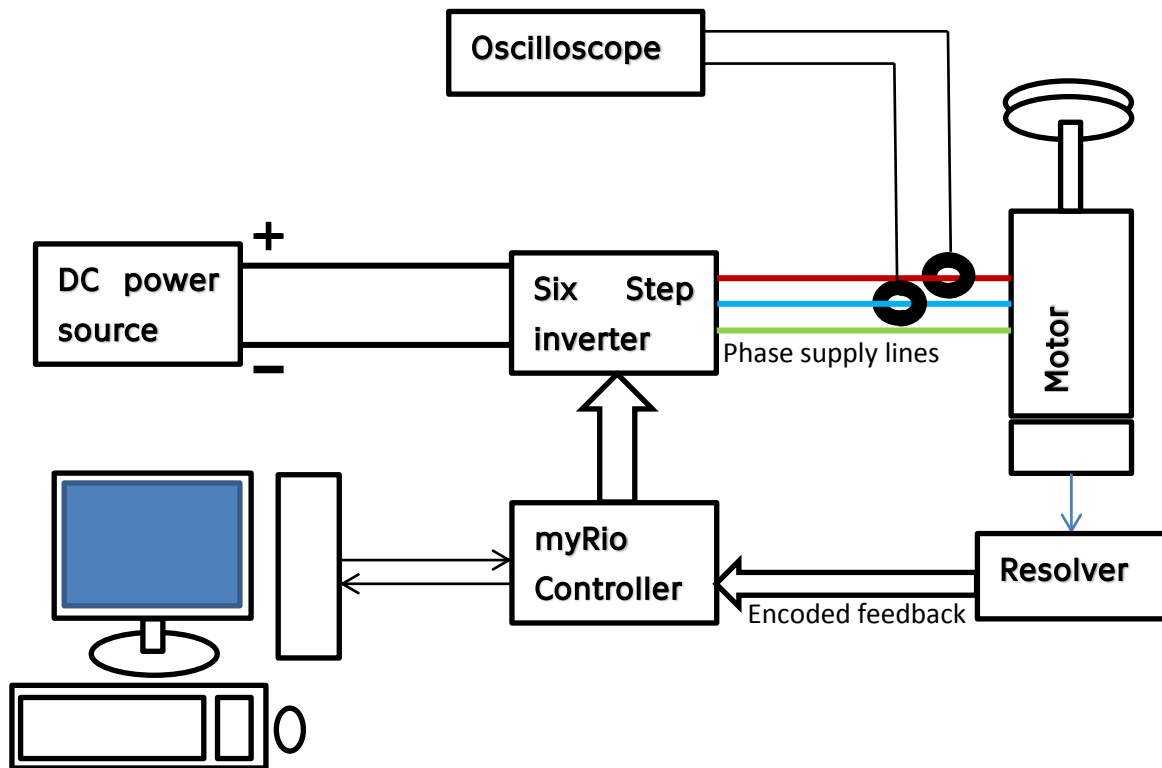


Figure 5.2 – Block Diagram of components

### 5.1.1. PMSM Motor

The motor used in this thesis research is the 2AML406B-S <sup>[23]</sup> series of PMSM motor produced by VUES Brno s.r.o., Brno (see). The motor variant is of a two pole motor construction and allows for an operation in the speed range from 25,000 to 40,000 min<sup>-1</sup> with a maximum power of 3.4 kW.

As mentioned in the original thesis guidelines, the motor used for verification of the control algorithm here is a PMSM motor. This is due to the fact that the overall functionality of a BLDC motor and PMSM motor is very similar especially at the conditions of testing.

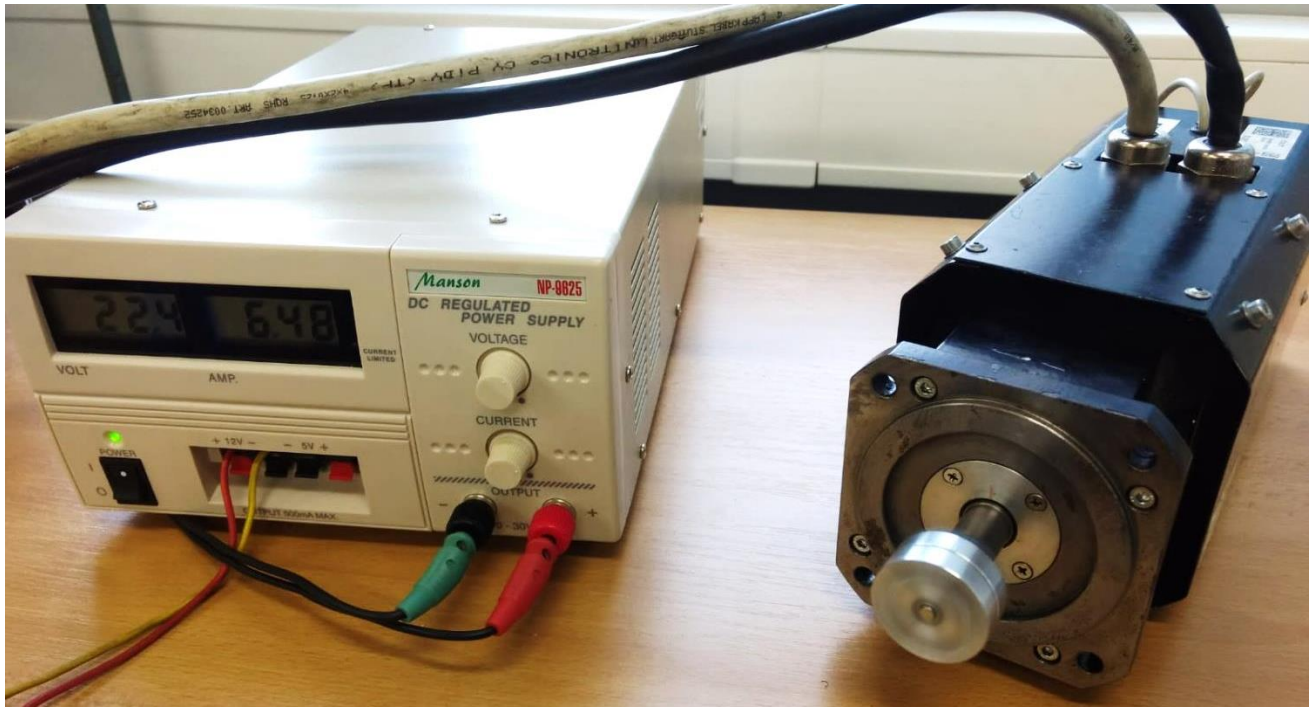


Figure 5.3 – DC source and PMSM Motor

### 5.1.2. DC Power Source

For the purpose of proof of concept the motor was driven at a relatively low power for safety reasons. The source chosen was the Manson NP-9625.

### 5.1.3. Six step Inverter

The main components used in providing the custom based inverter action and their functions have been described below. For further specification of these components please refer Appendix A.

- **Six-pack IGBT Driver**

The driver core offered by SEMIKRON forms the main component for the interfacing between the Digital controller and the physical motor. It receives the digital signals from the myRio board used as a controller in the case of this research and provides powering to the subsequent power electronic circuit.

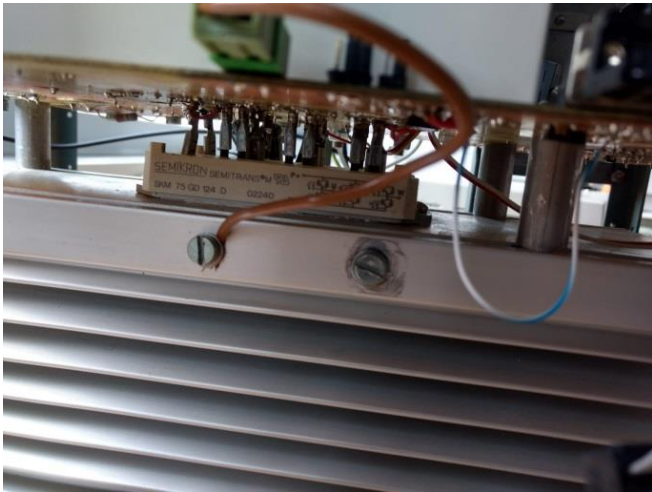


Figure 5.5 – IGBT Module

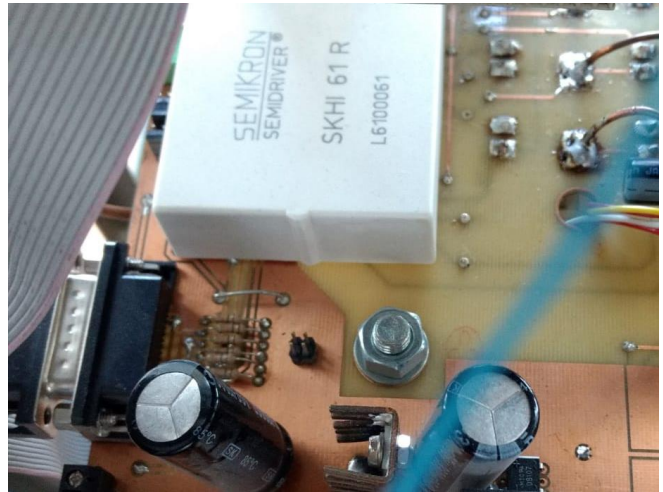


Figure 5.4 – Six-pack Driver

- **IGBT module**

The SEMIKRON IGBT (Insulated-Gate Bipolar Transistor) module SKM 75 GD 124 offering upto 75A in voltage class 1200V has been used for the power electronic inverter bridge for the PMSM motor supply. It is of a six-pack topology and provides higher power densities especially in motor drive. [24]

- **AC/DC transformer**

The HAHN BV EI 481 1184 offers an AC/DC transformer maximum safety and durability device with excellent resistance to temperature changes, high overvoltage resistance, self-extinguishing cover. [25]



Figure 5.7 – Current Sensors

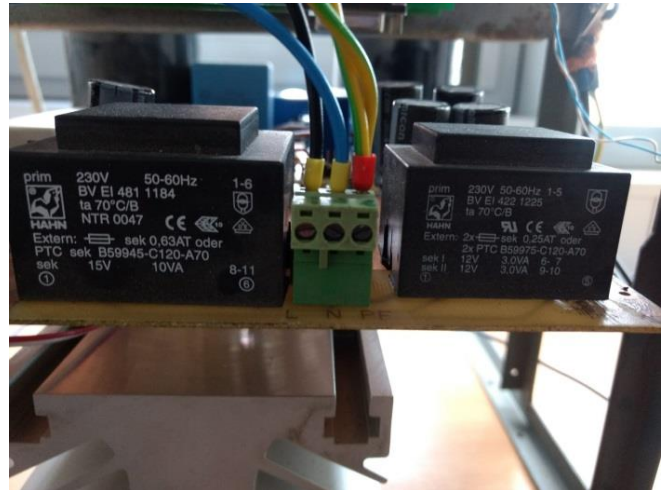


Figure 5.6 – AC/DC transformers



Figure 5.8 – Cooling Fin for Heat dissipation

- **Current sensor**

The sensor used for this board is the LEM LA-55-P current sensor. It proves ideal for the measurement of currents: DC, AC, PWM with a galvanic separation between the primary circuit and the secondary counterpart. [26]

## 5.1.4. MyRIO Student Embedded Device



Figure 5.9 - MyRio Student Embedded Device

The myRIO Student Embedded Device in Figure 5.9 has been used in this thesis for the purpose of a digital controller that takes the inputs received from the motor and driver system such as encoded rotor angle, phase currents and then pass it through the generated algorithmic process and generate a control signal that coupled with the gate driver allows for a holistic control system for the BLDC motor.

One of the main factors that made this driver a lucrative selection includes the fact that it provides reconfigurable I/O that allows implementation of multiple design concepts with one device. This allowed the rapid prototyping and design modifications in the control strategy with minimal time delay and ease of access. [27]

The myRIO Student Embedded platform features I/O on both sides of the device (MXP and MSP connectors). It includes digital I/O lines, analog inputs, analog outputs, a push button, LEDs, an onboard accelerometer, a dual-core ARM Cortex-A9 processor and a Xilinx FPGA. Some models also include WiFi support. The myRIO Student Embedded Device can be programmed with LabVIEW or C. [28]

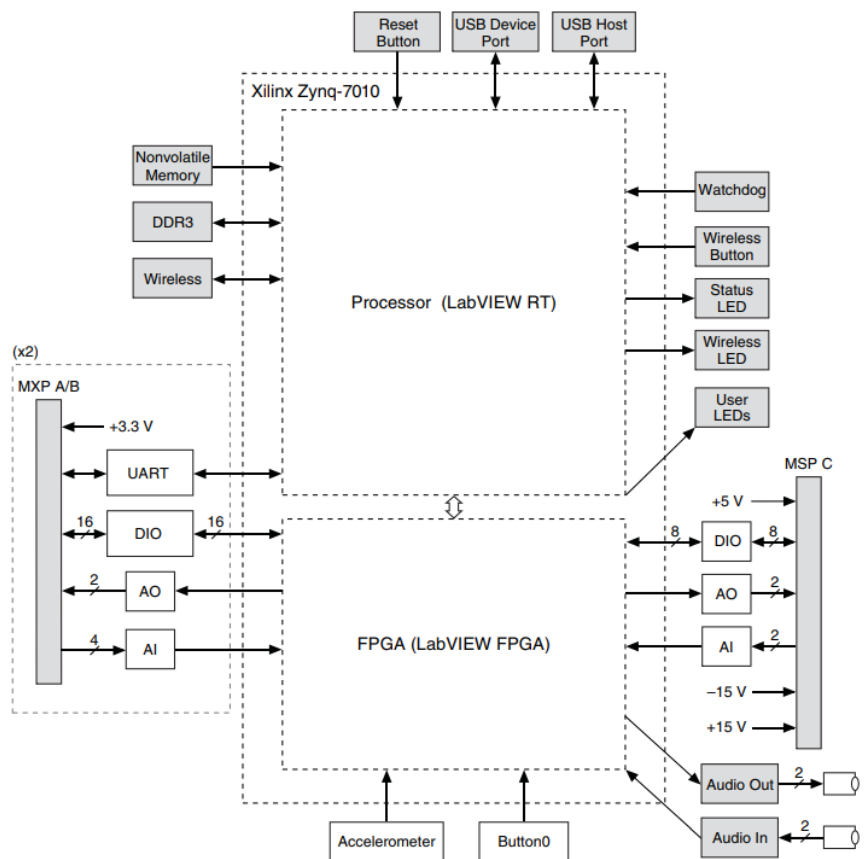


Figure 5.10 - Block Diagram



## 5.1.5. Angular position Resolver

The angular position resolver is an electromechanical device that employs the principle of induction in a rotary transformer to generate signals. These signals are then pre-processed before being supplied to the controller. The resolver accepts waveforms and then passes them through a comparator to produce an incremental encoded signal.

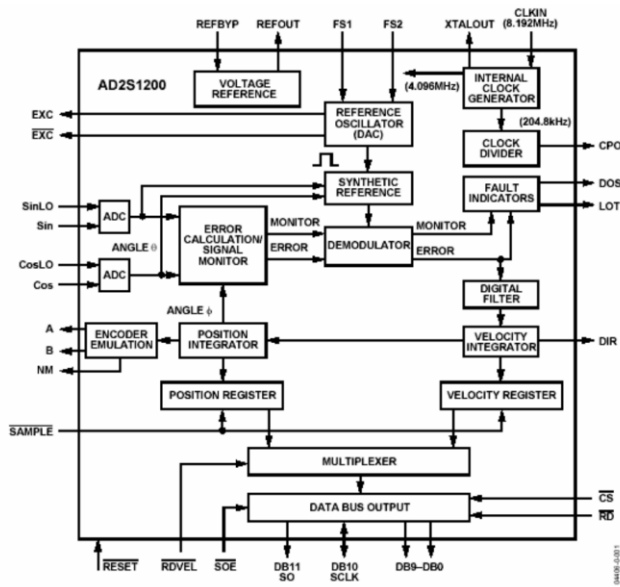


Figure 5.12 – Resolver Schematic<sup>[29]</sup>

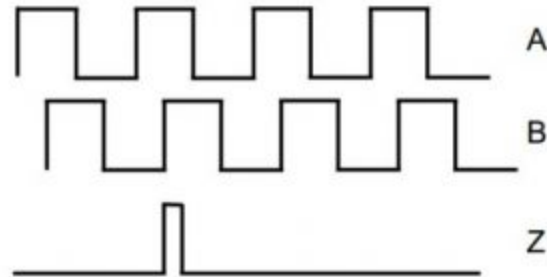


Figure 5.11 – A, B, Z Signal lines

The principle of the encoded signal in *Figure 5.11* is that the lines A and B have a square waveform with respect to rotor angle but are phase shifted by 90°. This allows for the resolving of the rotor rotation in steps that amount to a total of 4098 steps in a rotation. The Z line is the reset line that provides an impulse once in a complete rotation every time a particular position is reached. The combination of these signals allows for generating an absolute position of the rotor angle.<sup>[29]</sup>

## 5.2. Labview algorithm

The MyRIO Student Embedded Device offered by National Instruments comes compatible with the LabView Software for program generation. For this purpose, the Software has an additional module that needs to be included called the FPGA module.

LabVIEW offers a graphical programming approach that helps in the visualization of every aspect of the generated application, including hardware configuration, measurement data, and debugging. This makes it simple to visualize the integration of measurement hardware, represent complex logic on the diagram, develop data analysis algorithms, and design custom engineering user interfaces.<sup>[30, 31, 32, 33, 34]</sup>

LabVIEW FPGA module helps for the efficient and effective design of complex systems by providing a highly integrated development environment, IP libraries, a high-fidelity simulator, and debugging features. A field-programmable gate arrays (FPGAs) are integrated circuits (IC) that can be programmed in the field after manufacture. FPGAs provided by the Xilinx MyRio Controller are similar in principle to programmable read-only memory (PROM) chips. However, they come with a vastly wider potential application PROM Chips. Embedded FPGA VIs can then be created that combine direct access to I/O with user-defined LabVIEW logic to hardware-in-the-loop simulation and rapid control prototyping.<sup>[35, 36]</sup>

In consideration of the above distribution of logic between the two modules, the control program in LabView was split in two main components during development

- LabView FPGA VI Component
- LabView VI Component

### 5.2.1. LabView FPGA VI Component

The LabView FPGA VI front panel in *Figure 5.13* forms the main Interface for dealing with the control and calibration of the FPGA VI during execution.

This approach of leaving most of the variables in the control logic as runtime calibratable variables leads to a substantial saving in time for control algorithm generation. The generation and implementation of a LabView source code for a VI to be written onto a MyRio board is relatively long on a local server and hence the ability to have to flexibility of fine tuning the algorithm during runtime proves to be a large benefit.

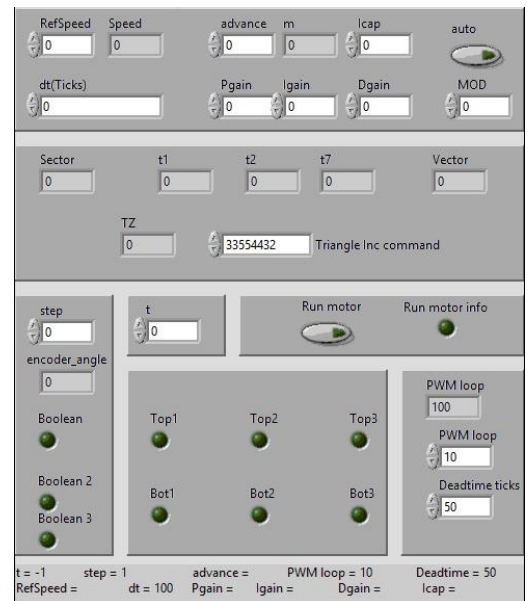


Figure 5.13 - FPGA VI front Panel

These variables are also then connected to the higher-level software generated in the Labview VI and allow for a comprehensive tuning of especially the feedback PID control part of the algorithm.

• **PID Controller loop**

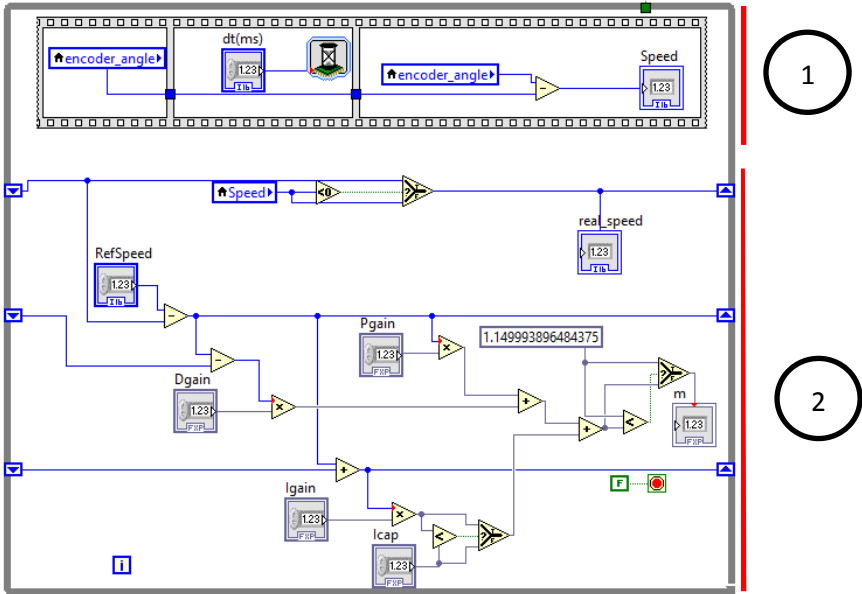


Figure 5.14 - PID Controller loop

The PID feedback controller in Figure 5.14 works in 2 stages in order to produce a modulation value for the control of the motor.

In stage one the loop has a flat sequence block that calculates the speed of the rotor by using the angle value previously generated.

The second stage compares this speed to the target reference speed to generate an error signal. The error signal is first scaled directly by a gain in P part of the controller. The D part calculates the change in error from the previous loop and then scales it. In the I part the error is added to the previous summation and then the result is scaled.

While these are not the exact derivative and integrative calculations they are simplified approximation considering a discrete calculation and loop time as unit time. This simplification allows for a much-simplified controller logic and quicker cycle times

• **Angle and time generator loop**

The angle value is generated in the below Figure 5.15. The signal is received by the MyRio board at the connector pins. These take a Boolean value that has been encoded previously in the method as discussed in section 2.6.1. The signals received from pin 0 -3 are the signals for line 1, line 2 reset and direction of turning respectively.

The first stage of the below while loop is to verify that there has been some change in the received values.

In stage two, there is a check if the rotor is moving in clockwise or anti-clockwise manner and subsequently the step shall be a positive or negative value for the angle.

In stage 3, the angle value is incremented by the step in case an edge change has been detected in the line 1 or line 2 values. Upon one complete rotation i.e. 4095 steps the value is reset to zero. A secondary override is also received on the reset line that changes the stored angle value to zero.

The next stage four is where the angle value is then compared to preset segregation values that allow for the prediction of the rotor vector's present sector orientation.

The final stage five of the loop, is where the angle value and predetermined modulation value is used to generate the turn on and turn off times for the individual space vectors at that cycle of the controller.

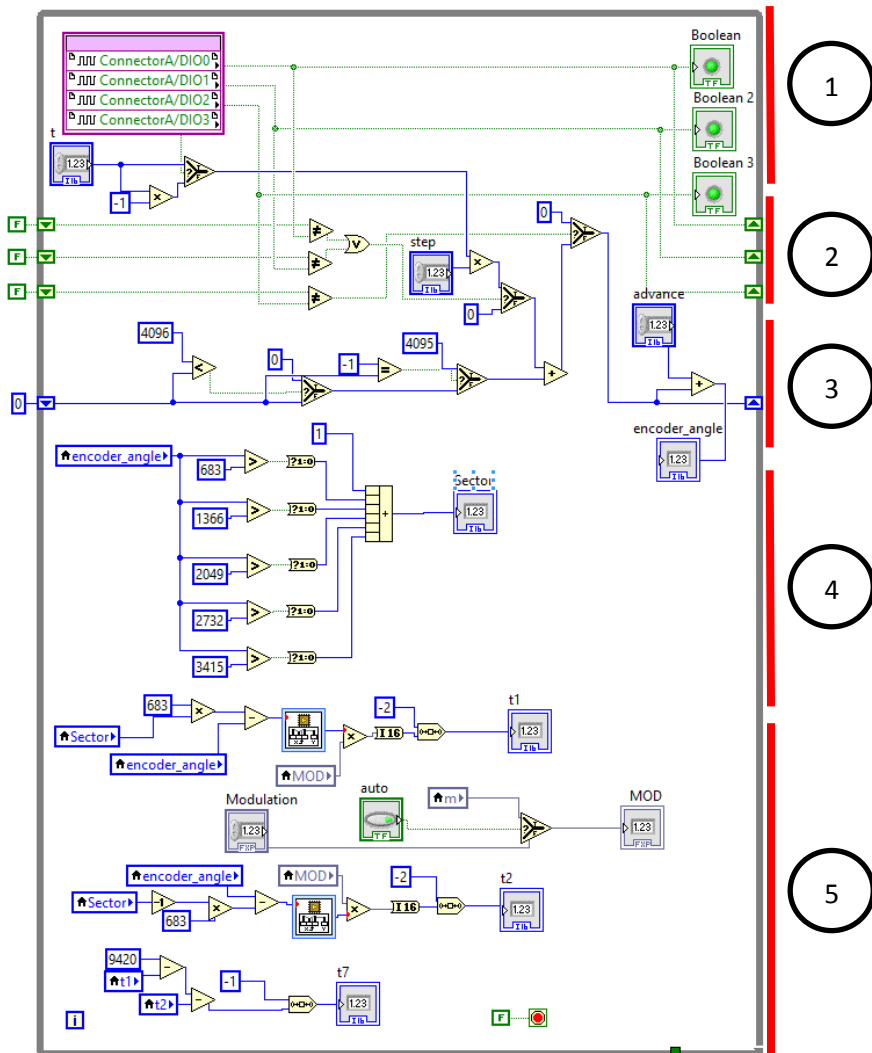


Figure 5.15 - Angle and time generator loop

## • Sector and vector generator loop

In the sector and vector generation, the logic previously discussed in section for Simulink simulation is again implemented. The PWM cycle time is compared with segregation time generated using the Turn on and off times of the SV-PWM vectors to generate the "Vector" value. As seen in the Figure 5.16, this vector value is then compared with a set of lookup tables to select if that respective phase needs to be turned on or off in the respective cycle of the controller.

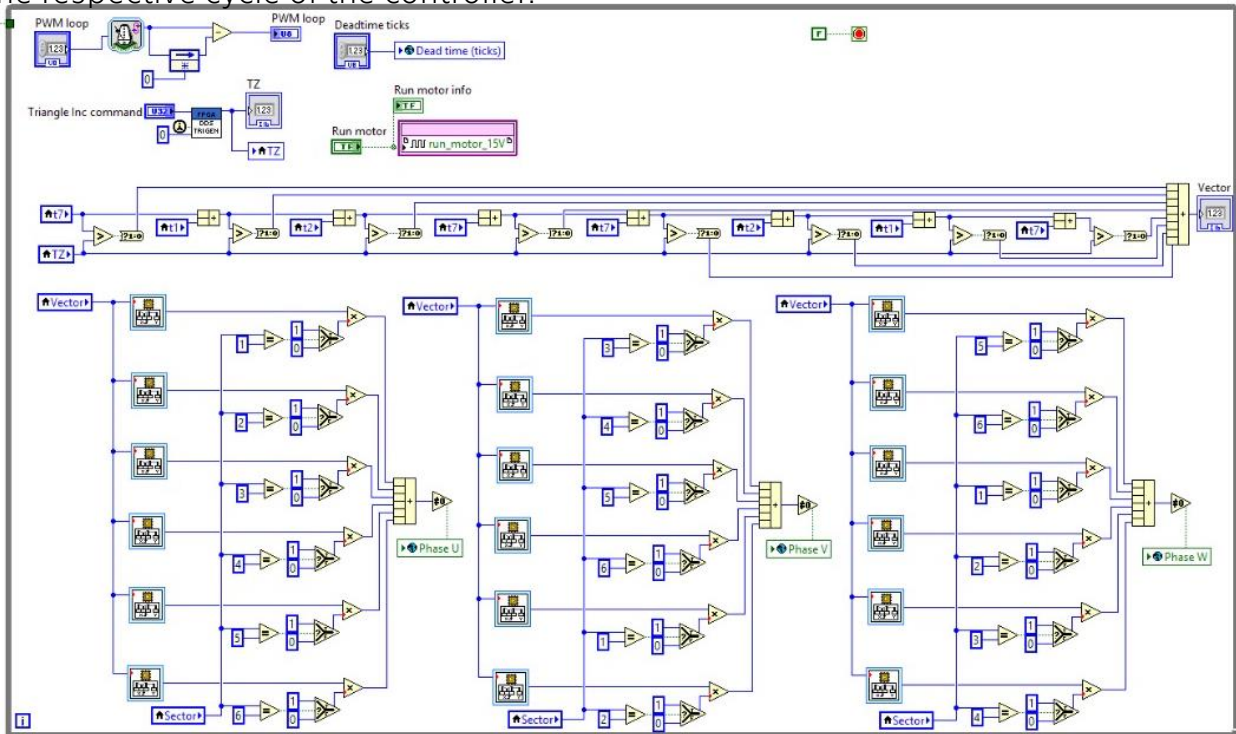


Figure 5.16 - Sector and vector generator loop

The below Table 3 – Look-up table data describes the data encapsulated in the above array of look-up tables. Each table contains a 1D look-up for finding a switch configuration of the respective Inverter switch in the existing vector at that instant. (1 – on, 0 - off)

While it would be substantially simpler to implement this as a 2D look-up table the above approach was implemented to circumvent the limitation that LabView FPGA allows for only 1D look-up tables.

Vector\Sector	1	2	3	4	5	6
1	0	0	0	0	0	0
2	1	0	0	0	0	1
3	1	1	0	0	1	1
4	1	1	1	1	1	1
5	1	1	1	1	1	1
6	1	1	0	0	1	1
7	1	0	0	0	0	1
8	0	0	0	0	0	0

Table 3 – Look-up table data

- **Phase signal generator loops**

Once the value of the phase signals are generated in the previously discussed loop, in the next Figure 5.17 the three loops for phase signals are triggered. In case that there is a change in the signal values it is not safe to directly pass it to the gates. This is due the fact that in real systems there are transients that exist in the components. This may lead to a short circuit in case that both switches happen to be on at the same time.

The solution to this is that we use a flat sequence block that first turns off both the switches and only after waiting for a predetermined specified time do we turn one of the two switches on for that leg of the 6-step inverter.

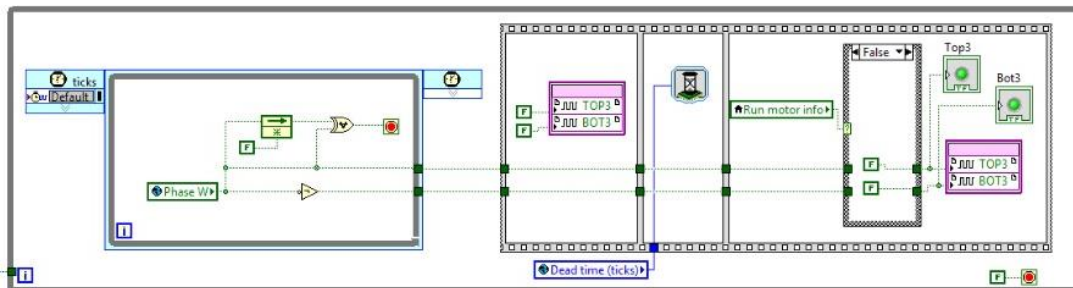


Figure 5.17 - Phase signal generator loops

- **FIFO data generator**

The loop for the FIFO (First In First Out) data generator in Figure 5.18 - FIFO Generator loop Figure 5.18 basically receives the signals generated at the FPGA level and prepares it to be transferred between different clock domains. It is this principle that allows for the transfer of data between the FPGA level to the LabView VI level in a format that can be processed and addressed.<sup>[37]</sup>

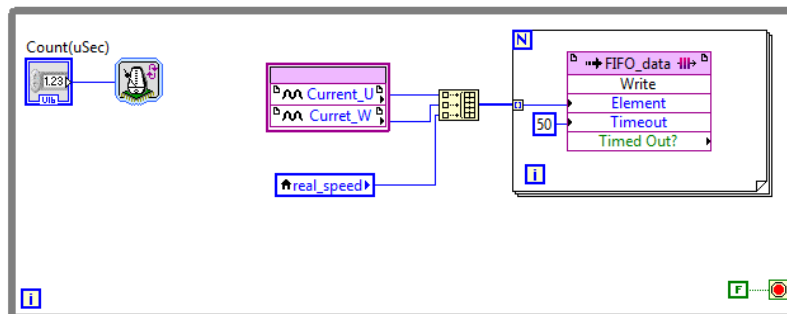


Figure 5.18 - FIFO Generator loop

## 5.2.2. Labview VI

The below Figure 5.19 and Figure 8.2 provide an overview of the front panel and block diagram of the LabView VI respectively. The Labview VI perform the task of the main higher level interfacing i.e. in this case the Labview VI front panel is the active HMI (Human Machine Interface) that can be toggled to bring about the change in characteristics of the algorithm. It serves as a Calibration tool.

Some of the main functionality captured in the LabView VI includes (see Appendix B for Block diagram)–

- Start-up of the system
- Configure FIFO Data reading
- Set and modify parameters for the FPGA module
- Read and display FIFO data
- Shut down system

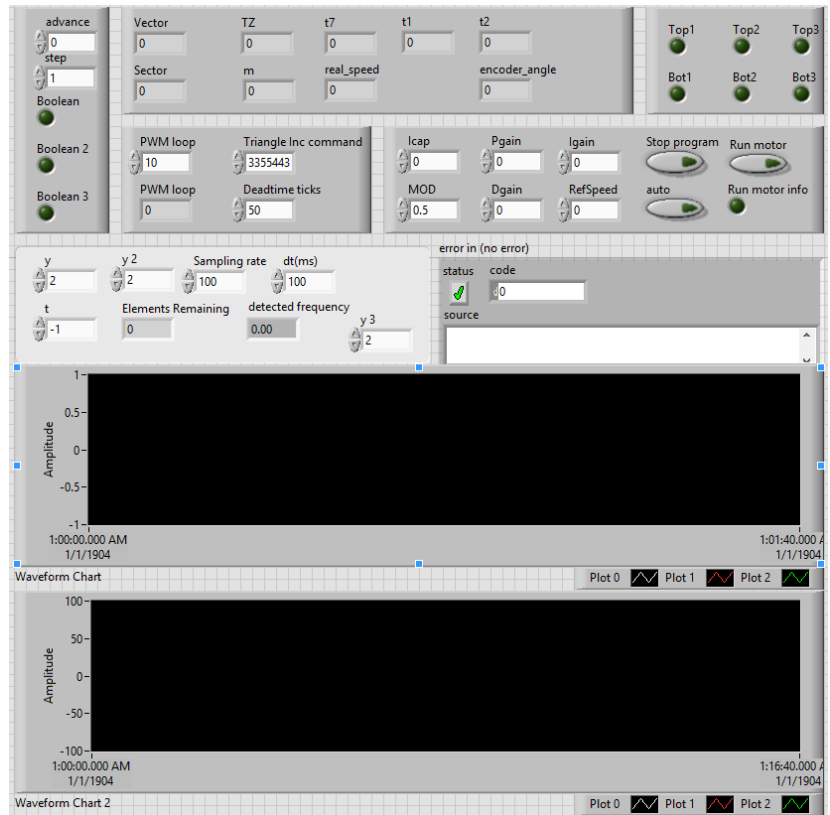


Figure 5.19 - LabView VI Front panel

### 5.2.3. Results from Practical implementation

The below graph in Figure 5.20 – *Real measured value from oscilloscope* is the plot of the real current readings from the phases of the motor power lines. The shape clearly reflects that the motor has experienced control through SV-PWM with a third harmonic being injected.

The motor performed with smooth speed and was fairly sensitive to the control changes requested through the HMI.

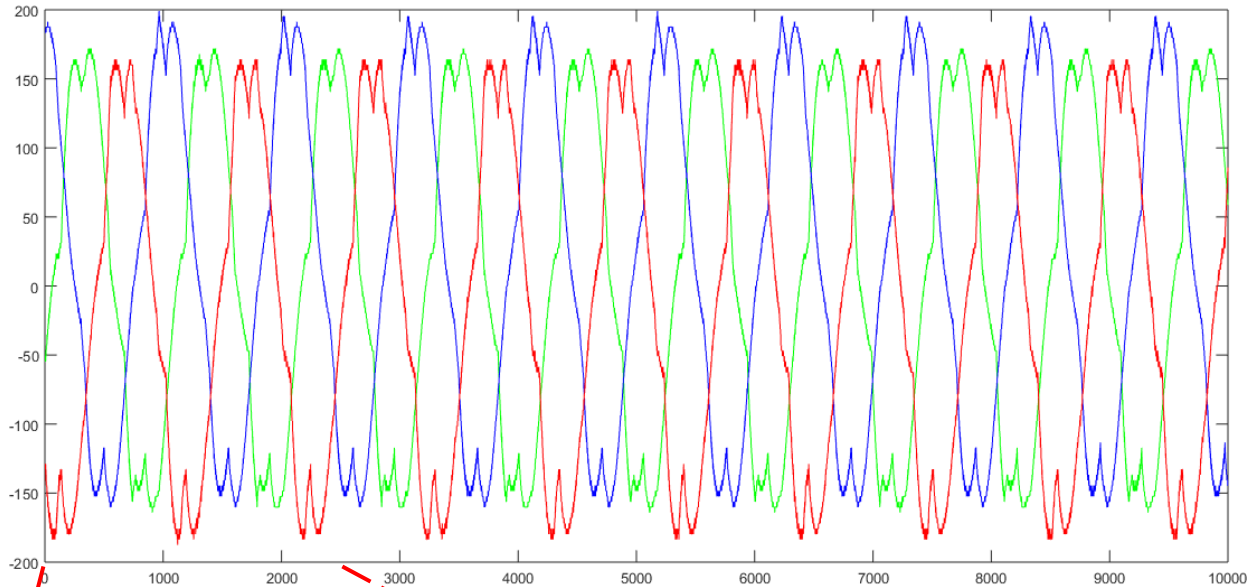


Figure 5.20 – *Real measured value from oscilloscope*

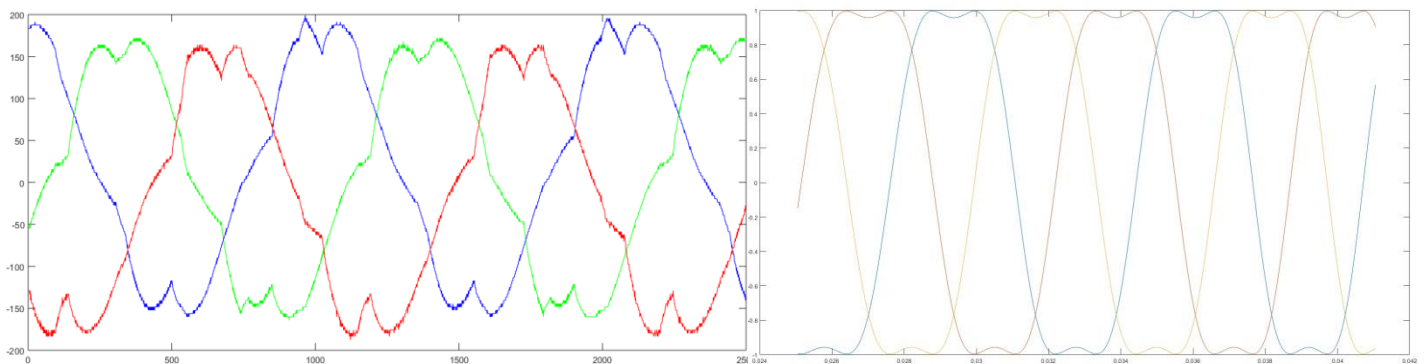


Figure 5.21 – Real vs. Simulated result

As can be seen in the comparison in Figure 5.21 with the simulated values the developed control algorithm was able to perform satisfactorily.



For the PID control, the values used for optimal control were found to be –

P gain, I Gain, D gain	0.1, 0.001, 0.001
Saturation value for Integrator	0.1
Rotational Speed	155 steps/ms
	= 155,000/ (4098 steps per rotation)
	= 37.8 rps
	= <u>2270 rpm</u>

These numbers though have very arbitrary values for the below reasons –

- The values for these gains are calibratables. The value varies from system to system. As we are not designing for the final motor to be used the values are applicable only to the scope of this research
- The motor shows the need for a variation in calibrated values with strong deviations from the set point
- The numbers for the gain values presently are selected in the scope of the Labview program design and hence vary with changes in other parameters such as iteration speed of each loop, dead time ticks needed for the switching.

The solution to these issues will be to have a realistic selection for the final roadworthy motor of the electric vehicle and then develop a mathematical model of the designed system. This will allow the true parameterization of the system properties and realistic predictions of the needed PID controller design.

## 6. Conclusion

In accordance with the goals of the Master's thesis, all the selected control algorithms have been simulated and the results have been studied.

In *Chapter 2*, the present market existent control strategies were researched and a comprehensive understanding of the algorithms was developed.

This was followed up in *Chapter 3* where modulation methods were compared and possible improvements for future improvements were proposed.

*Chapter 4* dealt with the simulation of control strategies and also the above mentioned improvements. The simulated results matched those predicted by the theoretical research –

- Basic six step control proved to be the simplest logic for execution. However, it has large motor torque ripples.
- Sensor-less control being a modification in 6-step control to take advantage of the BEMF provided similar response. Sensor-less control also proved to have fairly good feedback control allowing for a much more accurate PID control response
- Sensor-less control allowed for lower hardware requirements but also needed a start-up mechanism
- SV-PWM showed highest capability for torque production but needs a much higher complexity of control algorithm.
- SV-PWM also required a start-up algorithm in case of not have absolute position feedback at start up.
- PWM control methods proved very adept at controlling the motor but placed a much larger requirement upon the power pack of the system
- The newly proposed battery power management system showed promising results in simulation with large reduction in peak battery current

A practical realization of the SV-PWM motor control algorithm was implemented in *Chapter 5*. The results complied with the predictions of the simulations and some of the major outcomes include –

- The control algorithm for SV-PWM was successfully implemented LabView and the developed Control VI were able to run the motor in a range of varying operating conditions
- A peak rotational speed of approximately 2270 rpm was achieved with stability under limited power supply and no load conditions

- The modulation method with PID control proposed in Chapter 3 was successfully interfaced with the SV-PWM algorithm and marked improvements were observed in runtime in comparison with past experiences with a similar setup
- The third harmonic being injected for achieving over modulation was clearly observed as displayed in *Figure 5.21*.
- The

#### Limitations –

- Motor was not run at its highest possible rated speed. This was due to safety concerns for the test and also to ensuring that the motor driver not overheat during testing.
- The running test bench proves algorithm but still needs proofing under higher load conditions. As the test bench was not adaptable for a secure loading mechanism, the motor test was performed at no load.
- It was noted that a start-up algorithm or mechanism was required as the method of position finding for the rotor was based on inductive rotary transformer principle. This is applicable to the present motor and varies with the type of setup.

In conclusion, the goals established at the start of this thesis were accomplished and the results hold promising insights for future research and innovation in the fields of both BLDC motor control and the Electric vehicle industry.

## **6.1. Proposed research for Future**

The first stage of research for Ricardo plc. has resulted in a much deeper understanding of the behavior of the BLDC motor and its control system. In light of this, the research can be further pursued to develop a more holistic control system.

- Develop a test bench for the real required motor and control unit with load
- Develop a calibrated control
- Continue research in optimization for Battery power management system
- Develop a functional model of optimized power management system

# Appendix A - Hardware specifications

- **PMSM Motor**

The motor used in this thesis research is the 2AML406B-S <sup>[38]</sup> series of PMSM motor produced by VUES Brno s.r.o., Brno.

Type – 2AML406B-S – 000 <sup>[39]</sup>

Supply Voltage – 560 VDC maximum

Supply current - 11 A maximum

Torque – 1.2 Nm

Operating speed – 25000 rpm max. 40000 rpm

K = 6.79 V per 1000 rpm

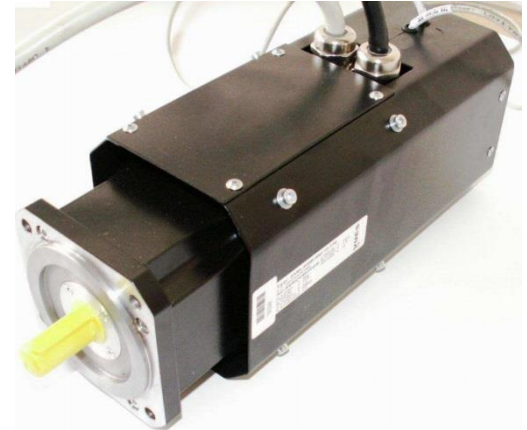


*Figure 7.1 - 2AML406B-S PMSM Motor<sup>[38]</sup>*

The AM motor series is provided with separate ventilation for achieving higher values of continuous torque and power output. <sup>[40]</sup>

At such high operating speeds, it becomes necessary to modify the design of the corresponding machine components to support operating characteristics. The major adjustment can be seen in the rotor design as an additional securing special bandage has been added to ensure the neodymium-based (NeFeB) rare earth magnets retain their accurate fixture.

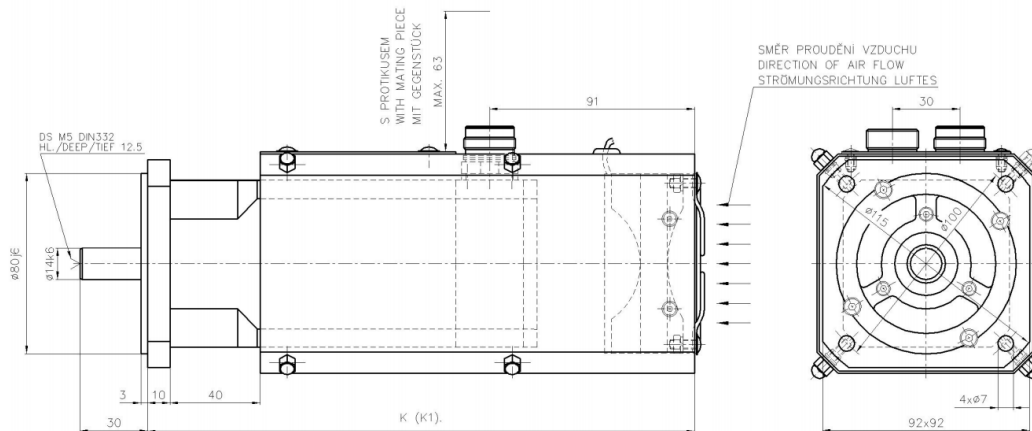
Use of a standard rotational speed sensor is operational only up to 20 000 min<sup>-1</sup>, hence, the motors come fitted with customized speed sensors from Micronor.

The motors 2AML406B are air-cooled and are supplied as standard with external ventilation. <sup>[41]</sup>

Some of the motor specifications and characteristics provided by the supplier can be seen in *Figure 7.2*.

# AML 40

Parameter / Basic data



SERVOMOTOR	$M_0$	MAYR	$M_B$	$t_{1max}$	$t_{2max}$	$U_{1DC}$	$n_{max}$	$J$	$m$
	[Nm]		[Nm]	[ms]	[ms]	[V]	[min <sup>-1</sup> ]	[kg.m <sup>2</sup> .10 <sup>-3</sup> ]	[kg]
AML 404 - B	1,7		2	50	30	24	9000	0,0245	0,62
AML 406 - B	3,2								
AML 408 - B	4,2								

$M_0$  - brzdňý moment / holding torque / Haltemoment  
 $J$  - moment setrvačnosti / moment of inertia / Trägheitsmoment  
 $m$  - hmotnost / weigh / Gewicht  
 $n_{max}$  - max. otáčky / max. speed / max. Drehzahl

$t_{1max}$  - max. čas sepnutí (odbrzdění) / max. time of switching-on / max. Einschaltzeit (Lösung der Bremse)  
 $t_{2max}$  - max. čas rozepnutí / max. time of switching-off / max. Ausschaltzeit  
 $U_{1DC}$  - jmenovité napětí / rated voltage / Eingangsspannung

Figure 7.2 - Technical data for 2AML406B<sup>[41]</sup>

## • DC Power Source

The source chosen was the Manson NP-9625. (see Figure 7.3)

### Characteristics

DC laboratory power supply <sup>[42]</sup>

One controllable output + two fixed outputs, display of actual values on controllable output with 2 LCD (Ammeter and Voltmeter). <sup>[43]</sup>

### Output parameters:

Adjustable channel: 0..30V / 10A  
 Fixed voltage: 5V / 0,5A; 12V / 0.5A  
 Dimensions: 205 x 115 x 280 mm  
 Weight: 7.5 kg



Figure 7.3 - Manson NP-9625

## • Six step Inverter components

### ○ Sixpack IGBT Driver

The SKHI 61 in the *Figure 7.4* can be optimized using adapter boards for each module type. It offers a fully qualified plug & play solution, saving time and costs in application. The high level of integration in SEMIKRON's chipset ensures that the IGBT gate can be safely controlled throughout the entire lifecycle. Short circuits are managed very fast by separate error channels. <sup>[44]</sup>



Figure 7.4 - Semikron SKHI 61<sup>[44]</sup>

### Features

- CMOS-compatible input buffers at VDD=5V
- Short-circuit protection by VCE - monitoring and Soft-turn-Off
- Drive interlock top/bottom
- Signal transmission by opto-couplers
- Supply under voltage protection (13V)
- Error latch / output
- Target Applications

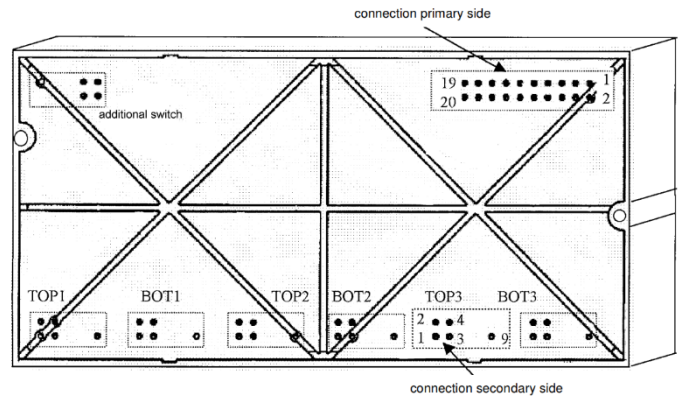


Figure 7.5 - Chip Back-view<sup>[44]</sup>

Driver for IGBT and MOSFET modules in three-phase-bridge circuits, inverter drives, UPS-facilities, etc.

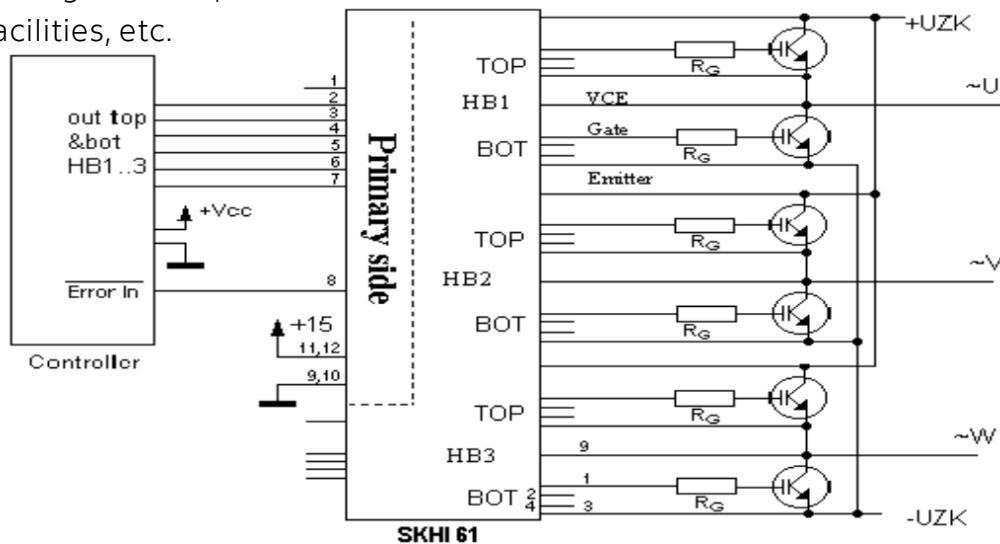


Figure 7.6 - Schematic of SKHI 61<sup>[44]</sup>

Pin connections on the bottom side of the Chip as seen in *Figure 7.5* are elaborated in below *Table 4 - Pin description*.<sup>[45]</sup>

*Table 4 - Pin description*

Pin	Symbol	Function	Pin	Symbol	Function
01	BS	Auxiliary earth connection	11	+15V	Supply voltage
02	BOT3	Driver signal BOT HB3	12	-15V	Supply voltage
03	TOP3	Driver signal TOP HB3	13	TDT1	Deadtime bit #1
04	BOT2	Driver signal BOT HB2	14	TDT2	Deadtime bit #2
05	TOP2	Driver signal TOP HB2	15	SEL	Deadtime on/off
06	BOT1	Driver signal BOT HB1	16	BSTD	Aux. earth for deadtime adjust
07	TOP1	Driver signal TOP HB1	17	__ERRI N	__ External error signal input
08	__ERR	__ Error output Sixpack-driver	18	NC	reserved
09	BSS	System earth connection	19	BRK	Driver signal additional switch
10	BSS	System earth connection	20	__BERR	__ Error output additional switch

The block diagram for the Semikron SKHI 61 can be seen in *Figure 7.6*. On primary side shall be connected the digital controller (In this case MyRio controller by National Instruments) and on the other side shall be the power electronic IGBT switches that form the top and bottom 3 switches in the 6-Step inverter. The below *Figure 7.7* is an overview of the chip's absolute and nominal performance characteristics.<sup>[45]</sup>

Absolute Maximum Ratings				Characteristics					
Symbol	Conditions	Values	Units	Symbol	Conditions	min.	typ.	max.	Units
$V_S$	Supply voltage primary	15,6	V	$V_S$	Supply voltage primary	14,4	15,0	15,6	V
$V_{IH}$	Input signal voltage	$V_S + 0,3$	V	$I_{SO}^{1)}$	Supply current no load	160		200	mA
$I_{outPEAK}$	Output peak current	2	A		primary side normal op.			450	mA
$I_{outAVmax}$	Output average current ( $T_a = 85^\circ C$ )	20	mA	$V_{IT+}$	Input threshold voltage (High)	4,0			V
$f_{max}$	Max. switching frequency ( $C_{GE} < 9nF$ )	50	kHz	$V_{IT-}$	Input threshold voltage (LOW)			1,5	V
$V_{CE}$	Collector emitter voltage sense across the IGBT (for 1200V-IGBTs)	900	V	$R_{in}$	Input resistance		60		k $\Omega$
dv/dt	Rate of rise and fall of voltage (secondary to primary side)	15	kV/ $\mu$ s	$V_{G(on)}$	Turn on gate voltage output		14,9		V
$V_{isolIO}$	Isolation test voltage input - output (2 sec. AC)	2500	V	$V_{G(off)}$	Turn off gate voltage output		-6,5		V
$V_{isol12}$	Isolation test voltage output 1 - output 2 (2 sec. AC)	1500	V	$R_{GE}$	Internal gate-emitter resistance		20		k $\Omega$
$R_{Gonmin}$	Minimum rating of $R_{Gon}$	10	$\Omega$	$f_{ASIC}$	ASIC system switching frequency		8		MHz
$R_{Goffmin}$	Minimum rating for $R_{Goff}$	10	$\Omega$	$t_{d(on)IO}$	Input-output turn-on propagation time	0,3	0,45	0,6	$\mu$ s
$Q_{out/pulse}$	Max. rating for gate $T_a = 85^\circ C$ charge per pulse $T_a = 55^\circ C$	0,7	$\mu$ C	$t_{d(off)IO}$	Input-output turn-off propagation time	0,3	0,45	0,6	$\mu$ s
$T_{op}$	Operating temperature	- 40 ... + 85	$^\circ C$	$t_{d(terr)}$	Error input-output propagation time	1,15	1,3	1,5	$\mu$ s
$T_{stg}$	Storage temperature	- 40 ... + 85	$^\circ C$	$t_{pERRRESET}$	Error memory reset time	7	15	27	$\mu$ s
				$t_{TD}$	Interlock dead time adjustable	no interlock		4,1	$\mu$ s
				$V_{CEstat}$	Reference voltage for $V_{CE}$ -monitoring		5,8		V
				$t_{blank}$	Blanking time		3,5		$\mu$ s
				$C_{ps}$	Coupling capacitance primary-secondary		40		pF
				MTBF	Mean Time Between Failure $T_a = 40^\circ C$		1		$10^6$ h
				w	weight		95		g
				H x B x T	Dimensions		20x57x114		mm

*Figure 7.7- Characteristics of SKHI 61*

## o IGBT module

The SEMIKRON IGBT (Insulated-Gate Bipolar Transistor) module SKM 75 GD 124 D ( see *Figure 7.8*) offering upto 75A in voltage class 1200V has been used for the power electronic inverter bridge for the PMSM motor supply. It is of a sixpack topology in *Figure 7.9*. Featuring the latest IGBT chips in combination with SEMIKRON's CAL diode technology, the latest IGBT generation 7 is available in SEMIKRON's SKM power module. It provides higher power densities and delivers the new benchmark, especially in motor drive and solar applications.<sup>[46]</sup>



*Figure 7.8 - SKM 75 GD 124 D<sup>[43]</sup>*

Features<sup>[47]</sup>

- MOS input (voltage controlled)
- N channel, homogeneous Silicon structure (NPT- Non punchthrough IGBT)
- Low loss high density chip
- Low tail current
- High short circuit capability Latch-up free
- Fast & soft inverse CAL diodes
- Isolated copper baseplate using DCB Direct Copper Bonding Technology without hard mould

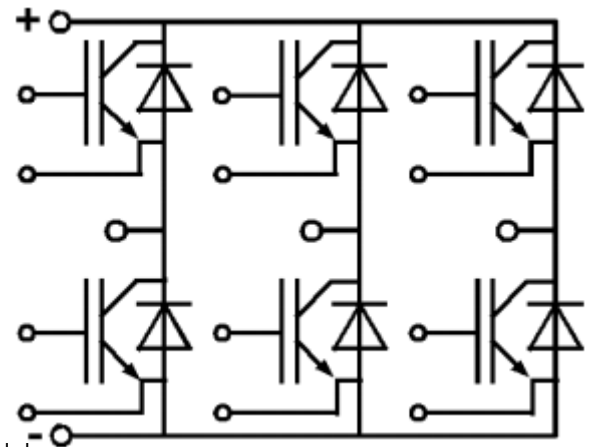


*Figure 7.9 - Schematic of SKM<sup>[43]</sup>*

Absolute Maximum Ratings				Characteristics					
T <sub>c</sub> = 25 °C, unless otherwise specified				T <sub>c</sub> = 25 °C, unless otherwise specified					
Symbol	Conditions	Values	Units	Symbol	Conditions	min.	typ.	max.	Units
<b>IGBT</b>									
V <sub>CES</sub>	T <sub>j</sub> = 25 °C	1200	V	V <sub>GE(th)</sub>	V <sub>GE</sub> = V <sub>CE</sub> , I <sub>C</sub> = 2 mA	4,5	5,5	6,5	V
I <sub>C</sub>	T <sub>j</sub> = 150 °C	75	A	I <sub>CES</sub>	V <sub>GE</sub> = 0 V, V <sub>CE</sub> = V <sub>CES</sub> , T <sub>j</sub> = 25 °C	0,4	1,2		mA
I <sub>CRM</sub>	T <sub>case</sub> = 25 °C	50	A	V <sub>CE(u)</sub>	T <sub>j</sub> = 25 °C	1,4	1,6		V
V <sub>GES</sub>	T <sub>case</sub> = 80 °C	100	A	V <sub>CE</sub>	T <sub>j</sub> = 125 °C	1,6	1,8		V
t <sub>psc</sub>	I <sub>CRM</sub> = 2 × I <sub>Cnom</sub>	± 20	V	V <sub>CE</sub>	V <sub>GE</sub> = 15 V, T <sub>j</sub> = 25 °C	22	28		mΩ
I <sub>F</sub>	V <sub>CC</sub> = 600 V; V <sub>GE</sub> ≤ 20 V; V <sub>CES</sub> < 1200 V; T <sub>j</sub> = 125 °C	10	μs	V <sub>CE</sub>	T <sub>j</sub> = 125 °C	30	38		mΩ
I <sub>FRM</sub>	T <sub>j</sub> = 150 °C	75	A	V <sub>CE(sat)</sub>	I <sub>Cnom</sub> = 50 A, V <sub>GE</sub> = 15 V, T <sub>j</sub> = °C <sub>chiplév.</sub>	2,5	3		V
I <sub>FSM</sub>	T <sub>case</sub> = 25 °C	50	A	C <sub>ies</sub>	V <sub>CE</sub> = 25 V, V <sub>GE</sub> = 0 V, f = 1 MHz	3,3	4,3		nF
I <sub>th(RMS)</sub>	T <sub>case</sub> = 80 °C	100	A	C <sub>oes</sub>		0,5	0,6		nF
T <sub>vj</sub>	I <sub>FRM</sub> = 2 × I <sub>Fnom</sub>	100	A	C <sub>res</sub>		0,22	0,3		nF
V <sub>stg</sub>	I <sub>FSM</sub> = 10 ms; sin. T <sub>j</sub> = 150 °C	550	A	t <sub>di(on)</sub>	R <sub>Gon</sub> = 22 Ω, V <sub>CC</sub> = 600V, I <sub>Cnom</sub> = 50A, T <sub>j</sub> = 125 °C, V <sub>GE</sub> = ± 15V	44	100		ns
V <sub>isol</sub>	t <sub>di(off)</sub>	100	A	t <sub>tr</sub>		56	100		ns
	t <sub>di(off)</sub>	- 40 ... + 150	°C	E <sub>on</sub>		8			mJ
	t <sub>di(off)</sub>	- 40 ... + 125	°C	t <sub>di(off)</sub>	R <sub>Goff</sub> = 22 Ω	380	500		ns
		2500	V	t <sub>f</sub>		70	100		ns
				E <sub>off</sub>		5			mJ
				R <sub>th(j-c)</sub>	per IGBT		0,32		K/W

*Figure 7.10 - Characteristics of SKM 75<sup>[43]</sup>*



## ○ **AC/DC transformer**

The HAHN BV EI 481 1184 offers an AC/DC transformer maximum safety and durability device with excellent resistance to temperature changes, high overvoltage resistance, self-extinguishing cover. [48]

Parameters:

- Power: 10 VA
- Voltage primary: 1x230 V
- PIN primary: 1-6
- Secondary voltage: 1x15 V
- Secondary secondary: 667 mA
  
- PIN secondary: 8-11
- No-load voltage: 1x18.6 V



Figure 7.11 - BV EI 481 1184 transformer<sup>[45]</sup>

## ○ **Current sensor**

The sensor used for this board is the LEM LA-55-P current sensor. It proves ideal for the measurement of currents: DC, AC, PWM with a galvanic separation between the primary circuit and the secondary counterpart. [49]

Features

- Closed loop (compensated) current transducer using the Hall Effect
- Insulating plastic case recognized according to UL 94-V0.

Advantages

- Excellent accuracy
- Very good linearity
- Low temperature drift
- Optimized response time
- Wide frequency bandwidth
- No insertion losses
- High immunity to external interference
- Current overload capability



Figure 7.12 - LEM LA-55-P Current sensor<sup>[46]</sup>

# Appendix B – LabView Block Diagram

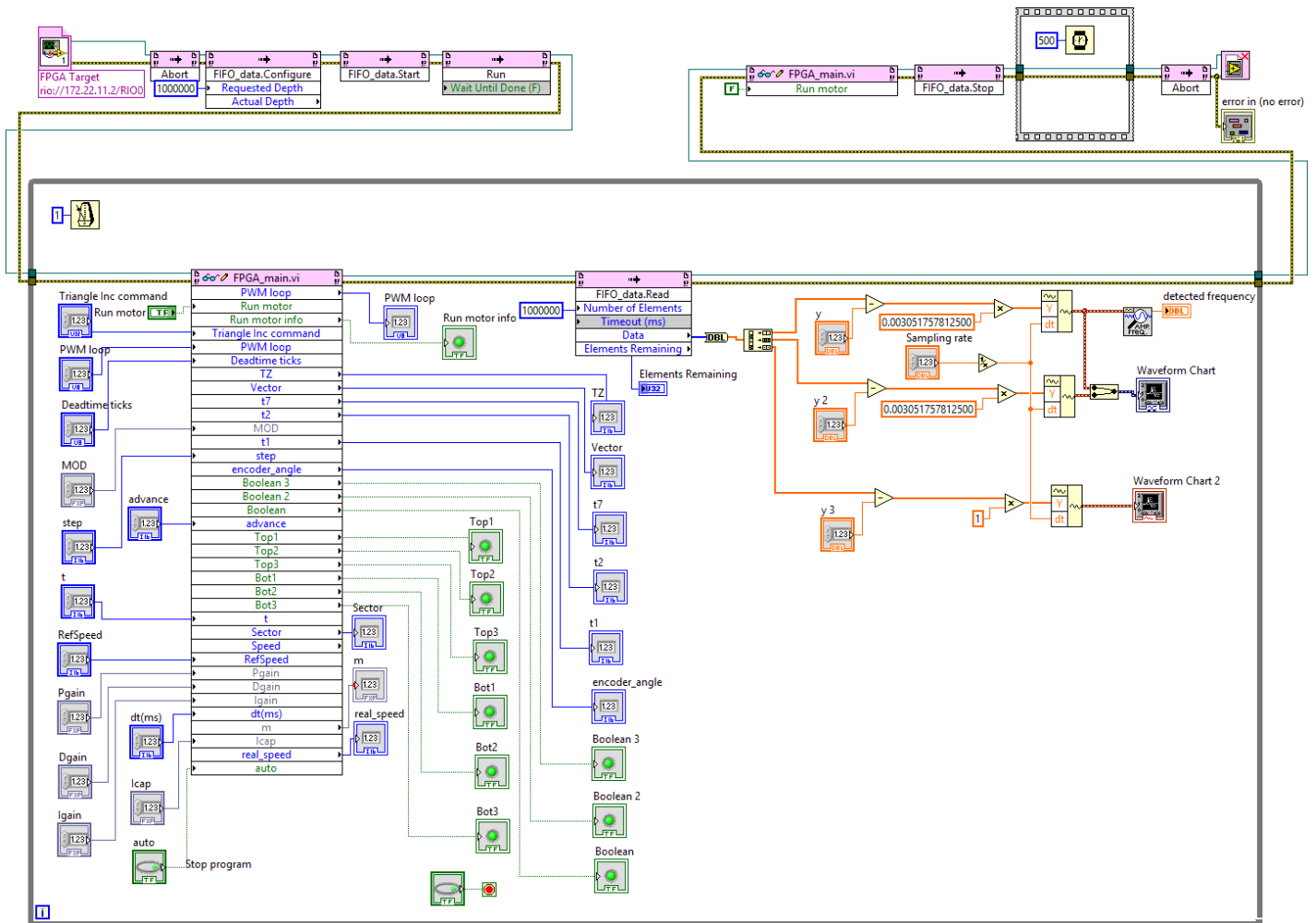


Figure 8.1 –Block diagram for LabView Section

Figure 8.2 – Block Diagram for FPGA Section

On following page

# References

---

- 1 Gao, X. *BLDC motor control with Hall sensors based on FRDMKE02Z*. Application Note AN4776, Freescale Semiconductor Inc 2013; Available from: <https://www.nxp.com/docs/en/application-note/AN4776.pdf>.
- 2 Krishnan, R. *Permanent Magnet Synchronous and Brushless DC Motor Drives*. Boca Raton, 2010. ISBN 978-0-8247-5384-9
- 3 Contributors, A. *All about circuits - Vol. II - Alternating Current (AC)*. 2019; Available from: <https://www.allaboutcircuits.com/textbook/alternating-current/chpt-13/brushless-dc-motor/>.
- 4 Viramontes, E. *BLDC motor control with Hall effect sensors using the 9S08MP*. Application Note AN4058, Freescale Semiconductor Inc 2010; Available from: <https://www.nxp.com/docs/en/application-note/AN4058.pdf>.
- 5 MATLAB Help -<https://www.mathworks.com/help/physmod/sps/ref/pmsm.html>
- 6 Grenier, D., et al., *Experimental nonlinear torque control of a permanent-magnet synchronous motor using saliency*. IEEE Transactions on Industrial Electronics, 1997. 44(5): p. 680-687.
- 7 Toliyat, H.A. *Analysis and simulation of multi-phase variable speed induction motor drives under asymmetrical connections*. in *Proceedings of Applied Power Electronics Conference. APEC'96*. 1996. IEEE.
- 8 Baudart, F., et al. *Control under normal and fault tolerant operation of multiphase SMPM synchronous machines with mechanically and magnetically decoupled phases*. in *2009 International Conference on Power Engineering, Energy and Electrical Drives*. 2009. IEEE.
- 9 Krause, P.C., et al., *Analysis of electric machinery and drive systems*. Vol. 2. 2002: Wiley Online Library.
- 10 Xia, C.-I., *Permanent magnet brushless DC motor drives and controls*. 2012: John Wiley & Sons.
- 11 Wilson, T. and P. Trickey. *DC Machine with Solid State Commutation*, AIEE paper I. CP62-1372, October 1962.

- 
- 12 Momenzadeh, Mohammad Mahdi & Ahmed, Abdullah & Tolba, Amr. *Modelling and Simulation of The BLDC Electric Drive System Using SIMULINK/MATLAB for a Hybrid Vehicle*. 2014.  
Available from: [https://www.researchgate.net/publication/262933380\\_Modelling\\_and\\_Simulation\\_of\\_The\\_BLDC\\_Electric\\_Drive\\_System\\_Using\\_SIMULINKMATLAB\\_for\\_a\\_Hybrid\\_Vehicle](https://www.researchgate.net/publication/262933380_Modelling_and_Simulation_of_The_BLDC_Electric_Drive_System_Using_SIMULINKMATLAB_for_a_Hybrid_Vehicle)
  - 13 Microelectronics, S. *Application Note AN1276 BLDC Motor Start Routine for the ST72141 Microcontroller*.  
Available from: <https://forums.parallax.com/discussion/download/83730&d=1312466087>.
  - 14 Buso, Simone, Paolo Mattavelli. *Digital Control in Power Electronics*. Morgan & Claypool, 2006. ISBN 9781598291131
  - 15 Kazmierkowski, Marian. P., Krishnan, R., Blaabjerg, F. *Control in power electronics: selected problems*. New York: Academic press.2002. ISBN 01-240-2772-5
  - 16 Jose Jacob, Chitra. *Field Oriented Control of Space Vector Modulated Multilevel Inverter fed PMSM Drive*. 2017 ;  
Available from: <https://www.sciencedirect.com/science/article/pii/S187661021732458X>
  - 17 D. Lalili, E. M. Berkouk, F. Boudjema, N. Lourci, T. Taleb, Petzold. *Simplified space vector PWM algorithm for five-level inverter*. 2007.
  - 18 Aleenejad, M., H. Iman-Eini, and S. Farhangi. *Modified space vector modulation for fault-tolerant operation of multilevel cascaded H-bridge inverters*. IET Power Electronics, 2013. 6, 742-751.
  - 19 Solbakkenspace, Y. *Vector PWM Intro* 2019;  
Available from: <https://www.switchcraft.org/learning/2017/3/15/space-vector-pwm-intro>.
  - 20 Soumya Ranjan Pradhan. *Principle of Space Vector PWM*  
Available from: <https://www.slideshare.net/biswajitcet13/svpwm>
  - 21 O. Bouhali, B. Francois, E. M. Berkouk, C. Saudemont. *A general modelling and control algorithm of a three-phase multilevel diode clamped inverter by means of a direct space vector control*. 2005.
  - 22 Satish Kumar Peddapelli. *Pulse Width Modulation – Analysis and performance in Multilevel Inverters*. 2016.
  - 23 Martin Novák, J.C., Ondřej Stanke. *High-speed Micro Turbine Power Generator*. 2010;

- 
- Available from: [http://www1.fs.cvut.cz/cz/U12110/vyzkum/Kostelec10/prispevek\\_novakm.pdf](http://www1.fs.cvut.cz/cz/U12110/vyzkum/Kostelec10/prispevek_novakm.pdf)
- 24 SEMIKRON . *IGBT Modules*. 2019  
Available from: <https://www.semikron.com/products/product-classes/igbt-modules.html#view/table/items/20/search/skm%2075gdl/>
- 25 HAHN - Elektrobau GmbH & Co. KG. *BV EI 481 1184*.  
Available from: <https://www.gme.cz/data/attachments/dsh.610-809.1.pdf>
- 26 LEM. *Current Transducer LA 55-P*. 2018.  
Available from: [https://www.lem.com/sites/default/files/products\\_datasheets/la\\_55-p\\_e.pdf](https://www.lem.com/sites/default/files/products_datasheets/la_55-p_e.pdf)
- 27 Instruments, N. *myRIO Student Embedded Device*. 2019;  
Available from: <http://www.ni.com/cs-cz/shop/select/myrio-student-embedded-device>.
- 28 Instruments, N. *USER GUIDE AND SPECIFICATIONS NI myRIO-1900*. 2019;  
Available from: <http://www.ni.com/pdf/manuals/376047c.pdf>.
- 29 Lukáš Knotek , *Elektronický obvod pro vyhodnocení úhlového natočení snímače polohy*. 2006.
- 30 Instruments, N. *What Is LabVIEW?* 2019;  
Available from: <http://www.ni.com/cs-cz/shop/labview.html>
- 31 Elliott, C., et al., *National Instruments LabVIEW: A Programming Environment for Laboratory Automation and Measurement*. JALA: Journal of the Association for Laboratory Automation, 2007. 12(1): p. 17-24.
- 32 Kalkman, C.J., *LabVIEW: A software system for data acquisition, data analysis, and instrument control*. *Journal of Clinical Monitoring*, 1995. 11(1): p. 51-58.
- 33 Alan D. Degenhart, John W. Kelly, Robin C. Ashmore. *Craniux: A LabVIEW-Based Modular Software Framework for Brain-Machine Interface Research*  
Available from: <https://www.ncbi.nlm.nih.gov/pmc/articles/PMC3113411/>
- 34 Doru Ursutiu, Marius Ghercioiu, Cornel Samoila, Petru Cotfas. *FPGA LabVIEW Programming, Monitoring and Remote Control*. 2009.  
Available from: <https://online-journals.org/index.php/i-joe/article/view/874>

- 
- 35 Instruments, N. *What Is the LabVIEW FPGA Module?* 2019;  
Available from: <http://www.ni.com/cs-cz/shop/electronic-test-instrumentation/add-ons-for-electronic-test-and-instrumentation/what-is-labview-fpga-module.html>.
- 36 Field-programmable gate array (FPGA). 2005;  
Available from: <https://whatis.techtarget.com/definition/field-programmable-gate-array-FPGA>
- 37 Instruments, N. *Read (FIFO Method)*  
Available from: [http://zone.ni.com/reference/en-XX/help/371599P-01/lvfpga/fifo\\_read/](http://zone.ni.com/reference/en-XX/help/371599P-01/lvfpga/fifo_read/)
- 38 Martin Novák, J.C., Ondřej Stanke. *High-speed Micro Turbine Power Generator*. 2010;  
Available from: [http://www1.fs.cvut.cz/cz/U12110/vyzkum/Kostelec10/prispevek\\_novakm.pdf](http://www1.fs.cvut.cz/cz/U12110/vyzkum/Kostelec10/prispevek_novakm.pdf)
- 39 V.B s.r.o. *AML 40*. 2017;  
Available from: [http://www.moogbrno.cz/mt-content/uploads/2017/09/en\\_aml40\\_130502.pdf](http://www.moogbrno.cz/mt-content/uploads/2017/09/en_aml40_130502.pdf)
- 40 ELEKTRO. *New series of synchronous servomotors 2AML406B*. 2013;  
Available from: <http://www.odbornecasopisy.cz/elektro/clanek/nova-rada-synchronnich-servomotoru-2aml406b--489>.
- 41 Brno, M. *DATA SHEETS servomotors*. 2019;  
Available from: <http://www.moogbrno.cz/vues-servomotors/#001>.
- 42 Electronics, G. *Laboratorní zdroj MANSON NP-9625-000G*. 2019;  
Available from: <https://www.gme.cz/laboratorni-zdroj-manson-np-9625-000g>.
- 43 NP. *NP-9625 DC REGULATED POWER SUPPLY*. 2019;  
Available from: <https://www.gme.cz/data/attachments/orn.722-281.1.pdf>.
- 44 SEMIKRON. *SKHI 61 R*. 2019; Available from:  
<https://www.semikron.com/products/product-classes/igbt-driver/detail/skhi-61-r-l6100061.html>.
- 45 SEMIKRON. *SEMIDRIVERTM SKHI 61 (R)*. 2019;  
Available from: <https://www.semikron.com/dl/service-support/downloads/download/semikron-datasheet-skhi-61-r-l6100061.pdf>.
- 46 SEMIKRON. *IGBT Modules*. 2019  
Available from: <https://www.semikron.com/products/product-classes/igbt-modules.html#view/table/items/20/search/skm%2075gdl/>

- 
- 47 SEMIKRON. *SEMISTRANS M Low Loss IGBT Modules*  
Available from: [https://gazellec.com/wp-content/uploads/2018/09/SKM75GD124D-Semikron-IGBT-Module\\_DataSheet.pdf](https://gazellec.com/wp-content/uploads/2018/09/SKM75GD124D-Semikron-IGBT-Module_DataSheet.pdf)
- 48 HAHN - Elektrobau GmbH & Co. KG. *BV EI 481 1184*.  
Available from: <https://www.gme.cz/data/attachments/dsh.610-809.1.pdf>
- 49 LEM. *Current Transducer LA 55-P*. 2018.  
Available from: [https://www.lem.com/sites/default/files/products\\_datasheets/la\\_55-p\\_e.pdf](https://www.lem.com/sites/default/files/products_datasheets/la_55-p_e.pdf)